

NLO QCD Corrections to $W+W+$ Scattering at the LHC with Three Jets Matched to a Parton Shower

Dissertation

der Mathematisch-Naturwissenschaftlichen Fakultät
der Eberhard Karls Universität Tübingen
zur Erlangung des Grades eines
Doktors der Naturwissenschaften
(Dr. rer. nat.)

vorgelegt von
Santiago Lopez Portillo Chavez
aus Guadalajara/Mexiko

Tübingen
2024

Gedruckt mit Genehmigung der Mathematisch-Naturwissenschaftlichen Fakultät der
Eberhard Karls Universität Tübingen.

Tag der mündlichen Qualifikation:

05.12.2024

Dekan:

Prof. Dr. Thilo Stehle

1. Berichterstatter/-in:

Prof. Dr. Barbara Jäger

2. Berichterstatter/-in:

Prof. Dr. Werner Vogelsang

Contents

Introduction	1
1 Theoretical Background	5
1.1 Quantum Field Theory	5
1.1.1 Fields and Green's Functions	5
1.1.2 The S -matrix, Cross Sections and the Reduction Formula	11
1.2 Divergences at Next-to-Leading Order	15
1.2.1 Loops and Ultraviolet Divergences	15
1.2.2 Renormalization	18
1.2.3 Infrared Divergences and the KLN Theorem	20
1.3 Gauge Theories and the Standard Model	23
1.3.1 The Standard Model	25
1.3.2 Electroweak Symmetry Breaking	28
1.3.3 The Running of α_s	32
1.3.4 Lagrangian and Feynman Rules	34
1.4 Hadron Collisions and Factorization	39
1.5 The Structure of a Collision Event	43
1.6 Jets	45
2 Nex-to-leading Order Calculations and Parton Showers	47
2.1 Infrared Subtraction	47
2.1.1 Frixione-Kunszt-Signer Subtraction Method	50
2.2 Parton Showers	52
2.3 Matching of NLO Calculations to Parton Showers	55
3 Vector Boson Scattering and the $pp \rightarrow W^+W^+jjj$ Process	59
3.1 Electroweak Production of W^+W^+jjj at the LHC	63
3.1.1 One-Loop Corrections	65
3.1.2 Real-Emission Corrections	67
3.2 The Vector-Boson-Scattering Approximation	69
3.2.1 The VBS Signature	70
3.2.2 Electroweak Propagators in the s -Channel	71
3.2.3 Diagrams with Gluon Exchange	73
3.2.4 Identical-Particle Effects	76

3.2.5	The Structure-Function Approach to Vector Boson Scattering	77
4	Implementation	80
4.1	POWHEG BOX	80
4.2	Process-Specific Parts	82
4.2.1	Flavor Structures	82
4.2.2	Matrix Elements	83
4.2.3	Channel Mapping	85
4.2.4	The Born Suppression Factor	86
4.3	Validation	87
5	Numerical Studies	89
5.1	Input Parameters and Analysis Setup	89
5.2	Results at Fixed Order	90
5.3	Parton-Shower Results	95
	Summary and Outlook	99

Introduction

With the discovery of the Higgs boson in 2012 [1, 2], the last missing piece of the Standard Model of particle physics (SM) was found. Since then, the paradigm within the high-energy physics community has shifted towards precision, with the goal of finding or constraining new-physics effects that might be hiding in the details.

In this context, Vector-Boson Scattering (VBS) is a class of processes that represents a unique window into the electroweak (EW) sector of the SM and has received significant attention by both theoretical and experimental physicists. As the name suggests, these processes involve the interaction of two electroweak vector bosons that results in the emission of two new bosons, i.e. a $2 \rightarrow 2$ process¹. The scattering of the vector bosons can happen by exchanging another particle or directly, and these interactions involve the so-called triple and quartic gauge couplings (TGC and QGC) between the bosons. Thus, VBS processes are ideal to study these SM parameters. Furthermore, the scattering amplitude in the SM for longitudinally polarized electroweak bosons is finite only because of the possibility of scattering by the exchange of a Higgs boson [3], which makes the leading energy behavior of the full matrix element constant at high energies [4]. If the contributions involving Higgs-boson exchange were not present, the scattering amplitude of the process would diverge linearly with the center-of-mass energy squared, which leads to the violation of unitarity at about 1 TeV [4]. This precise cancellation would in general be spoiled if the couplings of EW vector bosons with themselves and the Higgs boson that are realized in nature do not exactly correspond to those of the SM [5], i.e. if they are *anomalous*. If this is the case, then it must be assumed that some new-physics mechanism that avoids the violation of unitarity is at play at high energies. In this scenario, the cross section of VBS could increase significantly at energies between the Higgs boson mass and the new-physics energy scale [6], before the unitarity-restoring mechanism takes over. Such an increase could thus be an indication of new physics. All in all, the investigation of VBS processes offers an opportunity to to achieve an overall better understanding of the EW sector of the SM and its electroweak symmetry breaking (EWSB) mechanism and to look for or constrain new-physics effects. For this purpose, high precision in both calculations and measurements are indispensable.

The Large Hadron Collider (LHC) is the most powerful particle accelerator to date, and is the largest current laboratory in which particle physics is investigated. It is the first particle accelerator in which VBS can be observed. At the LHC, highly energetic protons collide and VBS is realized by the emission of a vector boson by (a constituent of) each proton, and the subsequent scattering of the two vector bosons. The vector bosons that result from the interaction then decay into quarks or leptons, which ultimately give rise to the signals in the detector. At the lowest order, VBS is

¹So-called Vector-Boson Fusion (VBF) processes, in which the bosons fuse to produce one single particle ($2 \rightarrow 1$), are sometimes considered part of the broader VBS-type of processes because they share many common traits. We adopt this convention here.

	WWWW	WW $\gamma\gamma$	WWZ γ	WWZZ
$W^\pm W^\pm jj$	✓			
WZjj				✓
ZZjj				✓
Z γ jj			✓	
WW (via $\gamma\gamma$)		✓		

Figure 1: Summary of the VBS processes observed at the LHC (left column) and the QGC that each is sensitive to, from Ref. [15].

a purely EW process. The interacting bosons can be of several kinds and involve different couplings. In 2014, the first hint of scattering of same-sign W bosons at the LHC was reported by the ATLAS collaboration [7]. In the following years, this observation was confirmed by both the CMS and ATLAS groups [8, 9], as well as the observation of processes involving the scattering of WZ , $Z\gamma$, and ZZ [10, 11, 12].

Figure 1 summarizes some of the processes used to study VBS at the LHC (leftmost column) and the QGC that these are able to probe (upper row). There, each process is denoted by its final state, which contains two *jets* (j) in the first four rows. These jets originate from the constituents of the proton after emitting the vector bosons. The last row corresponds to the process observed in Refs. [13, 14], in which the protons, while remaining intact, emit one photon each, which annihilate into a W^+W^- pair. In this case, the protons are undetected and no jets are produced. In Fig. 1, the QGC are denoted by the four bosons that participate in the interaction.

Theoretical calculations of VBS processes have been available for around 30 years [16, 17, 18]. These calculations were performed at *leading order* (LO) in perturbation theory, and the most advanced ones considered the decay products of the vector bosons as part of the final state. This has become standard practice, as it yields a more realistic description of the signal that is experimentally observed. In the meantime, enormous progress has been made towards results at *Next-to-Leading Order* (NLO) accuracy. NLO corrections in the strong interactions (QCD corrections) have been calculated for the scattering of $W^\pm Z$, W^+W^- , ZZ and $W^\pm W^\pm$ [19, 20, 21, 22]. The last three *fixed order* calculations have subsequently been matched to *parton showers* (PS) in [23, 24, 25], giving predictions at leading-logarithmic order even before experimental observations of the processes were available. These calculations rely on the so-called VBS approximation, in which some contributions to the full processes are neglected. This approximation will be discussed in detail in this work.

More recently, full calculations of the EW NLO corrections to $W^\pm W^\pm$ scattering were presented [26], and later the complete NLO corrections, which include EW, QCD

and mixed contributions, were calculated [27, 28]. When these became available, the quality of the VBS approximation was analyzed in Refs. [6, 28] for the process corresponding to W^+W^+ scattering. There, it was found that the approximation is justified in certain regions of the phase space. In Ref. [29], the EW NLO corrections to $W^\pm W^\pm$ scattering were matched with parton showers. Complete NLO corrections to $W^\pm Z$, ZZ and W^+W^- scattering have been presented more recently [30, 31, 20].

Among VBS processes, the scattering of same-sign vector bosons has been deemed the most important production channel of four lepton final states [32]. This was in fact the first VBS process observed at the LHC [7, 8, 9]. In Refs. [26, 20, 28], it was shown that NLO EW corrections to W^+W^+ scattering are negative and their absolute value is larger than that of QCD and mixed corrections for the leptonic final state, which are also negative. In fact, large negative EW corrections appear to be a common characteristic of VBS processes at the LHC, as was predicted in Ref. [26] and confirmed in Refs. [30, 28].

Events that correspond to VBS processes in the LHC are mainly detected by targeting leptonic decays of the vector bosons as well as the remaining jets. However, there are other processes that lead to the same final state without involving the scattering of vector bosons. Such *background processes* can be very significant, and therefore pose a challenge for the experimental detection of VBS. To a certain extent, the background can be filtered out by concentrating the analysis on certain kinematic regions, where the contributions of the *signal process*, VBS, dominate. As will be reviewed in this work, the ratio of signal over background is improved in regions of the phase space with little jet activity in the central region, i.e. perpendicular to the collision beam. The understanding of jet kinematics is therefore crucial to correctly assess experimental results.

With this work, we aim to contribute to the understanding of a specific VBS process at the LHC with special focus on jet kinematics. We develop a software package to calculate the production of W^+W^+ associated with *three* jets at the LHC, $pp \rightarrow W^+W^+jjj$ and its QCD corrections. This allows us to investigate the kinematics of the third jet more precisely than previous calculations have, as well as to describe a fourth jet, produced by real radiation at NLO, using matrix elements. Furthermore, this calculation is matched to a parton shower using the POWHEG method [33, 34], which complements the matrix-element description of the fourth jet. An important difference between our fixed-order calculation and the calculations mentioned before is that the final state of our process includes two W^+ bosons, and not their decay products. Although the decays of the vector bosons may be simulated by the parton shower program that our fixed-order calculation is matched to, this approach is an approximation that neglects some correlations between the initial and full final state, i.e. the final state that includes the decay products of the W^+ bosons. This choice must be seen as a compromise that allows us to consider three jets already at LO, in accordance with our prioritization of the description of jet observables. Furthermore, we employ the aforementioned VBS approximation, which will be discussed and justified further below.

This thesis is structured in the following way. The first section consists of a review of Quantum Field Theory (QFT) in the context of the calculation of observables for collider experiments. In it, the notion of the *cross section* is introduced, and the problem of divergences in higher-order calculations is discussed. The principle of gauge invariance is touched upon, and the Standard Model (SM) of particle physics is shortly introduced. We then discuss topics relevant to hadron colliders: the concept of *factorization* in Quantum Chromodynamics (QCD) is outlined, and the structure of collision events in terms of different energy scales is presented. We end the first section by introducing the concept of jets.

Section 2 is concerned with the methods of NLO calculations and their matching to a parton shower. After presenting the general subtraction strategy for infrared divergences, the subtraction scheme of Frixione, Kunszt and Signer is outlined. Then, the concept of parton showers is introduced and the matching of NLO calculations to them using the POWHEG method is discussed.

In Sec. 3, we turn our focus to the scattering of W^+ bosons at the LHC and how it is realized within the $pp \rightarrow W^+W^+jjj$ process. After discussing the contributions to the whole process at LO and NLO, we motivate and define the VBS approximation that is employed in our calculation. The implementation of our calculation is discussed in detail in Sec. 4. In Sec. 5, which is closely based on Ref. [35], predictions achieved through our calculations are presented. After assessing the nature of the QCD correction, we investigate the effects of matching our NLO calculation with a parton shower. Finally, we summarize this work and give an outlook of possible follow-up and complementary investigations in the last section.

1 Theoretical Background

In this section we broadly outline how experimental observables may be calculated within the theoretical framework of perturbative Quantum Field Theory. We begin with Sec. 1.1 by introducing canonically quantized, free quantum fields and their correlation functions. Then, correlation functions of interacting fields are discussed and related to S -matrix elements in Sec. 1.1.2, which finally allow for the calculation of cross sections. In Sec. 1.3 we introduce the Standard Model of particle physics as a gauge theory and shortly summarize the mechanism of Electroweak Symmetry Breaking. Finally, in Sec. 1.4 we discuss the factorization property of QCD and the structure of hadronic collisions, as well as the concept of jets. These notions are crucial to understand the calculational methods that will be introduced in Sec. 2.

1.1 Quantum Field Theory

1.1.1 Fields and Green's Functions

The mathematical framework in high-energy physics is Quantum Field Theory (QFT). This framework combines classical field theory in its relativistic formulation with quantum mechanics. Classical fields are functions of space-time and have a definite behavior under Lorentz transformations. The main object in classical field theory is the Lagrangian density \mathcal{L} (or simply Lagrangian), a Lorentz scalar that is a function of the fields. From it, the equations of motion of the fields it contains can be derived via the Euler-Lagrange equation. Physical fields are those that fulfill the equations of motion. In this respect, a Lagrangian defines a theory. The role of the Lagrangian density is similar for a quantum field theory.

Whether or not the equations of motion derived from a Lagrangian are solvable depends on the terms that appear in \mathcal{L} . Often times, a Lagrangian is divided into a free part \mathcal{L}_0 and an interaction part \mathcal{L}_I , $\mathcal{L} = \mathcal{L}_0 + \mathcal{L}_I$. The free part contains terms that are bilinear in the fields and contain at least one derivative (kinetic terms) as well as bilinear terms of fields of the same type without derivatives (mass terms). The interaction part contains all other terms, which generally involve several different field types and powers higher than two. Typically, each interaction term carries a prefactor that includes a dimensionless *coupling*. The fields that fulfill the equations of motion that arise from \mathcal{L}_0 are called free. If the terms in \mathcal{L}_I are sufficiently small, the solutions of the equations of motion that arise from \mathcal{L} can be approximated using perturbation theory as series expansions truncated at a certain order of the couplings.

In QFT, classical fields are promoted to operators (or, more precisely, operator-valued distributions) that act on Fock space. This space of quantum mechanical states contains free one-particle states $|M, p, j, j_3\rangle$, which are characterized by a mass M , momentum p , spin j and third component of spin j_3 , as well as multi-particle states and a unique vacuum state of minimal energy.

Free quantum fields have the general form

$$\psi_\alpha(x) = \frac{1}{(2\pi)^3} \sum_{j_3} \int \frac{d^3\mathbf{p}}{2E_p} \left[u_\alpha(p, j_3) a_{j_3}(p) e^{-ipx} + v_\alpha(p, j_3) b_{j_3}^\dagger(p) e^{+ipx} \right]. \quad (1)$$

Here, α denotes the type of field and $E_p = \sqrt{M^2 + \mathbf{p}^2}$ is the zeroth component of the four momentum p . The coefficient functions $u_\alpha(p, j_3)$ and $v_\alpha(p, j_3)$, also called wave functions, describe the polarization degrees of freedom, and $u_\alpha(p, j_3)e^{-ipx}$ ($v_\alpha(p, j_3)e^{+ipx}$) are linearly independent solutions of the corresponding equations of motion. For scalar fields, the wave functions are unity. For spin-1/2 fields, they are Dirac spinors. For spin-1 fields, the wave functions are the polarization vectors $\varepsilon^\mu(p, j_3)$. Lastly, $a_{j_3}(p)$ is the operator that annihilates a particle with momentum p and third component of spin j_3 , and b^\dagger the creation operator of the corresponding antiparticle. These are the ladder operators from many-particle quantum theory, which act as follows on the unique and invariant free vacuum state $|0\rangle$

$$a_{j_3}^\dagger(p) |0\rangle = |M, p, j, j_3\rangle, \quad a_{j_3}(p) |0\rangle = 0,$$

and fulfill the (anti-)commutation relations

$$\left[a_{j_3}^\dagger(p), a_{j'_3}^\dagger(p') \right]_\pm = 0 = \left[a_{j_3}(p), a_{j'_3}(p') \right]_\pm, \quad (2)$$

$$\left[a_{j_3}(p), a_{j'_3}^\dagger(p') \right]_\pm = 2E_p (2\pi)^3 \delta(\mathbf{p} - \mathbf{p}') \delta_{j_3 j'_3}, \quad (3)$$

where $+$ holds for fermions and $-$ for bosons, and similarly for b and b^\dagger . Creation and annihilation operators of particles and antiparticles commute, as do the operators of different particle types. Thus, particles are quanta of the fields in the sense of Eq. (1). The commutation relations of Eqs. (2) and (3) lead to the following commutation relations for scalar fields:

$$[\psi_\alpha(x), \psi_\alpha(x')] = 0 = [\psi_\alpha^\dagger(x), \psi_\alpha^\dagger(x')] \quad (4)$$

$$[\psi_\alpha(x), \psi_\alpha^\dagger(x')] = \frac{1}{(2\pi)^3} \int \frac{d^3\mathbf{p}}{2E_p} \left(e^{-ip(x-x')} - e^{ip(x-x')} \right) \quad (5)$$

The expression on the right hand side of Eq. (5) vanishes if the separation of the points x and x' is spacelike, which is an expression of causality. It can be rewritten in terms of

$$\frac{1}{(2\pi)^4} \int d^4p \frac{i e^{-ip(x-x')}}{p^2 - M^2 + i\varepsilon} =: i \Delta_F(x - x', M), \quad (6)$$

with a positive ε and an implicit limit $\lim_{\varepsilon \rightarrow 0^+}$, and where the particles corresponding to the field ψ_α have a mass M . On the left hand side of Eq. (6), the zeroth component p^0 of the four-vector p is an integration variable, for which $p^0 = E_p$ does not hold.

1.1 Quantum Field Theory

Equation (6) defines the *Feynman propagator* Δ_F , which is a Lorentz-invariant function of only the difference $x - x'$.

The vacuum expectation value of time-ordered products of n quantum fields, each with its own spacetime argument, are called n -point (correlation) functions or Green's functions. They contain the physical information of a quantum field theory. From them, quantities can be derived that describe the scattering processes in collision experiments. We will now broadly outline this derivation. The simplest correlation function we can calculate is the 2-point function of a free scalar field of mass M ,

$$G_{\text{free}}(x_1, x_2) = \langle 0 | T \psi(x_1) \psi(x_2) | 0 \rangle$$

Here, T denotes the time ordering operator that acts like

$$\begin{aligned} \langle 0 | T \psi(x_1) \psi(x_2) | 0 \rangle &= \Theta(x_1^0 - x_2^0) \langle 0 | \psi(x_1) \psi(x_2) | 0 \rangle \\ &+ \Theta(x_2^0 - x_1^0) \langle 0 | \psi(x_2) \psi(x_1) | 0 \rangle . \end{aligned}$$

Using the representation of the Heaviside Θ function

$$\Theta(x) = \lim_{\varepsilon \rightarrow 0^+} \frac{i}{2\pi} \int_{-\infty}^{\infty} dy \frac{e^{-ixy}}{y + i\varepsilon} ,$$

one finds

$$\begin{aligned} G_{\text{free}}(x_1, x_2) &= \frac{i}{(2\pi)^4} \int d^4p \frac{1}{p^2 - M^2 + i\varepsilon} e^{-ip(x_1 - x_2)} \\ &= i \Delta_F(x_1 - x_2, M) , \end{aligned}$$

i.e. the free 2-point function of the scalar field is the Feynman propagator.

By Wick's theorem [36], correlation functions for higher n can be decomposed using the result for $n = 2$. The general n -point function is a sum of products of 2-point functions. For the free scalar field, it holds

$$G_{\text{free}}(x_1, \dots, x_n) = i^n \sum_i \Delta_F(x_{i_1} - x_{i_2}) \Delta_F(x_{i_3} - x_{i_4}) \cdots \Delta_F(x_{i_{n-1}} - x_{i_n}) , \quad (7)$$

where $i_k \in \{1, \dots, n\}$ and the sum runs over all distinct combinations. Similar results can be obtained for other particle types, whose 2-point functions are proportional to the Feynman propagator, but include other structures.

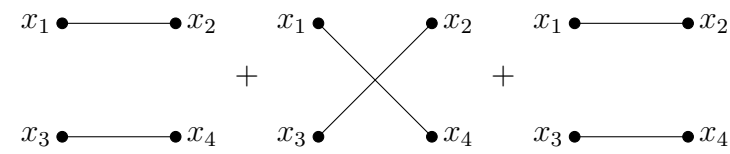
Correlation functions can be represented graphically with the following recipe. For a given n -point function with arguments x_k , $k = 1, \dots, n$ of the fields, a *field point* is drawn for each x_k . Then, each pair of points is joined by a line in every possible way, and a sum is built over all possibilities, each yielding a *diagram*. Each line represents i times a propagator of the particle kind that corresponds to the

fields that are involved. For the 2-point function of the free scalar field ψ_a , we obtain one diagram:

$$G_{\text{free}}(x_1, x_2) = x_1 \bullet \text{-----} \bullet x_2$$

$$= i \Delta_F(x_1 - x_2, M).$$

Similarly, we find three diagrams for the 4-point function:

$$G_{\text{free}}(x_1, x_2, x_3, x_4) =$$


$$= i^2 (\Delta_F(x_1 - x_2, M) \Delta_F(x_3 - x_4, M)$$

$$+ \Delta_F(x_1 - x_3, M) \Delta_F(x_2 - x_4, M)$$

$$+ \Delta_F(x_1 - x_4, M) \Delta_F(x_2 - x_3, M)).$$

These graphic representations are a mnemonic for the mathematical expressions that they stand for.

For a description of real-world QFTs, we need to extend our discussion to Green's functions of interacting fields,

$$G(x_1, \dots, x_n) = \langle \Omega | T \psi_H(x_1) \psi_H(x_2) \cdots \psi_H(x_n) | \Omega \rangle. \quad (8)$$

These contain fields in Heisenberg picture $\psi_H(x)$, whose time evolution is determined by the full Hamiltonian, including the interaction terms. The expectation value in Eq. (8) is with respect to the vacuum state $|\Omega\rangle$ of the interacting theory, which is different from $|0\rangle$. Luckily, Green's functions of the interacting theory can be related to those of the free theory, which we know how to calculate. This is achieved by the theorem of Gell-Mann and Low [37], which reads

$$\langle \Omega | T \psi_H(x_1) \psi_H(x_2) \cdots \psi_H(x_n) | \Omega \rangle = \frac{\langle 0 | T \psi(x_1) \psi(x_2) \cdots \psi(x_n) \exp \{ i \int dy \mathcal{L}_I(y) \} | 0 \rangle}{\langle 0 | T \exp \{ i \int dy \mathcal{L}_I(y) \} | 0 \rangle}. \quad (9)$$

The right hand side of Eq. (9) contains exponentials of the interaction lagrangian \mathcal{L}_I , which ultimately come from the translation from the Heisenberg to the interaction picture. A proof of the Gell-Mann and Low theorem can be found in [38], for example. In Eq. (9), \mathcal{L}_I contains quantum fields which are also subject to the time ordering enforced by T . The factors $\exp \{ i \int dy \mathcal{L}_I(y) \}$, understood as a series of operator products, can be expanded to a certain order of the couplings contained in \mathcal{L}_I to approximate the interacting Green's function on the left hand side. Once this has been done, the numerator on the right hand side of Eq. (9) becomes a sum of

1.1 Quantum Field Theory

Green's functions. Starting with the second term, the terms that result will contain products of fields with the same spacetime argument. We can exemplify this by discussing a simple example of interacting scalar fields with $\mathcal{L}_I = \lambda\psi^4$ and then expanding the exponential in the numerator of the right-hand side of Eq. 9 to the first order in the coupling λ :

$$\begin{aligned} \langle 0|T\psi(x_1)\psi(x_2)\cdots\psi(x_n)\exp\{i\int dy\mathcal{L}_I(y)\}|0\rangle &= \langle 0|T\psi(x_1)\psi(x_2)\cdots\psi(x_n)|0\rangle \\ &+ i\lambda\int dy\langle 0|T\psi(x_1)\psi(x_2)\cdots\psi(x_n)\psi(y)\psi(y)\psi(y)\psi(y)|0\rangle + \mathcal{O}(\lambda^2). \end{aligned} \quad (10)$$

As before, Wick's theorem can be used to decompose each term into a sum of products of 2-point functions, which can be graphically represented by lines and field points. An important difference to the case we have discussed before is the presence of several fields with the same argument. The corresponding field point is attached to more than one line. We will call these *internal points* or *vertices*, as opposed to the *external points* that are only attached to one line. Each vertex represents a factor $i\lambda$ and its position is integrated over. For the term of $\mathcal{O}(\lambda)$ in Eq. (10) with $n = 2$, we obtain

$$\begin{aligned} i\lambda\int dy\langle 0|T\psi(x_1)\psi(x_2)\psi(y)\psi(y)\psi(y)\psi(y)|0\rangle & \quad (11) \\ &= \int dy \left[3 \times \begin{array}{c} \text{---} \text{---} \text{---} \\ \bullet \quad \bullet \quad \bullet \\ x_1 \quad y \quad x_2 \end{array} + 12 \times \begin{array}{c} \text{---} \text{---} \\ \bullet \quad \bullet \\ x_1 \quad x_2 \end{array} \begin{array}{c} \text{---} \text{---} \\ \bullet \quad \bullet \\ \quad \quad y \end{array} \right] \\ &= i\lambda \left[i^3 3 \int dy \Delta_F(x_1 - y)\Delta_F(y - y)\Delta_F(y - x_2) + i^3 12\Delta_F(x_1 - x_2) \int dy (\Delta_F(y - y))^2 \right] \end{aligned}$$

The coefficients of each diagram in the second line of Eq. (11) are of combinatoric nature. Due to the presence of four fields with the same argument y , several forms of joining the field points and vertices lead to the same diagram. We have obtained two qualitatively different kinds of diagrams. The first one is fully connected, all vertices and field points are joined by at least one line to another one. The second one is not fully connected and, most importantly, contains a part which is made of vertices and lines that is not connected to any field point. Such parts are called *vacuum bubbles*. In this example, the only disconnected diagram contains a vacuum bubble. This is not a general property. Different interaction Lagrangians lead to correlation functions with all kinds of diagrams, which might not be fully connected but still not contain vacuum bubbles.

The right diagram in Eq. (11) translates to an expression in which the integrand does not depend upon any external point, i.e. the propagator that joins external points can be factorized. This is true for all diagrams that contain vacuum bubbles. In this way, one can factorize all vacuum bubbles of the whole numerator in Eq. (9). As it turns out [38], the vacuum bubbles exponentiate after being factorized. Crucially,

that exponential factor is cancelled by the denominator in Eq. (9), which contains no external points and thus can only lead to vacuum bubble diagrams. In this way, only diagrams without vacuum bubbles remain. That is, only diagrams without vacuum bubbles, which can be translated to products of propagators of free fields, contribute to the correlation functions of interacting fields:

$$\langle \Omega | T \psi_{\text{H}}(x_1) \psi_{\text{H}}(x_2) \cdots \psi_{\text{H}}(x_n) | \Omega \rangle = \left(\begin{array}{c} \text{sum of all diagrams with } n \\ \text{external points and no} \\ \text{vacuum bubbles} \end{array} \right). \quad (12)$$

At this point, we want to make a remark for completeness. In the last pages, we sketched a method to construct a quantum field theory by starting with a classical field theory and promoting the classical fields that appear in the corresponding Lagrangian \mathcal{L} to quantum fields. We defined free quantum fields using classical solutions of the equations of motion derived from \mathcal{L} and creation/annihilation operators of particle states. This leads to certain commutation relations that the fields fulfill. We then defined free correlation functions as vacuum expectation values of time ordered products of said quantum fields. To calculate general n -point functions, we decomposed them into sums of products of 2-point functions, for which analytic expressions have to be found for each type of field. We only cited the easiest case of a scalar particle of mass M . Then, using the Gell-Mann and Low formula, we found a perturbative and diagrammatic way to construct Green's functions of interacting fields using (parts of) those of free fields. This method is commonly called *canonical quantization*, and is not the only method there is to construct a quantum field theory.

One alternative method that leads to equivalent results is the so-called *path-integral quantization*, which is discussed in [39], for example. It is better suited to quantize massless vector fields, which appear in *gauge theories* (see Sec. 1.3) and contain unphysical degrees of freedom. If the massless vector field does not interact with itself, it can be canonically quantized by the ad-hoc addition of a *gauge-fixing term* to the Lagrangian density to constrain its unphysical degrees of freedom. If, on the other hand, the massless vector field can interact with itself, then its quantization becomes more involved and it must be done in the path-integral formalism. Thereby, unphysical *ghost fields* must be introduced. The path-integral method also leads to a closed formula for general Green's functions of interacting fields that is equivalent to Eqs. (9) and (12). More formally, the quantization of gauge theories can be achieved in the framework of *Becchi-Rouet-Stora-Tyutin* (BSRT) [40, 41], which is mathematically more rigorous than the path-integral method. A discussion of BSRT quantization is beyond the scope of this work, so we point to [38, 42] for an introduction to the topic.

We now turn to our last step towards physical observables in collision experiments, which is the discussion of the S -matrix and its relation to the Green's functions of interacting fields.

1.1 Quantum Field Theory

1.1.2 The S -matrix, Cross Sections and the Reduction Formula

The S -matrix describes the transition probabilities between two particle states in a scenario in which the interaction between particles is only possible in a certain region of space time, like in scattering experiments (hence the S). These states, called *in- and out-states*, are asymptotically defined to have a definite number of particles with definite momenta, along with other quantum numbers necessary to describe the particles. They behave like systems of non-interacting particles in times far enough from the scattering center in the past or future. Furthermore, they are independently complete in the Hilbert space, which implies the unitarity of the S -matrix [43].

Conventionally, the S -matrix is separated into a trivial part and a transition part. The trivial part describes forward scattering, and contributes to the scattering probability when the out-state is identical to the in-state. The transition part iT contributes if any particle undergoes real scattering. For the S -matrix element of the in-state $|\alpha\rangle_{\text{in}}$ and the out-state $|\beta\rangle_{\text{out}}$, we have

$$S_{\beta,\alpha} = {}_{\text{out}}\langle\beta|\alpha\rangle_{\text{in}} = \delta_{\beta\alpha} + iT_{\beta\alpha},$$

where we have summarized all quantum numbers of the in- and out-state, which need not be discrete, with α and β , respectively. The i factor that multiplies the transition matrix is a convention. The scattering probability is given by $|S_{\beta,\alpha}|^2$, as in quantum mechanics.

We will concentrate on the transition matrix T . As well as S , T should reflect momentum conservation. Thus, we can extract the corresponding δ -function and define the *invariant matrix element* \mathcal{M} as the remaining factor. For an in-state $|\alpha\rangle_{\text{in}}$ with two particles A and B and momenta p_A and p_B and an out-state $|\beta\rangle_{\text{out}}$ with n particles and total momentum p_f , we obtain

$${}_{\text{out}}\langle\beta|\alpha\rangle_{\text{in}} - \delta_{\beta\alpha} = iT_{\beta\alpha} = (2\pi)^4 \delta(p_A + p_B - p_f) i\mathcal{M}_{\beta\alpha}. \quad (13)$$

This $2 \rightarrow n$ scattering is the situation that corresponds to scattering experiments which we aim to describe, and we will assume it in the following discussion. Furthermore, we will assume that the spatial parts of p_A and p_B are parallel or antiparallel, i.e. along the beam axis of the collision experiment.

The invariant matrix element is a function of the incoming and outgoing momenta, as well as the other quantum numbers of the involved particles. It inherits the interpretation of the non-trivial scattering probability from the T -matrix, and can be used to define the *differential cross section* $d\sigma$ as

$$d\sigma = \frac{1}{4\sqrt{(p_A p_B)^2 - M_A^2 M_B^2}} \left[\prod_{i=1}^n \left(\frac{d^3 p_i}{(2\pi)^3 2E_i} \right) \right] (2\pi)^4 \delta \left(p_A + p_B - \sum_{k=1}^n p_k \right) |\mathcal{M}_{\beta\alpha}|^2. \quad (14)$$

The quantity $d\sigma$ represents the intrinsic probability that the in-state scatters into an out-state with n particles, whose momenta $\{p_i\}$ are each within a phase-space

volume $\frac{d^3 p_i}{(2\pi)^3 2E_i}$. The prefactor divides out the incoming flux of particles, which depends on the experimental setup, and is invariant under boosts along the beam axis. The rest of the expression is Lorentz-invariant. It is common to abbreviate the phase-space density in Eq. (14) with

$$d\Phi_n = \prod_{i=1}^n \left(\frac{d^3 p_i}{(2\pi)^3 2E_i} \right) \times (2\pi)^4 \delta \left(p_A + p_B - \sum_{k=1}^n p_k \right), \quad (15)$$

which is also called the Lorentz-invariant n -particle phase space. The invariant matrix element acts as a weight in this probability distribution. In the cross section, degrees of freedom that are not observed have to be averaged in the initial state and summed or integrated over in the final state. The integration of $d\sigma$ over a region of phase space yields the probability of scattering into that region. These are the quantities that can be measured in collision experiments.

Finally, we want to review the relation between the S -matrix and correlation functions. It is given by the *reduction formula* of Lehmann, Symanzik and Zimmermann (LSZ reduction) [44], which for a scalar field reads [42]

$$\begin{aligned} & \text{out} \langle -p_{s+1}, \dots, -p_n | p_1, \dots, p_s \rangle_{\text{in}} & (16) \\ & = R^{-n/2} (-i)^n (p_1^2 - M^2) \cdots (p_n^2 - M^2) \tilde{G}(p_1, \dots, p_n) \Big|_{p_i^2 = M_i^2} \\ & = R^{+n/2} \tilde{G}_0^{-1}(p_1, -p_1) \cdots \tilde{G}_0^{-1}(p_n, -p_n) \tilde{G}(p_1, \dots, p_n) \Big|_{p_i^2 = M_i^2} \\ & = R^{+n/2} \tilde{G}_{\text{trunc}}(p_1, \dots, p_n) \Big|_{p_i^2 = M_i^2}. \end{aligned}$$

The left hand side of Eq. (16) is an S -matrix element with an in-state defined by the momenta p_1, \dots, p_s and an out-state defined by the momenta $-p_{s+1}, \dots, -p_n$. On the right hand side, \tilde{G} is the Fourier-transform of the Green's function G with respect to all its arguments,

$$\begin{aligned} \tilde{G}(p_1, \dots, p_n) & = \int d^4 x_1 \cdots d^4 x_n e^{-i(p_1 x_1 + \cdots + p_n x_n)} G(x_1, \dots, x_n) \\ & = (2\pi)^4 \delta(p_1 + \cdots + p_n) \tilde{G}_0(p_1, \dots, p_n), \end{aligned}$$

also called momentum-space Green's function, and $R^{-1/2}$ is the *wave-function renormalization constant*. It is a number defined as

$$R = -i(p^2 - M^2) \tilde{G}_0(p, -p) \Big|_{p^2 = M^2}, \quad (17)$$

i.e. the residue at $p^2 = M^2$ of the Fourier-transformed 2-point function of interacting fields. This explains the second equality in Eq. (16). The third equality defines the *truncated Green's function in momentum space*, which we will discuss shortly.

We may summarize the content of the reduction formula as follows. The first equality in Eq. (16) says that the S -matrix element is the multiple residue of the Fourier-transformed Green's function at the poles where $p_i^2 = M_i^2$, multiplied

1.1 Quantum Field Theory

by the constant $R^{-1/2}$ for each particle. Recall that the p_i are arguments of $\tilde{G}(p_1, \dots, p_n)$ that correspond to the external points of $G(x_1, \dots, x_n)$, and the p_i^0 are not constrained. The limit $p_i^2 \rightarrow M_i^2$ is called the *on-shell limit*, as the condition $p^2 = M^2$, which is true for physical particles, defines a hypersurface (shell). In this sense, the S -matrix element corresponds to a momentum-space Green's function where external propagators have been replaced by physical particles. For particles with spin, the corresponding wave-functions have to be attached.

In the second equality in Eq. (16), the $(p_i^2 - M_i^2)$ factors have been replaced by inverse, fully interacting momentum-space 2-point functions, whose arguments correspond to external field points in position space. It is useful to think of these 2-point functions in terms of diagrams. Consider first the position-space 2-point function $\langle \Omega | T \psi_H(x_1) \psi_H(x_2) | \Omega \rangle$ of the scalar field, with the interaction $\mathcal{L}_I = \lambda \psi^4$ as an example. In Eq. (11) we have already seen the contribution of $\mathcal{O}(\lambda)$. We now want to consider all orders, dropping the vacuum bubbles as indicated by the Gell-Mann and Low theorem. Some of the diagrams at the lowest orders are

$$\begin{aligned}
 & \bullet \text{---} x_1 \text{---} \bullet \text{---} x_2 + \int dy \bullet \text{---} x_1 \text{---} \bullet \text{---} y \text{---} \bullet \text{---} x_2 + \int dy \int dz \left[\bullet \text{---} x_1 \text{---} \bullet \text{---} y \text{---} \bullet \text{---} z \text{---} \bullet \text{---} x_2 \right. \\
 & \left. + \begin{array}{c} \bullet \text{---} z \\ \bullet \text{---} y \\ \bullet \text{---} x_1 \text{---} \bullet \text{---} x_2 \end{array} + \begin{array}{c} \bullet \text{---} y \text{---} \bullet \text{---} z \text{---} \bullet \text{---} x_2 \\ \bullet \text{---} y \text{---} \bullet \text{---} z \text{---} \bullet \text{---} x_2 \end{array} \right] + \mathcal{O}(\lambda^3),
 \end{aligned}$$

where we have omitted combinatoric prefactors. The momentum-space correlation functions can be described by the same diagrams if we consider what happens to the correlation function upon Fourier-transformation and adapt the interpretation of the diagrams accordingly: Lines now represent the Fourier-transform of the free Feynman propagator, i.e. $i/[p^2 - M^2 + i\varepsilon]$ (cf. Eq. (6)). The integrals over internal positions (y and z above) yield δ -functions that reflect momentum conservation at the vertices. These can be integrated over when building the Fourier-transform to constrain some momenta. The integrals over unconstrained momenta remain.

In terms of diagrams, the effect of dividing by the 2-point functions in the second equality of Eq. (16) is to cut off those contributions that may be separated from the rest of the diagram by a single cut through an external line, as well as to eliminate diagrams with a disconnected part that only connects two external points. The diagrams that remain define the truncated momentum-space Green's functions and do not contain external points.

By Eq. (16), the S -matrix element can be expanded as a series in the couplings of the theory. The terms of the series are described by the diagrams that contribute to the corresponding orders of the truncated Green's function. This diagrammatic

representation carries over to matrix elements \mathcal{M} (cf. Eq. (13)). As opposed to the case of general Green's functions, it makes sense to say that the physical, incoming and outgoing particles in a reaction of a collision experiment are represented by external legs in diagrams of matrix elements. Internal lines are often denoted as *virtual particles*. On the one side, the propagators that these lines represent have a pole at the mass of the corresponding particle. They also “carry” a momentum and other quantum numbers for which conservation laws hold. In this sense they can be associated to a particle type. On the other hand, the energy-momentum relation does not hold for the argument p of these propagators, as it would for particles.

The rules that prescribe how to translate between matrix elements and diagrams are called *Feynman rules*, and the diagrams are commonly called *Feynman diagrams*. The rules are specific to the particles and interactions that they represent, and a list of the Feynman rules that are relevant to the process that we discuss in this thesis will be given in Sec. 1.3. Nevertheless, we can state the following general rules, which we have partly mentioned before:

1. External lines represent external particles and contribute the appropriate wave-function, which is a function of the particles momentum and spin.
2. Internal lines represent propagators (in the momentum representation), which have the general form $iC/[p^2 - M^2 + i\varepsilon]$. The numerator C is particle-type specific.
3. Lines that represent charged particles or fermions include an arrowhead that points in the direction of particle flow.
4. Vertices contribute a factor of i times the coupling of the interaction they represent. Momentum conservation holds at each vertex.
5. The momenta of *loop propagators*, i.e. those that are part of a closed loop in the diagram, are not determined by the external momenta and momentum conservation. These free momenta q_i must each be integrated over using $(2\pi)^{-4} \int d^4q_i$.

By Eq. (14), the cross section of the process $\alpha \rightarrow \beta$ can be computed in perturbation theory by expanding the corresponding matrix element $\mathcal{M}_{\beta\alpha}$ to a certain order, building its squared absolute value and integrating over the desired phase space. The $\mathcal{O}(k)$ contribution to the expansion of $\mathcal{M}_{\beta\alpha}$ corresponds to the sum of all possible diagrams connecting the particles in α and β that can be constructed using k vertices. Since each term of the expansion of $\mathcal{M}_{\beta\alpha}$ corresponds to Feynman diagrams, it makes sense to speak about “squared diagrams” or “interferences of diagrams”, which arise when building $|\mathcal{M}_{\beta\alpha}|^2$ and have a well-defined correspondence to mathematical expressions. We will use this terminology throughout this work.

Whether by applying the general Feynman rules cited above or by constructing \mathcal{M} from truncated Green's functions, one can quickly realize that some contributions to the matrix element diverge. By rule number 4, loop momenta are to be integrated over all possible values, which can be problematic for very low or very large momenta. Furthermore, the integration over phase space that is necessary to build observables

1.2 Divergences at Next-to-Leading Order

might not be well defined either. One way in which Feynman diagrams are useful is that they sometimes display in which regions of phase space the corresponding (squared) matrix element might be divergent. In the next section, we will discuss how observables can be calculated from quantum field theory despite these problems at *Next-to-Leading Order* (NLO) of perturbation theory.

1.2 Divergences at Next-to-Leading Order

As mentioned in the previous section, divergent integrals are encountered when we attempt to calculate observables in QFT. If we aim to make predictions using the methods described above, these divergences need to be handled.

In this chapter, we want to discuss the techniques that are employed to deal with this problem in perturbation theory, restricting our considerations to the leading and next-to-leading orders. We will distinguish two different types of divergences, namely *ultraviolet* (UV) and *infrared* (IR). UV divergences are those that arise from integrals over loop momenta in regions where the components of these momenta become very large. IR divergences encompass all other divergences, and may be further subdivided in the *soft* and *collinear* kinds. The names of these subcategories will become clear further below.

Conceptually, the treatment of divergences proceeds in two separate steps. The first one is called *regularization* and consists of the characterization of the divergences in a well defined manner that allows for mathematical manipulation. There are several regularization methods, but we will only discuss the commonly used *dimensional regularization* (DimReg), which has the advantage of being Lorentz invariant. It can be applied to regularize both types of divergences and will also be employed in this work. In the second step, the divergences are handled differently depending on their type. While UV divergences are absorbed by parameters of the Lagrangian, IR divergences are partially canceled against each other. We begin our discussion with UV divergences.

1.2.1 Loops and Ultraviolet Divergences

Before delving into the management of UV divergences, we want to say a few words about their origin in NLO calculations. As an example, we will consider a $2 \rightarrow n$ process with matrix element $\mathcal{M}_n(p_i)$ and external momenta p_i . We will assume for simplicity that only one coupling λ describes the interactions, and that vertices of diagrams are proportional to λ . We expand \mathcal{M}_n as

$$\mathcal{M}_n = \sum_{\ell=0}^{\infty} \mathcal{M}_n^{(k+2\ell)}, \quad (18)$$

in orders of λ ($\mathcal{M}^{(q)} \sim \lambda^q$). Furthermore, we assume that the diagrams that contribute to the leading (lowest) order term $\mathcal{M}_n^{(k)}$ are *tree diagrams*, i.e. they do

not contain loops. This is often the case for simple processes. Then, diagrams with one loop will contribute to $\mathcal{M}_n^{(k+2)}$, since two additional vertices are needed to add an internal line. Squaring Eq. (18), as we would to calculate a cross section, we obtain:

$$|\mathcal{M}_n|^2 = |\mathcal{M}_n^{(k)}|^2 + 2 \operatorname{Re} \left\{ \mathcal{M}_n^{(k+2)} (\mathcal{M}_n^{(k)})^* \right\} + \mathcal{O}(\lambda^{2k+2}). \quad (19)$$

The leading-order approximation of $|\mathcal{M}_n|^2$, i.e. truncating the expansion after the first order term $|\mathcal{M}_n^{(k)}|^2$, corresponds to the *Born approximation* from quantum mechanics. The second term on the right hand side of Eq. (18) contributes to $|\mathcal{M}_n|^2$ at next-to-leading order, and is often called the *virtual correction* or *virtual contribution*. As one can see, the virtual correction is proportional to the interference of a leading order and a next-to-leading order, one-loop matrix element. It is the integrals over loop momenta contained in $\mathcal{M}_n^{(k+2)}$ that can lead to UV divergences. These divergences can be made explicit by means of dimensional regularization, which we discuss in the following.

Dimensional regularization relies on the fact that the analytic structure of loop integrals allows for an analytic continuation to arbitrary complex spacetime dimensions d [42]. Furthermore, UV divergences arise for integer values of d . Thus, instead of performing divergent loop integrals in four dimensions, they are analytically continued to $d = 4 - 2\epsilon$ dimensions and then performed. The quantity ϵ that is thereby introduced parametrizes the departure from four dimensions and acts as a regulator. After integration, the UV divergences manifest themselves as negative powers of ϵ , so that the divergent structure is recovered in the limit $\epsilon \rightarrow 0$. To compensate for the change in mass dimension that is caused by the analytic continuation, the loop integrals are multiplied by a factor $(2\pi\mu)^{4-d}$, where the quantity μ with mass dimension is introduced. In this way, the coupling constants that appear in the Lagrangian remain dimensionless in d dimensions

To show this procedure in more detail, we consider the following, comparatively simple loop integral over the momentum k with mass m in d dimensions

$$\frac{1}{i\pi^2} \int d^4k \frac{1}{(k^2 - m^2 + i\varepsilon)^r} \rightarrow \frac{\mu^{4-d}}{i\pi^2} \int \frac{d^d k}{(2\pi)^{d-4}} \frac{1}{(k^2 - m^2 + i\varepsilon)^r} =: A_0^{(r)}(m) \quad (20)$$

which contains only one propagator to an arbitrary power $r \geq 1$. Before performing the integral, it is transformed from Minkowski space to Euclidean space by a *Wick rotation*. The integral along the real k^0 axis is substituted by an integral along the imaginary axis, which does not change the value of the integral by Cauchy's theorem. Then, the integration variables are substituted as $(k^0, \mathbf{k}) \rightarrow (ik_E^0, \mathbf{k}_E)$ by the *Euclidean momentum* k_E . This yields

$$A_0^{(r)}(m) = \frac{\mu^{4-d}}{\pi^2} \int \frac{d^d k_E}{(2\pi)^{d-4}} \frac{(-1)^r}{(k_E^2 + m^2 - i\varepsilon)^r}. \quad (21)$$

1.2 Divergences at Next-to-Leading Order

Then, spherical coordinates are introduced and the measure becomes

$$d^d k_E = \frac{1}{2} (k_E^2)^{(d-2)/2} dk_E^2 d\Omega_d, \quad (22)$$

with the solid-angle element in d dimensions $d\Omega_d$. Since there is no angular dependence in the integrand, the integral over $d\Omega_d$ can be performed, giving

$$\int d\Omega_d = \frac{2\pi^{d/2}}{\Gamma(d/2)},$$

with the *Gamma function* $\Gamma(z)$, which is defined for complex numbers z with a positive real part by

$$\Gamma(z) = \int_0^\infty dt t^{z-1} e^{-t}. \quad (23)$$

The Gamma function generalizes the factorial to non-natural numbers and has single poles at negative integers and zero. It also satisfies the functional equation $\Gamma(z+1) = z\Gamma(z)$. After the angular integration, we arrive at

$$A_0^{(r)}(m) = \frac{\mu^{4-d}}{\pi^2} \frac{2\pi^{d/2}}{\Gamma(d/2)} \frac{(-1)^r}{2(2\pi)^{d-4}} \int dk_E^2 \frac{(k_E^2)^{(d-2)/2}}{(k_E^2 + m^2 - i\varepsilon)^r}. \quad (24)$$

Lastly, we make the substitution $k_E^2 = (m^2 - i\varepsilon)\tau(1-\tau)$ in the integral of Eq. (24), which leads to

$$A_0^{(r)}(m) = \frac{\mu^{4-d}(4\pi)^{2-d/2}}{\Gamma(d/2)} (-1)^r (m^2 - i\varepsilon)^{d/2-r} \int_0^1 d\tau \tau^{d/2-1} (1-\tau)^{(r-d/2)-1}. \quad (25)$$

The remaining integral is a representation of the *Beta function*

$$B(z_1, z_2) = \int_0^1 d\tau \tau^{z_1-1} (1-\tau)^{z_2-1} = \frac{\Gamma(z_1)\Gamma(z_2)}{\Gamma(z_1+z_2)},$$

with $z_1 = d/2$ and $z_2 = r - d/2$. We plug the Beta function in terms of Gamma functions back into Eq. (25) to find

$$\begin{aligned} A_0^{(r)}(m) &= (4\pi\mu^2)^{(4-d)/2} \frac{\Gamma(d/2)\Gamma(r-d/2)}{\Gamma(d/2+r-d/2)\Gamma(d/2)} (-1)^r (m^2 - i\varepsilon)^{d/2-r} \\ &= (4\pi\mu^2)^{(4-d)/2} \frac{\Gamma(r-d/2)}{\Gamma(r)} (-1)^r (m^2 - i\varepsilon)^{d/2-r}. \end{aligned} \quad (26)$$

At this point, we can investigate the behavior of $A_0^{(r)}(m)$ close to the physical dimension four by setting $d = 4 - 2\varepsilon$ as mentioned before. We use the functional equation on the Gamma function in the numerator of Eq. (25) r times to shift the argument from $r - d/2 = r - 2 + \varepsilon$ to ε , as

$$\Gamma(r - 2 + \varepsilon) = \Gamma((r-1) - 2 + \varepsilon) \frac{1}{r-2+\varepsilon} = \Gamma(\varepsilon) \prod_{i=0}^{r-1} \frac{1}{r-i-2+\varepsilon}.$$

Then, we use the expansions for small ϵ

$$z^\epsilon = 1 + \epsilon \log z + \mathcal{O}(\epsilon), \quad \Gamma(\epsilon) = \frac{1}{\epsilon} - \gamma_E + \mathcal{O}(\epsilon),$$

where $\gamma_E \approx 0.577$ is the *Euler-Mascheroni constant*. For $r = 1$, this leads to

$$A_0^{(1)}(m) = m^2 \left(\frac{1}{\epsilon} - \gamma_E + \log 4\pi - \log \frac{m^2}{\mu^2} \right) + \mathcal{O}(\epsilon). \quad (27)$$

The divergence corresponding to $d \rightarrow 4$ has been regularized and is expressed as the pole $\frac{1}{\epsilon}$.

In practice, loop integrals can be significantly more complicated than our example. Loops that consist of several propagators yield integrands that are products of propagators, and are often denoted by the number of edges (propagators) that form the loop they correspond to. The integral in Eq. (20) with $r = 1$ corresponds to a *tadpole* diagram. A loop with two propagators is called a *self-energy* loop, and diagrams with higher numbers of edges are denoted as *triangles* for three propagators, *boxes* for four, *pentagons* for five and so on. With a technique called *Feynman parametrization*, the product in the denominator of such integrands can be rewritten as a sum. The general relation for a product of n propagators is

$$\frac{1}{D_1^{a_1} D_2^{a_2} \cdots D_n^{a_n}} = \frac{\Gamma(a_1 + a_2 + \cdots + a_n)}{\Gamma(a_1)\Gamma(a_2) \cdots \Gamma(a_n)} \times \int_0^1 dx_1 \cdots \int_0^1 dx_n \frac{\delta(1 - x_1 - \cdots - x_n) x_1^{a_1-1} \cdots x_n^{a_n-1}}{[x_1 D_1 + \cdots + x_n D_n]^{a_1 + \cdots + a_n}}, \quad (28)$$

where each D_i is the denominator of a propagator and a_i is its power. The cost of this transformation is the introduction of n integrals over the *Feynman parameters* x_i . In this way, loop integrals can be brought to the form of Eq. (20) and handled as we have seen above, with the further complication that the remaining Feynman integrals present.

Furthermore, when propagators of particles with nonzero spin are involved in the loop, the corresponding integrands can contain a tensorial structure from momenta in the numerator. These *tensor integrals* can be decomposed as linear combinations of basis tensors with coefficients that are scalar functions, for example via the *Passarino-Veltman reduction* method [45]. These scalar coefficients are themselves linear combinations of *scalar integrals* like that in Eq. (20), which contain no momenta in the numerator and can be handled as discussed above.

1.2.2 Renormalization

As we have seen at the top of the previous subsection, the method to calculate observable quantities can lead to divergent results when loop corrections are included. Therefore, it is unclear how to relate these results to actual measurements of physical

1.2 Divergences at Next-to-Leading Order

quantities without further considerations. If one were to solve for the parameters of a theory, like masses and couplings, by equating a divergent expression calculated to some order of perturbation theory to a (finite) measured physical quantity, the result would be divergent parameters.

Renormalization is a procedure in which these parameters are redefined, or *renormalized*. This reparametrization can be done by relating theoretical predictions to physical, measurable quantities, so that the physical interpretation of the parameters is more direct. Importantly, a reparametrization of a theory does not affect the relations between physical results. For *renormalizable* theories, an appropriate reparametrization of the theory leads to theoretical predictions that are finite and thus interpretable, it eliminates the UV divergences. The parameters of renormalizable theories can be redefined in a way that eliminates the UV divergences even if the new parameters do not have a direct physical interpretation.

Consider a theory with the unrenormalized Lagrangian $\mathcal{L}(\{\psi_{0,i}\}, \{g_{0,i}\})$, a function of fields $\psi_{0,i}$ and couplings $g_{0,i}$, which shall also summarize any masses that occur. Commonly, the reparametrization is done multiplicatively using *renormalization constants* Z_{ψ_i}, Z_{g_i} to relate *bare* parameters $\{\psi_{0,i}\}, \{g_{0,i}\}$ to *renormalized* parameters $\{\psi_i\}, \{g_i\}$ as

$$g_{0,i} = Z_{g_i}(g_i, \epsilon)g_i, \quad \psi_{0,i} = Z_{\psi_i}^{1/2}(g_i, \epsilon)\psi_i. \quad (29)$$

The bare parameters appear in the Lagrangian density and are divergent, whereas we require the renormalized parameters to be finite. Thus, the divergences are factorized into the renormalization constants. This is made evident in our notation by their dependence on the parameter ϵ from dimensional regularization. Since UV divergences come from loop corrections, we can expand the renormalization constants in the perturbative couplings g_i , which, up to NLO, gives

$$Z_{g_i}(g_i, \epsilon) = 1 + \delta Z_{g_i}(g_i, \epsilon), \quad Z_{\psi_i} = 1 + \delta Z_{\psi_i}(g_i, \epsilon). \quad (30)$$

After inserting Eqs. (29) and (30) into the Lagrangian, the latter can be decomposed as

$$\begin{aligned} \mathcal{L}(\{\psi_{0,i}\}, \{g_{0,i}\}) &= \mathcal{L}(\{(1 + \delta Z_{\psi_i})\psi_i\}, \{(1 + \delta Z_{g_i})g_i\}) \\ &= \mathcal{L}(\{\psi_i\}, \{g_i\}) + \mathcal{L}_{\text{ct}}(\{\delta Z_{\psi_i}\}, \{\delta Z_{g_i}\}, \{\psi_i\}, \{g_i\}). \end{aligned} \quad (31)$$

Note that no bare quantities appear on the right hand side of Eq. (31). The functional dependence of $\mathcal{L}(\{\psi_i\}, \{g_i\})$ on the renormalized quantities is as the one of $\mathcal{L}(\{\psi_{0,i}\}, \{g_{0,i}\})$ on the bare couplings, and the *counterterm Lagrangian* \mathcal{L}_{ct} , defined by Eq. (31), contains all divergences of $\mathcal{L}(\{\psi_{0,i}\}, \{g_{0,i}\})$. As the name suggests, the single terms contained in \mathcal{L}_{ct} are called *counterterms*. These can be treated as interaction terms, from which Feynman rules can be derived.

Once the UV-divergent diagrams of the theory have been identified, they can be made finite in the following way. The right hand side of Eq. (31) is used. Although

they are functions of renormalized parameters, the loop diagrams that result from $\mathcal{L}(\{\psi_i\}, \{g_i\})$ contain divergences that must be regularized. These contributions are added to those that result from the new interactions in \mathcal{L}_{ct} . Using *renormalization conditions*, the δZ_{ψ_i} and δZ_{g_i} are fixed in a way that cancels the UV divergences from $\mathcal{L}(\{\psi_i\}, \{g_i\})$ and renders the total result finite.

The requirement that the divergences cancel in a calculation only fixes the definition of the renormalization constants up to finite terms. The renormalization conditions are a set of equations that completely fix the renormalization constants, and they define a *renormalization scheme*. While a renormalization scheme may be formulated so that renormalized quantities have a direct physical interpretation, it does not need to be the case, as mentioned before. Often, the so-called *modified minimal subtraction* scheme, or $\overline{\text{MS}}$ scheme is chosen instead. In this scheme, the renormalization constants are chosen so that terms of the form

$$\frac{1}{\epsilon} - \gamma_E + \log 4\pi$$

are cancelled, which commonly arise in loops that have been dimensionally regularized, cf. Eq. (27).

In this way, UV divergences can be cancelled not only to NLO, but to all orders in perturbation theory. If only a finite number of counterterms is necessary to achieve this, the theory is called renormalizable.

Before discussing IR divergences, we remark that the renormalization procedure in the $\overline{\text{MS}}$ scheme makes the renormalized quantities dependent upon the quantity μ of mass dimension that was introduced during dimensional regularization. For example, for the renormalized coupling g it holds $g = g(\mu)$, which leads to the concept of the *running coupling*, to which we will return in Sec. 1.3.3.

1.2.3 Infrared Divergences and the KLN Theorem

After the calculation of an observable at NLO has been freed of UV divergences via renormalization, IR divergences might remain. These occur when virtual particles (loop lines) are attached to external lines and in regions of the integration domain in which the loop momentum approaches zero, in which case they are called soft, or when the loop momentum becomes collinear to the one of an adjacent line. Soft and collinear divergences can also overlap, and in that case they are called *soft-collinear*. IR divergences are often called *mass divergences* as well [42], since they can only occur if massless particles are involved in the loop. This is the case in physically relevant theories, as we will see later. We remark that the term IR divergences is sometimes used to refer to soft divergences only. Here, we call any divergence that is not of UV origin IR. Similarly, the term mass divergences sometimes refers to collinear singularities only.

Consider for simplicity a $2 \rightarrow n$ process with external momenta $k_1, k_2, p_1, \dots, p_n$ and a LO matrix element $\mathcal{M}_n^{(0)}$ that does not contain loops. As it turns out, the soft

1.2 Divergences at Next-to-Leading Order

divergences that arise from a one-loop matrix element $\mathcal{M}_n^{(1)}$ of the same process, its one-loop correction, can be factorized, so that in the soft limit one can schematically write

$$\mathcal{M}_n^{(1)}(k_1, k_2; p_1, \dots, p_n) \stackrel{\text{soft}}{\approx} I_v \cdot \mathcal{M}_n^{(0)}(k_1, k_2; p_1, \dots, p_n). \quad (32)$$

Here I_v is an IR-divergent integral and $\mathcal{M}^{(0)}$ is the matrix element that is obtained from $\mathcal{M}^{(1)}$ by removing the loop from which the soft divergence stems. In fact, it can be shown [46] that this factorization property leads to an exponentiation of the IR-divergent prefactor in the case of multiple loops whose momenta become soft, as long as all loops are joined to an external line.

In a way similar to Eq. (32), collinear divergences can be factorized from one-loop matrix elements. They can be regularized by giving a finite mass m to the particles to which the loop line is attached. In this case, the divergences appear as logarithmic prefactors of the matrix element without loop:

$$\mathcal{M}_n^{(1)}(k_1, k_2; p_1, \dots, p_n) \stackrel{\text{coll.}}{\approx} \log \frac{Q^2}{m^2} \cdot \mathcal{M}_n^{(0)}(k_1, k_2; p_1, \dots, p_n), \quad (33)$$

where Q is a kinematic quantity of the process with mass dimension, and the singularity is recovered for $m \rightarrow 0$. Even for a finite mass, these collinear regions are enhanced if $Q^2 \gg m^2$.

According to the *Kinoshita-Lee-Nauenberg* (KLN) theorem [47, 48], soft and collinear divergences are cancelled in observables if the sum over initial and final energy-degenerate states is performed in their calculation at a fixed order. These energy-degenerate final states include states with additional soft or collinear particles in the final state: it is impossible to distinguish a $2 \rightarrow n$ process from a $2 \rightarrow n + m$ process if the m extra particles have been emitted by external particles and have an energy close to zero. Also, if they are produced with momenta that are collinear to the momentum of other final-state particles, each group of collinear particles would be detected as a single particle with momentum equal to the group's total momentum. Observables that are constructed in a way that they are sufficiently insensitive to soft and collinear radiation, so that the IR cancellation occurs, are called *infrared safe*. The emission of extra soft or collinear particles produces IR divergences that factorize (and exponentiate) in the same way as those from loop contributions.

The KLN cancellation holds order by order in perturbation theory. In the context of NLO calculations, the energy-degenerate states that are to be taken into account in order to cancel IR loop divergences are those that contain one extra soft or collinear particle, and formally would correspond to a different, $2 \rightarrow (n + 1)$ process. Thus, to construct the infrared-safe NLO cross section of a $2 \rightarrow n$ process, it is necessary to take into account matrix elements $\mathcal{M}_n^{(0)}$, $\mathcal{M}_n^{(1)}$ and $\mathcal{M}_{n+1}^{(0)}$. Specifically, the squared modulus of the $n + 1$ matrix element, the *real (emission) contribution* $|\mathcal{M}_{n+1}^{(0)}|^2$, is added to the Born and virtual contributions of Eq. (19).

The phase-space integrations that are necessary to calculate the cross section from these squared matrix elements are different for the $2 \rightarrow n$ and $2 \rightarrow (n + 1)$ parts.

While the Born and virtual contributions need to be integrated over an n -particle phase space, the real contribution is to be integrated over an $n + 1$ -particle phase space, and only the sum of all integrals is IR-finite. A regularization method can be used to express the IR divergences in the different integrals as $1/\epsilon$ -poles and analytically cancel the singularities. In the real contribution, they only arise upon the integration over the phase space of the extra particle in the real correction. Thus, a decomposition of the $n + 1$ -particle phase space into an n -particle phase space and a one-particle, so-called *radiation phase space* is necessary. This cancellation is particularly complicated to perform in numerical calculations, and a sketch of the method employed in this work to that end will be given in Sec. 2.1.

Before ending this section, we remark that the cancellation of IR divergences in the sum of virtual and real contributions is not complete if the initial-state particles are massless and can emit other particles. This is the case in physically relevant theories, so there are methods to deal with these remaining singularities. The left-over divergences correspond to non-soft, collinear emissions from the initial state which are not cancelled by the corresponding IR loop divergences. The reason for this non-cancellation can be intuitively understood after considering the factorization properties mentioned above. The factorization properties from Eqs. (32) and (33) lead to analogous expressions at the cross-section level for virtual and real corrections. The real soft emission of an $(n + 1)$ -th particle factorizes as

$$\sigma_r(k_1, k_2; p_1, \dots, p_{n+1}) \stackrel{p_{n+1} \text{ soft}}{\approx} I_r \cdot \sigma_B(k_1, k_2; p_1, \dots, p_n)$$

where the subindices stand for real and Born, respectively. On the right hand side, I_r is an integral that carries the soft divergence, and the Born cross section σ_B that it multiplies is a function of the momenta that remain when p_{n+1} goes to zero. σ_B corresponds to the Born cross section that multiplies the virtual soft divergence after factorization, cf. Eq. (32). This is independent of the origin of the soft particle.

For a collinear emission, where the emitted particle carries away a fraction x of the energy of the emitter, this is not the case. On the contrary, the kinematics upon which the factorized Born cross section depends are influenced by the origin of the emission. If the $(n + 1)$ -th particle is emitted from the n -th final-state particle, the underlying Born process with matrix element $\mathcal{M}_n^{(0)}$ depends upon the $n + 2$ momenta $k_1, k_2, p_1, \dots, p_{n-1}, \tilde{p}_n$ where $\tilde{p}_n = p_n + p_{n+1}$, i.e. \tilde{p}_n is the momentum of the n -th particle “before” the emission. These are also the momenta upon which the factorized Born cross section from the virtual correction depends, where there is no extra emission.

If, on the other hand, the $(n + 1)$ -th particle is emitted by the initial state, say by the particle with momentum k_1 , so that $p_{n+1} = xk_1$, then the factorized Born cross section depends on the momenta $(1 - x)k_1, k_2, p_1, \dots, p_n$. These are not the momenta upon which the factorized Born cross section from the virtual correction depends, but correspond to a process with less total incoming energy. Thus, there is a mismatch between the prefactors of the virtual and initial-state collinear, real

1.3 Gauge Theories and the Standard Model

divergences, and they can't possibly cancel. A solution to this problem is presented in Section 1.4.

1.3 Gauge Theories and the Standard Model

After a short general discussion of gauge theories, we turn to the Standard Model of particle physics, the QFT that has been most successful in describing high-energy phenomena. We describe the field and particle content of this theory and cite its Lagrangian and the Feynman rules that can be derived from it for the construction of matrix elements.

In field theory, the *action* S of a given theory is given by the integral of its Lagrangian density \mathcal{L} over the whole of spacetime, $S = \int d^4x \mathcal{L}$. The continuous *symmetries* of the action are very important for the theory, because they are linked to the existence of conservation laws by Noether's first theorem. A symmetry is defined as a certain transformation of the fields under which the Lagrangian \mathcal{L} is invariant. The action is invariant under a transformation of the fields if the corresponding Lagrangian is invariant up to total divergences, so often the symmetries of the Lagrangian are directly investigated. Specifically, Noether's theorem states that if S is invariant under a continuous *global transformation* of the field, described by a set of parameters $\{\theta_a\}$, then a set of vector quantities arises, often called *currents*, which fulfill continuity equations. The zeroth components of the currents, often called *charges*, are then conserved in time.

From space-time or *external* symmetries, i.e. the Lorentz-invariance of the Lagrangian, the conservation of energy, momentum and angular momentum can be derived. Similarly, the conservation of electric charge follows from the invariance of the Lagrangian of electromagnetism under transformations that rotate the (complex-valued) fields in the complex plane. These transformations are just the multiplication by a complex number, belonging to the symmetry group of unitary, one-dimensional matrices $U(1)$.

Groups of continuous transformations are mathematically described by *Lie groups*. Any one element g of a Lie group G can be written as an exponent of a linear combination of the groups *generators* Q^a , which are themselves elements of the *Lie algebra* \mathfrak{g} . The number of generators of a group corresponds to the group's dimension, i.e. the number of parameters that are necessary to describe a group element. These parameters may be chosen as the coefficients of the aforementioned linear combination, so that

$$g(\{\theta_a\}) = \exp[i\theta^a Q^a], \quad (34)$$

where the factor i is a convention. The generators of a symmetry group fulfill commutation relations

$$[Q^a, Q^b] = i f^{abc} Q^c, \quad (35)$$

where the f^{abc} are the group's *structure constants*. Furthermore, the generators are related to the conserved charge that arises if a Lagrangian is invariant under that symmetry group.

The importance of global symmetries motivates the study of *local* symmetries, for which the parameters that describe the field transformations are functions of space time, $\{\theta_a(x)\}$. A Lagrangian that is invariant under a certain global transformation with parameters $\{\theta_a\}$ will generally not be invariant if one simply replaces $\theta_a \rightarrow \theta_a(x)$. On the other hand, the invariance can be recovered if new fields are introduced to counteract the effects of the locality of $\theta_a(x)$ that arise upon a transformation. These new fields are called *gauge fields*, and their introduction naturally produces new interaction terms in the Lagrangian density. One can then add corresponding gauge-invariant kinetic terms for the gauge fields and interpret them as particle fields. Crucially, no gauge-invariant mass terms for the gauge fields can be introduced “by hand”, so the corresponding particles must be massless. A local version of the $U(1)$ transformation mentioned above is an example of a *gauge transformation*, and the electromagnetic Lagrangian is *gauge invariant* under it.

We now exemplify these concepts using the prototypical symmetry group $SU(N)$ of unitary matrices with unit determinant, which is a compact Lie group with $N^2 - 1$ generators T^a . These generators are elements of $\mathfrak{su}(N)$, the Lie algebra of $SU(N)$. We consider a set of N fields $\psi_i(x)$, $i = 1, \dots, N$, that transforms under the N -dimensional fundamental representation U of $SU(N)$. For the group element $g \in SU(N)$:

$$\psi_i(x) \rightarrow U(g)_{ij} \psi_j(x) = \exp [i\theta^a T^a]_{ij} \psi_j(x). \quad (36)$$

If we make the transformation local, $g \rightarrow g(x)$, then Eq. (36) becomes

$$\psi_i(x) \rightarrow U(g(x))_{ij} \psi_j(x) = \exp [i\theta^a(x) T^a]_{ij} \psi_j(x), \quad (37)$$

and it is necessary to introduce a vector field $A_\mu(x)$ which transforms as

$$A_\mu(x) \rightarrow U(x)(i\partial_\mu + A_\mu(x))U^{-1}(x), \quad (38)$$

where we have abbreviated $U(x) = U(g(x))$. The Lorentz components of A_μ are elements of $\mathfrak{su}(N)$ and can be expressed in the same representation U as a linear combination of the generators T^a :

$$A_{\mu,ij}(x) = qA_\mu^a(x)T_{ij}^a. \quad (39)$$

The common, constant factor q is called *coupling*. The $N^2 - 1$ vector fields $A_\mu^a(x)$ are the *components* of $A_\mu(x)$, i.e. the coefficients of the generators. The component fields $A_\mu^a(x)$ transform under the $N^2 - 1$ -dimensional adjoint representation of $SU(N)$, which can be constructed from the structure constants.

The gauge field $A_\mu(x)$ is introduced into the Lagrangian density via the *covariant derivative* $D_\mu := \partial_\mu - iA_\mu(x)$, which in components reads

$$D_{\mu,ij} := \partial_\mu \delta_{ij} - igA_\mu^a(x)T_{ij}^a, \quad (40)$$

1.3 Gauge Theories and the Standard Model

and replaces the standard derivatives ∂_μ in the kinetic terms of the fields $\psi_i(x)$. The kinetic term of $A_\mu(x)$ has the form

$$-\frac{1}{2g} \text{Tr} [F_{\mu\nu}(x)F^{\mu\nu}(x)] \quad (41)$$

and is given in terms of the *field-strength tensor*

$$F_{\mu\nu}(x) = i [D_\mu(x), D_\nu(x)] = \partial_\mu A_\nu(x) - \partial_\nu A_\mu(x) - i [A_\mu(x), A_\nu(x)] , \quad (42)$$

which reads in components

$$F_{\mu\nu}^a(x) = \partial_\mu A_\nu^a(x) - \partial_\nu A_\mu^a(x) - igf^{abc}A_\mu^b(x)A_\nu^c(x) . \quad (43)$$

The structure constant in the third term of the right hand side of Eq. (43) comes from the commutator of generators that follows from Eq. (42). If the symmetry group were commutative, this term would not arise. The presence (or absence) of this term has important consequences for the theory. These are derived from the fact that, when the term is present, the Lagrangian will contain self-interaction terms of the fields $A_\mu^a(x)$.

The considerations described so far apply to classical fields. While they carry over to quantum fields, care has to be taken in the quantization of the massless vector fields that are introduced in gauge theories, as was mentioned in Sec. 1.1.1. The renormalizability of *Yang-Mills theories*, i.e. of gauge theories based on a compact Lie group, was proved by t'Hooft in [49], and the proof was extended to *spontaneously broken* Yang Mills theories shortly after [50].

1.3.1 The Standard Model

During the past century, gauge quantum field theories were developed to understand the forces that govern particle physics. On the one hand, Quantum Chromodynamics (QCD) was put forward as the theory of strong interactions. During its development, a quantum number that can assume three values, called *color*, was introduced, which finally gave the theory its name. Particles that are described by QCD, i.e. those that interact strongly, are said to be *color charged*. In its final formulation, QCD is a gauge theory with the underlying symmetry group $SU(3)$, and strongly interacting fields transform according to a representation of this group. The dimension of the fundamental representation, 3, is often written as N_C , the *number of colors*.

On the other hand, the electromagnetic and weak forces are both described by the *Glashow-Weinberg-Salam* model, which unifies both interactions at large energies. It is a gauge theory with the symmetry group $SU(2) \times U(1)$, but the gauge fields that it contains are both massless and massive, as opposed to those of QCD. This is achieved via the process of *Electroweak Symmetry Breaking* (EWSB), which will be discussed further below.

The Standard Model (SM) of particle physics consists of QCD and the electroweak model, and gives a description of the forces of nature, with the important

exception of gravity. It is itself a gauge QFT with the product symmetry group $SU(3) \times SU(2) \times U(1)$.

The SM contains 12 spin-1/2 *matter fields*, 12 spin-1 gauge fields or *force carriers* and a spin-0 scalar field, the Higgs field. These fields (or linear combinations thereof) are associated to particles. The 12 fermions are divided into 6 *quarks* and 6 *leptons*, according to their behavior under $SU(3)$ transformations. While both quark and lepton fields transform non trivially under $SU(2)$, lepton fields are singlets of $SU(3)$, meaning that quarks carry a color charge, while leptons do not.

Generally, a Dirac field ψ that describes a fermion can be decomposed in left- and right-handed chirality eigenstates $\psi = \psi_L + \psi_R$ by the projectors $P_{L/R} = (1 \mp \gamma^5)/2$. $SU(2)$ transformations act differently on these left- and right-handed parts. The left-handed parts of the lepton fields are organized in three $SU(2)$ doublets

$$L_n = \begin{pmatrix} \nu_{L,n} \\ e_{L,n} \end{pmatrix}, \quad (44)$$

where $n = 1, 2, 3$ is the *generation number*, $\nu_{L,n}$ and $e_{L,n}$ are the left-handed parts of the neutrino and electron-type fields ν_n and e_n , respectively. Similarly, the left-handed parts of the quark fields form the three doublets

$$Q_n = \begin{pmatrix} u_{L,n} \\ d_{L,n} \end{pmatrix}, \quad (45)$$

with the left-handed parts of the up- and down-type quark fields u_n and d_n . The right-handed parts of the matter fields $u_{R,n}$, $d_{R,n}$, and $e_{R,n}$, on the other hand, are singlets of $SU(2)$. For the case of neutrinos, the right-handed part is not present in the SM. The fermions of each generation have specific names. Instead of “quarks of u -type of the first, second and third generation”, they are typically called “up, charm and top” (u, c, t). The d -type quarks receive the names “down, strange and bottom” (d, s, b). Similarly, the electron-type fields are called “electron, muon and tauon” (e, μ, τ), and the corresponding neutrino-type fields are “electron-, muon- and tauon-neutrino” (ν_e, ν_μ, ν_τ). These 12 unique fermion labels are called *flavors*.

Before EWSB, the SM contains the components W_μ^a , $a = 1, 2, 3$ and B_μ of the gauge fields of $SU(2)$ and $U(1)$. The corresponding components of the field-strength tensors are

$$F_{1,\mu\nu} = \partial_\mu B_\nu - \partial_\nu B_\mu, \quad (46)$$

$$F_{2,\mu\nu}^a = \partial_\mu W_\nu^a - \partial_\nu W_\mu^a + g_2 \varepsilon^{abc} W_\mu^b W_\nu^c, \quad (47)$$

where ε^{abc} are the components of the Levi-Civita tensor, the structure constants of $SU(2)$. The absence of a third term in the equation for $F_{1,\mu\nu}$ reflects the commutativity of $U(1)$. After EWSB, combinations of W_μ^a and B_μ will correspond to the physical photon and electroweak bosons.

The remaining eight force-carrier fields are the components G_μ^a of the gauge field of $SU(3)$, called gluon fields, which carry a color charge themselves. Their

1.3 Gauge Theories and the Standard Model

field-strength tensors are

$$F_{s,\mu\nu}^a = \partial_\mu G_\nu^a - \partial_\nu G_\mu^a + g_s f^{abc} G_\mu^b G_\nu^c, \quad (48)$$

with the structure constants of $SU(3)$, of which only the following are non-zero:

$$\begin{aligned} f^{123} = 1, \quad f^{458} = f^{678} = \frac{\sqrt{3}}{2}, \\ f^{147} = -f^{156} = f^{246} = f^{257} = f^{345} = -f^{367} = \frac{1}{2}. \end{aligned} \quad (49)$$

The gauge fields form the covariant derivative

$$D_\mu = \partial_\mu + ig_1 \frac{Y}{2} B_\mu - ig_2 \frac{\tau^a}{2} W_\mu^a + ig_s T^b G_\mu^b, \quad (50)$$

with the couplings g_1 and g_2 and the *strong coupling* g_s . The *hypercharge* Y is the generator of the $U(1)$ symmetry group, the three τ^a are those of $SU(2)$ and the eight T^a the ones of $SU(3)$. In the fundamental representation, one chooses the Pauli matrices for τ^a . The T^a are represented by $1/2$ times the *Gell-Mann matrices* λ^a ,

$$T^a = \lambda^a / 2. \quad (51)$$

The Gell-Mann matrices are traceless, $\text{Tr}[\lambda^a] = 0 \forall a$, and fulfill the relations

$$\text{Tr}[\lambda^a \lambda^b] = \delta^{ab} \quad \text{and} \quad (52)$$

$$(\lambda^a)_{ij} (\lambda^a)_{kl} = \delta_{il} \delta_{jk} - \frac{1}{N_C} \delta_{ij} \delta_{kl}. \quad (53)$$

The covariant derivative of Eq. (50) appears in the kinetic terms of the matter fields

$$\mathcal{L}_{\text{matter}} = \bar{L}_n i \not{D} L_n + \bar{Q}_n i \not{D} Q_n + \bar{e}_{R,n} i \not{D} e_{R,n} + \bar{d}_{R,n} i \not{D} d_{R,n}, \quad (54)$$

where \bar{L}_n, \bar{Q}_n are the Dirac adjoint fields of L_n, Q_n and we have used the slash notation $\not{D} = \gamma^\mu D_\mu$. In Eq. (54), the sum over the generation index n is implicit. Before EWSB, there are no mass terms for the matter fields. The interaction terms between gluons and quarks that result from $\mathcal{L}_{\text{matter}}$ are

$$-g_s \sum_q \bar{\psi}_{q,i} \gamma^\mu T_{ij}^a G_\mu^a \psi_{q,j}, \quad (55)$$

where $\psi_{q,i}$ is the Dirac spinor of a quark with flavor q and color charge $i = 1, 2, 3$. This interaction involves a rotation in color space produced by T^a . Unlike the other massless gauge boson, the photon, the gluons carry a (color) charge and can interact

with themselves. The couplings between the matter fields and the other gauge bosons will be discussed after EWSB.

Lastly, the SM contains the Higgs complex scalar field ϕ which transforms as a doublet under $SU(2)$ and is a $SU(3)$ singlet:

$$\phi = \begin{pmatrix} \phi^+ \\ \phi^0 \end{pmatrix}. \quad (56)$$

It contributes to the Lagrangian of the SM with its kinetic and potential terms

$$\mathcal{L}_\phi = (D_\mu \phi)^\dagger (D^\mu \phi) - V(\phi^\dagger \phi), \quad (57)$$

where D_μ is as in Eq. (50) and the Higgs potential is given by

$$V(\phi^\dagger \phi) = \lambda [\phi^\dagger \phi - \mu^2/2\lambda]^2, \quad (58)$$

with the real parameters μ^2 and λ , $\lambda > 0$. The Higgs field couples to the fermion fields according to the interaction terms

$$\mathcal{L}_{\text{Yukawa}} = y_{ij}^e \bar{L}_i \phi e_{R,j} + y_{ij}^d \bar{Q}_i \phi d_{R,j} + y_{ij}^u \bar{Q}_i \tilde{\phi} u_{R,j} + \text{h.c.}, \quad (59)$$

where

$$\tilde{\phi} = \begin{pmatrix} \phi^{0*} \\ -\phi^{+*} \end{pmatrix} \quad (60)$$

and the *Yukawa couplings* y^e , y^d and y^u are matrices in the space of fermion generations.

1.3.2 Electroweak Symmetry Breaking

The electroweak $SU(2) \times U(1)$ symmetry of the SM is broken and reduced to a $U(1)$ symmetry via the Brout-Englert-Higgs mechanism. Thereby, mass terms for the fermions and weak vector bosons are generated in the SM Lagrangian in a gauge-invariant way. The mechanism consists of the introduction of the Higgs field ϕ as stated above, and of the choice $\mu^2 > 0$ for the Higgs potential in Eq. (58). Then, V is minimized by field configurations with

$$\phi^\dagger \phi = \mu^2/(2\lambda) =: v^2/2, \quad (61)$$

where v is called the *vacuum expectation value* (vev). Then, gauge freedom can be exploited to perform a transformation at every point in spacetime to restrict the field ϕ to its lower component and rewrite

$$\phi = \begin{pmatrix} 0 \\ \frac{1}{\sqrt{2}}(v + h(x)) \end{pmatrix}, \quad (62)$$

1.3 Gauge Theories and the Standard Model

with the real excitation field $h(x)$ around v . This choice, called *unitary gauge*, makes the rest of the procedure more transparent.

Equation (62) is then inserted in Eqs. (57) and (59). The kinetic term of the Higgs fields yields

$$(D_\mu\phi)^\dagger(D^\mu\phi) = \frac{1}{2}[\partial_\mu h]^2 + \frac{g_2^2 v^2}{4} [(W_\mu^1)^2 + (W_\mu^2)^2] + \frac{v^2}{8} [(g_2 W_\mu^3 - g_1 B_\mu)^2] + \text{higher orders in the fields.} \quad (63)$$

Aside from the kinetic term of $h(x)$, one can recognize the mass terms for the fields W_μ^1 and W_μ^2 . Although the Higgs mechanism generates mass terms for them, the W_μ^1 and W_μ^2 fields mix under electroweak transformations. Therefore, they are combined to

$$W_\mu^\pm = \frac{1}{\sqrt{2}}(W_\mu^1 \mp iW_\mu^2), \quad (64)$$

which are eigenstates of the left-over $U(1)$ -electromagnetic symmetry, where $+$ and $-$ correspond to particle and antiparticle respectively.

Equation (63) also contains a mass term for the linear combination $(g_2 W_\mu^3 - g_1 B_\mu)$, suggesting that it represents a physical field. The weak mixing angle θ_W is defined by

$$\tan \theta_W := g_1/g_2 \quad (65)$$

and is used to parametrize the two independent linear combinations of W_μ^3 and B_μ as the new fields Z_μ and A_μ , defined as

$$\begin{pmatrix} Z_\mu \\ A_\mu \end{pmatrix} := \begin{pmatrix} \cos \theta_W & -\sin \theta_W \\ \sin \theta_W & \cos \theta_W \end{pmatrix} \begin{pmatrix} W_\mu^3 \\ B_\mu \end{pmatrix}.$$

While a mass term is generated for Z_μ , A_μ remains massless after EWSB. The W_μ^\pm , Z_μ and A_μ fields are the physical fields that correspond to the particles we observe: the electrically charged W^+ and W^- bosons, the neutral Z boson and the massless photon γ ². These identifications are justified by the coupling of these bosons to the matter fields, as we will see below. The mass parameters of the weak bosons then read

$$M_W = \frac{g_2 v}{2}, \quad M_Z = \frac{g_2 v}{2 \cos \theta_W} = \frac{M_W}{\cos \theta_W},$$

and are directly proportional to the vev of the Higgs field. Among the higher-order terms on the right hand side of Eq.(63) there are triple and quartic couplings between the Higgs field and the weak vector bosons:

$$-\left(\frac{h}{v} + \frac{h^2}{v^2}\right) (2M_W^2 W^{+\mu} W_\mu^- + M_Z^2 Z^\mu Z_\mu). \quad (66)$$

²While the letter A is commonly used to denote the photon field, the particle is more often represented by the letter γ .

Inserting Eq.(62) into the Higgs potential of Eq. 58, one obtains the self-interaction terms of the Higgs field

$$\lambda v^2 h^2 + \lambda v h^3 + \frac{\lambda}{4} h^4 \quad (67)$$

from which the Higgs boson mass can be read.

$$m_h = \sqrt{2\lambda v^2}. \quad (68)$$

The field-strength tensors of all gauge fields are part of the Lagrangian according to Eq.(41). In components, these terms are

$$\mathcal{L}_{\text{gauge}} = -\frac{1}{4} G_{\mu\nu}^a G^{a,\mu\nu} - \frac{1}{4} W_{\mu\nu}^a W^{a,\mu\nu} - \frac{1}{4} B_{\mu\nu} B^{\mu\nu}. \quad (69)$$

The first term in Eq. (69) includes the kinetic and self-interaction terms of the gluon field. After EWSB, the second and third terms yield the triple and quartic couplings of the physical fields in the following combinations:

$$W^+W^-Z, \quad W^+W^-A, \quad \text{and} \\ W^+W^-W^+W^-, \quad W^+W^-ZZ, \quad W^+W^-AA, \quad W^+W^-ZA.$$

We now turn to the Yukawa terms of Eq. (59) after Eq. (62) is used. The Yukawa couplings y^e , y^u and y^d can be diagonalized so that a mass term is generated for each of the fermions, with the exception of the neutrinos. From now on, we assume this has been done and refer to the mass eigenstates. For the first generation of leptons, for example, one finds

$$y^e (\bar{L}\phi e_R + \bar{e}_R\phi^\dagger L) = \frac{y^e}{\sqrt{2}} (\bar{e}_L v e_R + \bar{e}_R v e_L) + \frac{y^e}{\sqrt{2}} (\bar{e}_L h e_R + \bar{e}_R h e_L). \quad (70)$$

The first term on the right hand side of Eq. (70) has the form of a mass term, since

$$m\bar{e}e = m\bar{e}(P_L + P_R)e = m\bar{e}(P_L e_L + P_R e_R) = m(\bar{e}_R e_L + \bar{e}_L e_R),$$

so we interpret the factor $y^e v/\sqrt{2}$ as the electron mass. The second term describes the interaction of the physical Higgs field $h(x)$ with the fermion.

In the process of diagonalizing the Yukawa couplings, all terms in the Lagrangian where the matter fields appear can remain unchanged except for one kind. This exception are the interaction terms of quarks with the W^\pm bosons which result from the covariant derivatives in $\mathcal{L}_{\text{matter}}$. They are

$$-\frac{g_2}{2^{3/2}} \sum_n \bar{Q}'_n \gamma^\mu (W_\mu^+ \tau^+ + W_\mu^- \tau^-) Q'_n, \quad (71)$$

1.3 Gauge Theories and the Standard Model

where

$$Q'_n = \begin{pmatrix} u_{L,n} \\ d'_{L,n} \end{pmatrix} \quad (72)$$

and the τ^\pm are the weak-isospin raising and lowering operators

$$\tau^+ = \begin{pmatrix} 0 & 1 \\ 0 & 0 \end{pmatrix}, \quad \tau^- = \begin{pmatrix} 0 & 0 \\ 1 & 0 \end{pmatrix}. \quad (73)$$

The term in Eq. (71) is contained in Eq. (54). In this *charged-current interaction*, it is not the mass eigenstates of the d_L -type quark fields that appear, but linear combinations of them of the form $d'_{L,i} = \sum_j V_{ij} d_{L,j}$. The coefficients V_{ij} are elements of the *Cabibbo-Kobayashi-Maskawa* (CKM) matrix, which is described by four physical parameters and is very close to being a unit matrix [51]. Due to the non-diagonal elements of the CKM matrix, the charged-current interaction can change the generation of a quark. Even for a diagonal CKM matrix, this interaction changes the flavor of a quark within a generation, i.e. it mixes the upper and lower components of the $SU(2)$ doublets. In this work, we use the approximation of a diagonal CKM matrix.

The couplings of the remaining electroweak bosons to the matter fields are not influenced the diagonalization of the mass matrices of the fermion fields and involve the complete Dirac fields, i.e. both the left- and right-handed field components. The interaction terms between the electroweak boson A and the matter fields are

$$-\frac{g_1 g_2}{\sqrt{g_1^2 + g_2^2}} \sum_f \bar{f} \left[\frac{\tau^3}{2} + Y \right] \gamma^\mu f A_\mu, \quad (74)$$

where $f = f_L + f_R$ stands for a fermion field and the sum runs over all flavors and the operators τ^3 and Y act on the fermion fields. The *Gell-Mann-Nishijima* formula [38] defines the square bracket in Eq. (74) as the electric charge operator

$$Q_{\text{EM}} = \frac{\tau^3}{2} + Y, \quad (75)$$

which is the conserved generator of the $U(1)_{\text{EM}}$ symmetry that remains after EWSB. Interpreting Eq. (74) as the fermion-photon interaction from quantum electrodynamics, it becomes clear that Q_{EM} gives the electric charge of fermion f , i.e. the strength of its interaction with the photon field in units of the combination

$$\frac{g_1 g_2}{\sqrt{g_1^2 + g_2^2}} =: e_{\text{EM}}, \quad (76)$$

which corresponds to the electromagnetic coupling constant, i.e. the absolute value of the electron charge [51].

The couplings of the Z boson and the fermions are of the form

$$-e_{\text{EM}} \sum_f \bar{f} \gamma^\mu (c_V - c_A \gamma^5) f Z_\mu. \quad (77)$$

As opposed to the charged-current interaction, this *neutral-current interaction* couples only fermions of the same flavor. This interaction involves a vector coupling and an axial coupling, with coefficients c_V and c_A which are operators that act on the fermion fields given by

$$c_V = \frac{\tau^3 - 2Q_{\text{EM}} \sin^2 \theta_W}{2 \sin \theta_W \cos \theta_W} \quad \text{and} \quad c_A = \frac{\tau^3}{2 \sin \theta_W \cos \theta_W}. \quad (78)$$

For the purposes of calculations at the level of cross sections, the quantities

$$\alpha_{\text{em}} := \frac{e_{\text{EM}}^2}{4\pi} = \frac{g_2^2 \sin^2 \theta_W}{4\pi}, \quad \alpha_s := \frac{g_s^2}{4\pi} \quad (79)$$

are defined, and are denoted as the electromagnetic and strong *coupling constants*. As we will see in Sec. 1.3.3, the coupling constants are in fact energy dependent. Nevertheless, the strong coupling constant is generally larger than the electromagnetic one. At an energy equivalent to the mass of the Z boson $M_Z = 91.1876$ GeV, for example, they are [52]

$$\alpha_{\text{em}} \approx \frac{1}{127} \approx 0.008, \quad \alpha_s \approx 0.118. \quad (80)$$

1.3.3 The Running of α_s

One consequence of the regularization and renormalization procedures that were discussed in Sec. (1.1) is the introduction of a dependence of the renormalized couplings of the theory upon the parameter μ . This dependence is given by the *renormalization group equation* (RGE)

$$\mu \frac{dg}{d\mu} = \beta(g), \quad (81)$$

which can be derived from the fact that renormalization does not affect the relations between physical quantities [42]. In Eq. (81), g stands for a generic coupling and $\beta(g)$ is the *beta function* of the relevant theory. This beta function can be determined to a certain order of perturbation theory, and then used to solve Eq. (81). This gives the explicit *running of the coupling*, *i.e.* the function $g(\mu)$ to the corresponding perturbative order. Thanks to this relation, it is possible to calculate the value of the coupling at a certain scale μ given an initial value at a different scale μ_0 .

As it turns out, the lowest order of the beta function with respect to the coupling is two. With the series expansion

$$-\beta(g) = \sum_{n=0}^{\infty} \frac{\beta_n}{(4\pi)^{1+n}} g^{2+n} \quad (82)$$

1.3 Gauge Theories and the Standard Model

from [53] and taking the lowest-order coefficient, the first-order solution of Eq. (81) is [54]

$$g(\mu) = \frac{g(\mu_0)}{1 + \beta_0 g(\mu_0) \log \frac{\mu}{\mu_0}}, \quad (83)$$

with a reference scale μ_0 .

The beta functions that describe the running of the two couplings constants of the SM, α_{em} and α_s , have a fundamental difference: while $\beta_0 < 0$ for the electromagnetic coupling, it is $\beta_0 > 0$ for the strong coupling. More specifically, for QCD it is

$$\beta_0 = \frac{11}{3}C_A - \frac{4}{3}T_F n_f \quad (84)$$

with the *number of flavors* n_f and the group-theoretical factors of $SU(N)$

$$C_A = N, \quad T_F = \frac{1}{2} \quad (85)$$

with $N = 3$ for $SU(3)$. Consequently $\beta_0 > 0$ holds for $n_f < 33/2$, in particular for the SM where $n_f = 6$.

This key difference in β_0 can be traced back to the non-commutativity of $SU(3)$, the gauge group of QCD. In terms of the running of the couplings, this means that they behave in opposite ways with respect to the renormalization scale. While α_{em} decreases for lower values of μ , α_s becomes larger. For sufficiently low μ , the strong coupling constant grows so much that perturbative methods stop being a good approximation. On the other hand, the strong coupling constant becomes ever smaller for growing values of μ , a phenomenon that is called *asymptotic freedom*. While both couplings depend upon μ , the electromagnetic coupling is normally regarded as constant in QCD calculations. This is justified because the α_{em} scale dependence is much weaker than the corresponding one for α_s .

As mentioned in Sec. 1.1, the scale μ is an arbitrary quantity of mass dimension. On the other hand, it implicitly defines the point at which the subtractions which remove the ultraviolet divergences are performed [55], hence μ is called the *renormalization scale* and denoted by μ_r , which we will do from now on.

Quantities calculated at a given perturbative order require a choice for its value, since the matrix elements display an explicit dependence upon it³. Often, an adequate choice is a characteristic energy scale Q^2 of the process under consideration. This is adequate in the sense that it prevents logarithms that appear in higher-order corrections from becoming too large and spoiling the perturbative expansion, see Sec. 10.5 in Ref. [43], and μ_r is generally chosen this way. In other words, $\alpha_s(\mu_r^2 \simeq Q^2)$ is indicative of the effective strength of the strong interaction in a process with

³This dependence becomes weaker for higher orders, and it is used to estimate the size of the uncertainty due to the truncation of the perturbative series.

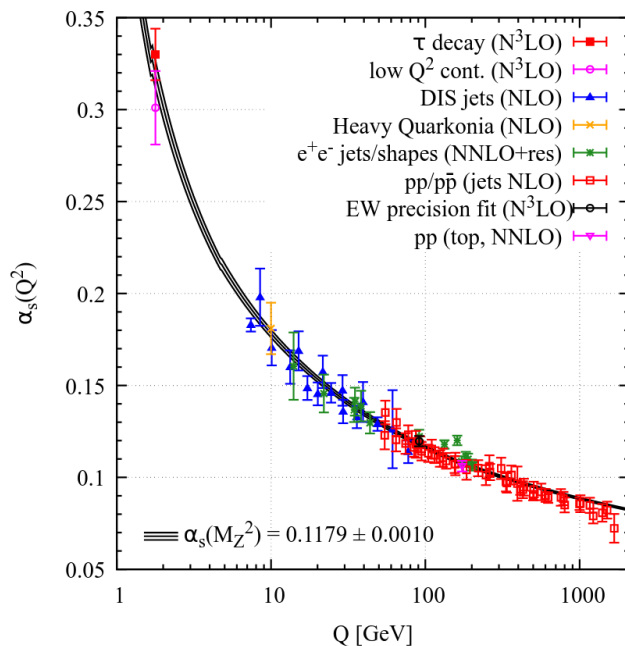


Figure 2: Comparison of indirect measurements of the strong coupling constant against its theoretical running. The data points show values of the strong coupling constant α_s , extracted from different measurements at different energy scales Q . The solid line shows the running of the coupling computed from the starting energy value M_Z^2 . Figure taken from Ref. [52].

momentum transfer Q [52]. The asymptotic freedom of QCD ultimately allows for the perturbative treatment of the theory of strong interactions in the high-energy regime.

Values for α_s can be extracted from measurements of observables at different energy scales by using theoretical expressions at a certain order for those observables. In Fig. 2, such values are displayed as points, which are in agreement with the running of the coupling calculated from the beta function using α_s extracted at $Q^2 = M_Z^2$ as an input value.

1.3.4 Lagrangian and Feynman Rules

All in all, the Lagrangian of the SM is given by

$$\mathcal{L}_{\text{SM}} = \mathcal{L}_{\text{matter}} + \mathcal{L}_{\text{gauge}} + \mathcal{L}_{\phi} + \mathcal{L}_{\text{Yukawa}} + \mathcal{L}_{\text{gauge-fixing}}, \quad (86)$$

where $\mathcal{L}_{\text{gauge-fixing}}$ compiles the gauge-fixing terms that are necessary for the quantization of the gauge fields, including the ghost fields that are introduced in the path-integral quantization of QCD. We don't mention these terms explicitly. The interactions contained in \mathcal{L}_{SM} , most of which have been discussed in this section, give rise to Feynman rules for matrix elements. In Figs. 3 and 4 we cite some of

1.3 Gauge Theories and the Standard Model

them, following Ref. [42], separately for particles with and without participation in the strong interaction.

Equations (87) to (91) in Fig. 3 show some Feynman rules of QCD. The rules in Eqs. (87) and (88) are for internal propagators and those in Eqs. (89) to (91) are for interaction vertices. The vertices in Eqs. (90) and (91) correspond to the self-interactions of the gluons. Here, q and g denote quark and gluon fields, respectively. Greek characters denote Lorentz indices, while latin characters denote fundamental (i, j) or adjoint (a, b, c, d, e) color indices. The f^{abc} are the structure constants of the $SU(3)$ color group, see Eq. (49). The Dirac indices carried by gamma matrices are suppressed. Momentum flow is indicated by a separate arrow and fermion flow is indicated by embedded arrowheads. Rule (88) includes the gauge parameter ξ . Common gauge choices include Feynman gauge ($\xi = 1$) and Lorenz gauge ($\xi = 0$) [56].

Figure 4 displays some Feynman for the EW sector. There, f denotes a fermion field and V stands for A, Z or W . In rule (93), $M_A = 0$ for the photon $V = A$. As in Eq. (88), rule (93) includes the gauge parameters ξ_V , which can in principle be different for each EW vector boson V . Rule (95) has been simplified by assuming a diagonal CKM matrix. The vector and axial couplings c_V and c_A of rule (96) are defined in Eq. (78). The triple and quartic gauge couplings of rules (97) and (98) depend upon the kind of vector bosons that are involved. Their values are given in Table 1.

Table 1: Values of the triple and quartic EW gauge couplings for specific combinations of vector bosons. Here, $\sin \theta_W$ is the Weinberg angle from Eq. (65).

$V_1 V_2 V_3$	AW^+W^-	ZW^+W^-		
c_{TGC}	1	$-\cos \theta_W / \sin \theta_W$		
$V_1 V_2 V_3 V_4$	W^+W^-AA	W^+W^-ZZ	W^+W^-AZ	$W^+W^+W^-W^-$
c_{QGC}	-1	$-\sin^2 \theta_W / \cos^2 \theta_W$	$\cos \theta_W / \sin \theta_W$	$1 / \sin^2 \theta_W$

In Fig. 5, we show two further Feynman rules that are relevant for this work. These describe the propagator of the Higgs boson and the interaction vertex of one Higgs boson and two EW bosons, see also Eq.(66).

In calculations, the denominator of massive propagators is often modified to include the *decay width* Γ of the associated particle as

$$p^2 - M^2 \quad \rightarrow \quad p^2 - M^2 + iM\Gamma. \quad (101)$$

The particle's width Γ , which is a quantity that can be extracted from measurements, regulates the pole in the propagator. The replaced denominator on the left side of Eq. (101) leads to cross sections that behave like a Breit-Wigner distribution near the resonance, which correctly reproduces experimental observations. On the other

$$j \xrightarrow[\vec{p}]{q} i = i\delta_{ij} \frac{\not{p} + m}{p^2 - m^2 + i\varepsilon} \quad (87)$$

$$a, \mu \xrightarrow[\vec{p}]{g} b, \nu = \frac{i\delta_{ab}}{p^2 + i\varepsilon} \left[- \left(g_{\mu\nu} - \frac{p_\mu p_\nu}{p^2} \right) - \xi \frac{p_\mu p_\nu}{p^2} \right] \quad (88)$$

$$a, \mu \xrightarrow{g} \begin{array}{l} i \\ q \\ \bar{q} \\ j \end{array} = ig_s T_{ij}^a \gamma^\mu \quad (89)$$

$$a, \mu \xrightarrow[\vec{k}_1]{g_1} \begin{array}{l} k_2 \\ g_2, b, \nu \\ k_3 \\ g_3, c, \rho \end{array} = g_s f^{abc} \left[g_{\mu\nu}(k_1 - k_2)_\rho + g_{\nu\rho}(k_2 - k_3)_\mu + g_{\rho\mu}(k_3 - k_1)_\nu \right] \quad (90)$$

$$\begin{array}{l} g_1, a, \mu \\ g_2, b, \nu \end{array} \xrightarrow{\quad} \begin{array}{l} g_3, c, \rho \\ g_4, d, \sigma \end{array} = -ig_s^2 \left[f^{abe} f^{cde} (g_{\mu\rho} g_{\nu\sigma} - g_{\mu\sigma} g_{\nu\rho}) + f^{ace} f^{dbe} (g_{\mu\sigma} g_{\rho\nu} - g_{\mu\nu} g_{\rho\sigma}) + f^{ade} f^{bce} (g_{\mu\nu} g_{\sigma\rho} - g_{\mu\rho} g_{\sigma\nu}) \right] \quad (91)$$

Figure 3: Some Feynman rules of QCD. The rules in Eqs. (87) and (88) are for internal propagators and those in Eqs. (89) to (91) are for interaction vertices. See text for details.

1.3 Gauge Theories and the Standard Model

$$\text{---} \xrightarrow[p]{f} \text{---} = i \frac{\not{p} + m}{p^2 - m^2 + i\varepsilon} \quad (92)$$

$$\mu \text{---} \xrightarrow[p]{V} \nu = \frac{i}{p^2 - M_V^2 + i\varepsilon} \left[- \left(g_{\mu\nu} - \frac{p_\mu p_\nu}{p^2 - \xi_V M_V^2} \right) - \xi_V \frac{p_\mu p_\nu}{p^2 - \xi_V M_V^2} \right] \quad (93)$$

$$\mu \text{---} \xrightarrow{A} \begin{array}{l} f \\ \bar{f} \end{array} = -ie_{\text{EM}} Q_{\text{EM}}^f \gamma^\mu \quad (94)$$

$$\mu \text{---} \xrightarrow{W} \begin{array}{l} f \\ \bar{f} \end{array} = \frac{ie_{\text{EM}}}{\sqrt{2} \sin \theta_W} \gamma^\mu P_L \quad (95)$$

$$\mu \text{---} \xrightarrow{Z} \begin{array}{l} f \\ \bar{f} \end{array} = ie_{\text{EM}} \gamma^\mu (c_V^f - c_A^f \gamma^5) \quad (96)$$

$$\mu \text{---} \xrightarrow[V_1]{k_1} \begin{array}{l} V_2, \nu \\ V_3, \rho \end{array} = ie_{\text{EM}} c_{\text{TGC}} (g_{\mu\nu} (k_1 - k_2)_\rho + g_{\nu\rho} (k_2 - k_3)_\mu + g_{\rho\mu} (k_3 - k_1)_\nu) \quad (97)$$

$$\begin{array}{l} V_1, \mu \\ V_2, \nu \end{array} \text{---} \begin{array}{l} V_3, \rho \\ V_4, \sigma \end{array} = ie_{\text{EM}}^2 c_{\text{QGC}} (2 g_{\mu\nu} g_{\sigma\rho} - g_{\nu\rho} g_{\mu\sigma} - g_{\rho\mu} g_{\nu\sigma}) \quad (98)$$

Figure 4: Feynman rules for fields without color charge. Equations (92) and (93) give the rules for internal leptons and EW vector bosons, respectively. Equations (94) to (97) give rules for couplings. See text for details.

$$\begin{array}{c} h \\ \text{---} \\ \xrightarrow{p} \end{array} = \frac{i}{p^2 - m_h^2 + i\varepsilon} \quad (99)$$

$$\begin{array}{c} V, \mu \\ \text{---} \\ h \text{---} \\ \text{---} \\ V, \nu \end{array} = i e_{\text{EM}} g_{\mu\nu} M_V \quad (100)$$

Figure 5: Two Feynman rules including the Higgs field. Equation (92) gives the rule for the propagator of a Higgs boson and Eq. (93) gives the rules for the couplings of two equal EW vector bosons V to the Higgs boson.

hand, the replacement of Eq. (101) arises from the theory if one considers the exact (all-orders) propagator, see for instance Ref. [38].

We finalize this section with some remarks about the practical use of the Feynman rules. To arrive at expressions for matrix elements of scattering processes from Feynman diagrams, wave functions of the external particles and the Feynman rules for internal propagators and vertices are multiplied together, for each diagram. Thereby, the Lorentz indices in the expressions are contracted and scalar quantities result, which possibly still depend upon polarization (or spin) and color degrees of freedom of the attached wave functions.

In mathematical expressions of Feynman diagrams that include strongly interacting particles, the color-dependent part, which arises from the δ_{ij} , T_{ij}^a and f^{abc} factors in the Feynman rules above, can be separated from the spin- and momentum-dependent part. More generally, a matrix element at a certain order, to which potentially many Feynman diagrams contribute, can be linearly decomposed as [57]

$$\mathcal{M} = \sum_i \mathcal{C}_i \mathcal{A}_i, \quad (102)$$

where the *color factors* \mathcal{C}_i summarize the color-algebra dependence and the \mathcal{A} are called *partial* or *color-ordered (sub)amplitudes* and carry the polarization and kinematic dependence.

As mentioned in Sec. 1.1.1, degrees of freedom that are not observed are averaged over when calculating observables from matrix elements. While this is always the case for color indices, spin indices may or may not be averaged over to obtain unpolarized or polarized observables, respectively. The observables considered in this work are unpolarized.

1.4 Hadron Collisions and Factorization

Up to this point, our discussion of the theoretical calculation of collision processes has involved only elementary particles. On the other hand, investigating processes with strongly interacting particles in the initial state requires the collision of *hadrons*. This is due to the fact that no free color-charged particles can be detected, a property known as *color confinement*. While it is associated with the low-energy regime, in which perturbative QCD breaks down due to a large strong coupling constant, it is not entirely understood how the confinement property arises from QCD [42].

Hadrons are color-neutral bound states of quarks, which can be observed. Historically, the quark hypothesis was put forward in 1964 to classify the hadron spectrum in the first place [58, 59], which seemed too rich to be fundamental. Later, it was found that the observations from experiments of *Deep Inelastic Scattering* (DIS), in which a hadron is probed with a very energetic lepton, were highly compatible with the thesis of free, point-like scattering centers inside of hadrons [60, 61, 62]. Specifically, it was shown that the so-called *structure functions* of hadrons follow a specific scaling property, known as *Björken scaling*, to a very good approximation. These scattering centers have the properties of quarks and were called *partons* by Richard Feynman [39], who consequently formulated the *parton model* of hadron scattering [63].

In the naive form of this model, hadrons in *hard* (i.e. highly energetic) scattering processes act like an ensemble of free partons. The hadron momentum is distributed over the momenta of the partons, which are themselves mostly collinear to the hadron's momentum. Then, the cross section of a process with hadrons h_1 and h_2 in the initial state and an n -parton final state is given by

$$\sigma_{h_1 h_2 \rightarrow n} = \sum_{a,b} \int_0^1 dx_a dx_b f_a^{h_1}(x_a) f_b^{h_2}(x_b) \hat{\sigma}_{a,b \rightarrow n}(x_a, x_b, \mu_r), \quad (103)$$

where a and b are partons in h_1 and h_2 , respectively, and $\hat{\sigma}_{ab \rightarrow n}$ is the *partonic cross section*, that can be computed by perturbative methods to a certain order and is given by,

$$\hat{\sigma}_{ab \rightarrow n} = \frac{1}{2\hat{s}} \int d\Phi_n |\mathcal{M}_{a,b \rightarrow n}(\Phi_n)|^2, \quad (104)$$

according to Eq. (14) for massless incoming particles. Here $\hat{s} = x_a x_b s$ is the partonic center of mass energy and s is its counterpart for the two-hadron system.

The $f_j^{h_i}(x_j)$ are *parton distribution functions* (PDFs) and describe the probability that the j -th parton of hadron h_i carries the momentum $x_j P_{h_i}$, which is a fraction of the total hadron's momentum P_{h_i} for $x_j \in [0, 1]$. The PDFs act as the weights in the sum over partonic cross sections, and the hadronic cross section is obtained upon integrating over all possible momentum fractions. Thus, Eq. (103) represents the incoherent sum of interactions between the partons, i.e. a sum at cross-section

level. This model neglects interferences and interactions between the final state particles. Also, it assumes that parton distribution functions are universal, so that the PDF of a hadron can be used in different processes with different partonic cross sections, as long as that hadron is part of the initial state.

While the naive parton model is independent of QCD, the two can be connected. Treating partons as free particles in high energy collisions is consistent with asymptotic freedom. Furthermore, together with perturbative QCD, the parton model can explain the deviation to Björken scaling that is observed in experiments [56]. Also, the gluons of QCD can be included as constituents of hadrons, i.e. as partons, to solve the issue that the fraction of a hadron's momentum carried by quarks and antiquarks is significantly less than one [64].

On the other hand, Eq. (103) assumes that the hadronic process can be separated into a hard partonic process that is calculated with perturbative methods and a non-perturbative description of the hadrons, which is realized by the universal PDFs. This property is called *factorization*, and it is not trivial to recover from QCD. It has in fact only been shown for certain processes, DIS and the *Drell-Yan* process [53], but not for general processes involving two hadrons in the initial state. Nevertheless, the validity of factorization for such processes is often assumed. When factorization holds, it does so up to terms that are suppressed by powers of the characteristic hard scale of the process. Schematically, the factorization property for a process involving hadrons can be written as [56]

$$\sigma_{\text{had}} = f \otimes H + \mathcal{O}\left(\frac{\Lambda_{\text{QCD}}}{Q}\right), \quad (105)$$

where f are the PDFs, H is the perturbative hard calculation and \otimes denotes a convolution. In Eq. (105), Λ_{QCD} is the scale at which perturbative QCD breaks down and Q is a high-energy scale of the process described by σ_{had} . Since the PDFs describe an energy regime that cannot be treated by perturbative methods, they are not calculated but extracted from experimental data.

The separation of scales stated by factorization offers a solution to the problem of uncanceled collinear divergences that was illustrated in Sec. 1.2.3. These divergences arise at NLO from collinear emissions off massless particles in the initial state, which in the real corrections are part of what would correspond to $\hat{\sigma}$ in Eq. (103). As mentioned in Sec. (1.2.3), these IR divergences can be dimensionally regularized as poles of a regulator ϵ_{IR} , whereby a mass scale μ is introduced. Then, the poles in ϵ_{IR} themselves factorize from the underlying LO process. Such collinear emissions are to be associated to the initial states themselves and not the hard part of the process [46]. Therefore, it is natural to shift them from $\hat{\sigma}$ to a redefinition of the PDFs in Eq. (103), so that the remaining hard part is free of all divergences. Schematically, this shift

1.4 Hadron Collisions

reads

$$\begin{aligned}
\sigma_{h_1 h_2} &= \sum_{a,b} \int_0^1 dx_a dx_b f_a^{h_1}(x_a) f_b^{h_2}(x_b) \hat{\sigma}_{a,b}(x_a, x_b, \mu_r) \\
&= \sum_{a,b} \int_0^1 dx_a dx_b f_a^{h_1}(x_a) f_b^{h_2}(x_b) C_a(\mu_f) C_b(\mu_f) \hat{\sigma}_{a,b}^{\text{finite}}(x_a, x_b; \mu_r, \mu_f) \\
&= \sum_{a,b} \int_0^1 dx_a dx_b \tilde{f}_a^{h_1}(x_a; \mu_f) \tilde{f}_b^{h_2}(x_b; \mu_f) \hat{\sigma}_{a,b}^{\text{finite}}(x_a, x_b; \mu_r, \mu_f),
\end{aligned} \tag{106}$$

where the $C_i(\mu_r)$ contain the ϵ_{IR} poles associated to collinear emission from the initial-state parton i and μ_f is the *factorization scale*, the mass scale introduced during the dimensional regularization of the IR divergences.

More specifically, consider the calculation of a partonic cross section $\hat{\sigma}_{a,b}$ at NLO. After the KLN cancellation is carried out, initial-state collinear divergences remain. Assume that one of them originates from parton a with momentum p_a emitting a particle c , thereby retaining only the fraction z of its momentum and possibly becoming another parton d , which then goes on to enter the hard scattering with momentum zp_a . Such a divergence takes the following form

$$-\frac{1}{\epsilon_{\text{IR}}} \frac{\alpha_s}{2\pi} P_{da}(z) \hat{\sigma}_{d,b}^{\text{LO}}(zp_a), \tag{107}$$

where $\hat{\sigma}_{\text{LO}}$ corresponds to the LO hard process initiated by partons d and b and $P_{da}(z)$ is a *Dokshitzer–Gribov–Lipatov–Altarelli–Parisi (DGLAP) splitting function* associated to the splitting $a \rightarrow cd$. Similar divergences associated with collinear emissions by a can be collected as

$$\hat{\sigma}_{a,b}|_{\text{ICdiv},a} = -\frac{1}{\epsilon_{\text{IR}}} \sum_d \int_0^1 dz \frac{\alpha_s}{2\pi} P_{da}(z) \hat{\sigma}_{d,b}^{\text{LO}}(zp_a), \tag{108}$$

where we have summed over all possible splittings and integrated over the momentum fraction z . The NLO partonic cross section $\hat{\sigma}_{a,b}$ then contains

$$\hat{\sigma}_{a,b} = \hat{\sigma}_{a,b}^{\text{LO}} + \hat{\sigma}_{a,b}^{\text{real}}|_{\text{ICdiv},a} + \text{finite terms}, \tag{109}$$

where the finite terms are of NLO and the remainders of the KLN cancellation.

We now go back to the first line of Eq. (106) and consider only the parts that concern parton a , for simplicity. We insert Eq. (109), then rename the summation

indices in the second term and then shift the integration variable to obtain

$$\begin{aligned}
 & \sum_a \int_0^1 dx_a f_a^{h_1}(x_a) \hat{\sigma}_{a,b}(x_a) \\
 &= \sum_a \int_0^1 dx_a \left[f_a^{h_1}(x_a) \hat{\sigma}_{a,b}^{\text{LO}}(x_a) - \frac{1}{\epsilon_{\text{IR}}} \sum_d \int_0^1 dz f_a^{h_1}(x_a) \frac{\alpha_s(\mu_f)}{2\pi} P_{da}(z) \hat{\sigma}_{d,b}^{\text{LO}}(zx_a) \right] \\
 &= \sum_a \int_0^1 dx_a \left[f_a^{h_1}(x_a) \hat{\sigma}_{a,b}^{\text{LO}}(x_a) - \frac{1}{\epsilon_{\text{IR}}} \sum_d \int_0^1 dz f_d^{h_1}(x_a) \frac{\alpha_s(\mu_f)}{2\pi} P_{ad}(z) \hat{\sigma}_{a,b}^{\text{LO}}(zx_a) \right] \\
 &= \sum_a \int_0^1 dx_a \left[f_a^{h_1}(x_a) \hat{\sigma}_{a,b}^{\text{LO}}(x_a) - \frac{1}{\epsilon_{\text{IR}}} \sum_d \int_{x_a}^1 \frac{dz}{z} f_d^{h_1}(z) \frac{\alpha_s(\mu_f)}{2\pi} P_{ad}\left(\frac{x_a}{z}\right) \hat{\sigma}_{a,b}^{\text{LO}}(x_a) \right] \\
 &= \sum_a \int_0^1 dx_a \left[f_a^{h_1}(x_a) - \frac{1}{\epsilon_{\text{IR}}} \sum_d \int_{x_a}^1 \frac{dz}{z} f_d^{h_1}(z) \frac{\alpha_s(\mu_f)}{2\pi} P_{ad}\left(\frac{x_a}{z}\right) \right] \hat{\sigma}_{a,b}^{\text{LO}}(x_a),
 \end{aligned} \tag{110}$$

where we have suppressed the finite terms. The second-to-last equality in Eq. (110) can be seen by inserting an integral $\int_0^1 dy \delta(y - zx_a)$ to the second term, performing the integral over z and then renaming $x_a \rightarrow z$ and $y \rightarrow x_a$. These steps can be equally followed for parton b in Eq. (106).

The last line of Eq. (110) suggests how to redefine the PDFs, namely

$$\tilde{f}_a^{h_1}(x) = \left[f_a^{h_1}(x) - \frac{1}{\epsilon_{\text{IR}}} \sum_d \int_x^1 \frac{dz}{z} f_d^{h_1}(z) \frac{\alpha_s}{2\pi} P_{ad}\left(\frac{x}{z}\right) \right]. \tag{111}$$

Using the PDFs extracted from data as $\tilde{f}(x)$, only finite terms remain in the total hadronic cross section. Equation (111) shows that the redefinition corresponds to an NLO correction to $f(x)$. Thus, the product of the NLO term in $\tilde{f}(x)$ and the NLO terms in the finite, partonic cross section in Eq. (106) would be of orders higher than NLO, so they are not taken into account in an NLO calculation.

Yet another way to understand the redefinition of the PDFs is that they have been renormalized. As in UV renormalization, a divergence is subtracted from $f(x)$. Again, the subtraction can include finite terms, and the $\overline{\text{MS}}$ scheme is used for PDFs to subtract the terms $-\gamma_E + \log 4\pi$ that arise from dimensional regularization. The equivalent to the RGE for PDFs, which now follows from the independence of observables from the factorization scale, are the DGLAP equations. For quarks and gluons, they read [56]

$$\mu_f \frac{d}{d\mu_f} \begin{pmatrix} f_i(x, \mu_f) \\ f_g(x, \mu_f) \end{pmatrix} = \frac{\alpha_s}{\pi} \sum_j \int_x^1 \frac{dz}{z} \begin{pmatrix} P_{q_i q_j}(x/z) & P_{q_i g}(x/z) \\ P_{g q_j}(x/z) & P_{g g}(x/z) \end{pmatrix} \begin{pmatrix} f_j(z, \mu_f) \\ f_g(z, \mu_f) \end{pmatrix}, \tag{112}$$

at leading order, where the sum i and j stand for quark flavors. The splitting

1.5 The Structure of a Collision Event

functions P_{ab} are

$$P_{qq}(z) = C_F \left[\frac{1+z^2}{[1-z]_+} + \frac{3}{2}\delta(1-z) \right] \quad (113)$$

$$P_{qg}(z) = T_F [z^2(1-z^2)] \quad (114)$$

$$P_{gq}(z) = C_F \left[\frac{1+(1-z)^2}{z} \right] \quad (115)$$

$$P_{gg}(z) = 2C_A \left[\frac{z}{[1-z]_+} + \frac{1-z}{z} + z(1-z) \right] + \frac{\beta_0}{2}\delta(1-z), \quad (116)$$

with

$$C_F = \frac{N^2 - 1}{N}, \quad C_A = N_C, \quad T_F = \frac{1}{2} \quad \text{and} \quad \beta_0 = \frac{11}{3}C_A - \frac{4}{3}T_F n_f, \quad (117)$$

for $N_C = 3$, cf. Sec. 1.3.3, and with the *plus distributions* $[\dots]_+$ that regulate the divergences at $z = 1$. In general, they act as

$$\int_0^1 dz f(z)[g(z)]_+ = \int_0^1 dz (f(z) - f(1))g(z) \quad (118)$$

on a test function $f(z)$ and a function $g(z)$ that diverges at the upper integration limit.

The splitting functions P_{ab} from Eqs. (113)–(116) depend only on the type of splitting they describe. This means that the PDFs remain universal after the redefinition of Eq. (106). In an NLO calculation, the initial-state collinear emissions that remain after the KLN cancellation are subtracted in the form of *collinear counterterms* from an NLO partonic cross section. In Sec. 2.1, we describe this subtraction procedure in more detail.

1.5 The Structure of a Collision Event

In this section, we discuss how hadron-initiated processes from collision experiments are modeled. From the very first interaction between incoming hadrons to the very last particle decay that occurs before particles can be detected, the process can be thought of as a sequence of steps, each of which develops at a different energy scale. A collision can be broken down into the following five components [53]:

1. Hard process (parton-parton collision)
2. Initial and final state radiation
3. Underlying event
4. Hadronization
5. Hadron decays

These are ordered by momentum transfer from *hardest* to *softest*. The broad energy spectrum that these components encompass demands the use of different models and techniques for their simulation.

During the hard process, the largest momentum transfer occurs between partons. This step can be described perturbatively by calculating a hadronic cross section from matrix elements to a given order and using the factorization discussed in Sec. 1.4. This is called a *fixed-order* (FO) calculation. In practice, this means the following: After being brought to a suitable form (see Sec. 2.1), Eq. (106) is numerically integrated using *Monte Carlo methods*, and a set of external momenta is sampled, distributed according to the cross section.

The second step in the model is the emission of secondary particles by the particles going in and out of the hard process. These are highly energetic and can radiate photons and gluons. Radiated gluons can themselves radiate more gluons or produce quark-antiquark pairs. This radiation is predominantly collinear, and after several branchings it resembles a shower. The tools used for their simulation are denoted accordingly as parton showers (PS) or shower Monte Carlos (SMC). The description of radiation by a PS is probabilistic and inherently approximative, but essential for a realistic description of the collision. Such simulations are described in some more detail in Sec. 2.2.

Besides the main hard process, secondary interactions between the remaining incoming hadrons, i.e. the components that were ignored when choosing the specific interacting partons of the hard process, also interact and influence the detected final state. These other processes are called the underlying event, and cannot be described perturbatively. After radiating away most of their kinetic energy, the momenta of the outgoing particles become smaller, and the coupling constant grows. At some point, the hadronization of quarks and gluons into observable, colorless bound states takes place. Because of the energy scale, this process again can not be described using perturbation theory. Its simulation is phenomenological, and relies on models like the Lund string model [65]. Finally, the decay of possible excited hadronic states can be modeled. The components of a hadron collision are shown schematically in Fig. 6.

For this work, we have performed a simulation of the hard process using matrix elements at NLO in QCD and interfaced the result to the PS of the PYTHIA 8.240 program [67], which takes care of the initial and final state radiation, hadronization and decays. To control the non-perturbative physics that goes into the simulation of the underlying event and hadronization PYTHIA employs sets of parameters, called *tunes*, that have been collectively tuned to describe experimental data. We employ the *Monash 2013* tune [68], which was created using LHC data and has been the default of PYTHIA from version 8.200 on. In Sec. 2, we discuss the techniques of NLO calculations, as well as PS programs and the matching of the two.

1.6 Jets

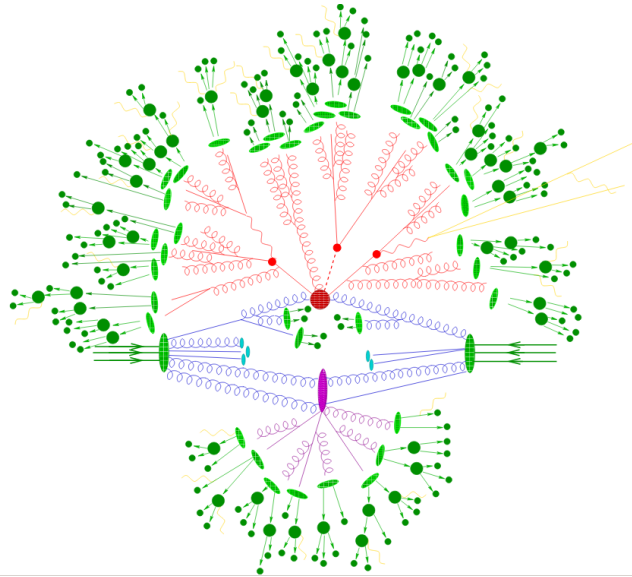


Figure 6: Graphic representation of a hadron collision event, from Ref. [66]. The hard process is represented by the red circle in the middle, and the red lines denote the final-state of the signal process and its radiation. The blue lines stand for the the initial state radiation, some of which lead to the beam remnants in light blue. The underlying event is shown in purple, while the light and dark green lines and shapes correspond to the hadronization products and their decays respectively.

1.6 Jets

For collision processes that involve color-charged particles in the final state, the concept of *jets* plays a crucial role. A physical detector in collision experiments cannot distinguish very soft or collinear emissions by final-state particles. If a particle emits others below a certain angle and energy threshold, mother and daughter particles are perceived as part of the same particle. More generally, any final-state particles that cannot be well separated are detected as a bundle. These particle bundles are called jets, and they are part the final states of hadron collisions that are actually detected, as opposed to single quarks and gluons. From a theoretical point of view, the concept of jets is important for infrared safety. As we have seen in Sec. 1.2.3, the virtual correction to the cross section of a $2 \rightarrow n$ process must be combined with a tree-level $2 \rightarrow n + 1$ cross section to yield a finite result. Thus, an IR-safe observable must include both $2 \rightarrow n$ and $2 \rightarrow n + 1$ contributions (below a certain threshold), and be insensitive to soft and collinear emissions. Like a physical detector, an IR-safe observable can measure jets but not partons.

In simulations of collision processes, jets are constructed event by event using the momenta of the event's final-state particles. If a PS program is employed, the jets are constructed after the initial- and final-state radiation has been modeled by it. The output of the PS program is a set of the momenta of all final state particles that have been produced in the shower. This list can be considerably larger than the

list of final-state momenta directly after the hard process. From this list, bundles of particles can be found that correspond to the jets that are expected to be observable.

Several *jet algorithms* exist for the construction of the jets. In general, they should be insensitive to soft or collinear radiation and hadronization processes, i.e. they should return similar jets when started directly after the hard process, after the PS process or after hadronization. Due to the soft/collinear nature of the radiation that takes place after the hard process, this is compatible with the picture of jets as particle bundles.

In this work, we employ the commonly used *anti- k_T clustering algorithm* [69]. In it, every final-state particle i is called an *entity*, and its distances d_{iB} from the beam axis and d_{ij} from every other particle j are defined as

$$d_{iB} = \frac{1}{p_{T,i}^2} \quad (119)$$

and

$$d_{ij} = \min \left(\frac{1}{p_{T,i}^2}, \frac{1}{p_{T,j}^2} \right) \frac{\Delta R_{ij}^2}{R^2}, \quad (120)$$

where $p_{T,i}^2 = p_{1,i}^2 + p_{2,i}^2$ is the transverse momentum of the i -th particle and R is the *radius parameter*. ΔR_{ij}^2 is the distance between the particle's momenta in the $y - \phi$ plane

$$\Delta R_{ij}^2 = (y_i - y_j)^2 + (\phi_i - \phi_j)^2, \quad (121)$$

with the rapidity

$$y_i = \ln \frac{p_{0,i} + p_{3,i}}{p_{0,i} - p_{3,i}}, \quad (122)$$

that measures the forwardness of the i -th particle and the azimuthal angle ϕ_i between its momentum and the beam axis. Then, the smallest of all d_{iB}, d_{ij} for a given i is identified. If it is a d_{ij} , i and j are combined to one entity. If it is d_{iB} , i is promoted to a jet and removed it from the list of entities. The distances are recalculated and the procedure repeated until no entities are left [69].

The role radius parameter R can be understood as a minimal separation between entities, below which they are clustered together as a jet. Consider the scenario of two entities with transverse momenta $p_{T,1}, p_{T,2}$ and $p_{T,1} > p_{T,2}$. Then the relevant distances according to Eqs. (119 and (120) are

$$d_{1B} = \frac{1}{p_{T,1}^2}, \quad d_{2B} = \frac{1}{p_{T,2}^2}, \quad d_{12} = \frac{1}{p_{T,1}^2} \frac{\Delta R_{12}^2}{R^2}. \quad (123)$$

Following the algorithm described above, one can see that if $\Delta R_{12} < R$ then $\min(d_{1B}, d_{2B}, d_{12}) = d_{12}$ and the entities are clustered. If $\Delta R_{12} > R$, then $\min(d_{1B}, d_{2B}, d_{12}) = d_{1B}$ and entity 1 is declared a jet and taken out of the list, so the entities are not clustered.

2 Nex-to-leading Order Calculations and Parton Showers

In this chapter, we review the general structure of a numerical calculation to the next-to-leading order in QCD matched to a PS program. For the hard part of the process, calculated at fixed order, we discuss *IR subtraction*, i.e. the management of IR divergences that is necessary to realize the KLN cancellation in practice. Then, we present the idea behind parton showers and their numerical realization. Finally, we discuss the problem of matching an NLO calculation to a PS simulation and conclude the section by presenting one way to deal with it, the POWHEG method [33, 34].

2.1 Infrared Subtraction

Closely following [34], we want to outline the structure of a QCD NLO calculation of a hadronic cross section and how the arising divergences are handled in practice in the methods employed in this work. As discussed in Sec. 1.2.1 and 1.2.3, the NLO calculation of a partonic cross section must include a Born, a virtual and a real contribution. According to Eq. (14), the NLO cross section is then given by

$$\hat{\sigma}^{\text{NLO}} = \frac{1}{2\hat{s}} \left[\int d\Phi_n [|\mathcal{M}_{\text{Born}}(\Phi_n)|^2 + 2\Re\{\mathcal{M}_{\text{Born}}(\Phi_n) \cdot \mathcal{M}_{\text{virt}}^*(\Phi_n)\}] \right. \quad (124)$$

$$\left. + \int d\Phi_{n+1} |\mathcal{M}_{\text{real}}(\Phi_{n+1})|^2 \right] \quad (125)$$

where $\Re\{z\}$ is the real part of z . To obtain the hadronic cross section, Eq. (124) can be plugged into Eq. (106), which includes a sum over possible partons, an integral over each incoming parton's momentum fraction and the PDFs. To cancel initial-state collinear divergences, collinear counterterms must be introduced and redefined PDFs must be used. In the notation of [34], the hadronic cross section then reads

$$\begin{aligned} \sigma^{\text{NLO}} = & \int d\Phi_n \mathcal{L} \left[\mathcal{B}(\Phi_n) + \mathcal{V}_b(\Phi_n) \right] + \int d\Phi_{n+1} \mathcal{L} \mathcal{R}(\Phi_{n+1}) \\ & + \int d\Phi_{n,\oplus} \mathcal{L} \mathcal{G}_{\oplus,b}(\Phi_{n,\oplus}) + \int d\Phi_{n,\ominus} \mathcal{L} \mathcal{G}_{\ominus,b}(\Phi_{n,\ominus}), \end{aligned} \quad (126)$$

where we have defined the Born, virtual and real contributions \mathcal{B} , \mathcal{V}_b and \mathcal{R} . We will assume that all contributions in Eq. (126) have been regularized, and that the virtual term \mathcal{V}_b has been renormalized and is UV-finite and only contains IR divergences, which is hinted at by the “bare” subindex b. \mathcal{B} , \mathcal{V}_b and \mathcal{R} include the partonic flux factor as well as the sum over the initial-state partons, and are functions of the momenta of the outgoing momenta k_i , $i = 1, \dots, n$ and of the momentum fractions x_\oplus and x_\ominus of the incoming partons, whose three-momenta are

parallel and opposite. Additionally, \mathcal{R} depends upon the momentum k_{n+1} of the real emission. The corresponding full phase-space elements are

$$d\Phi_n = dx_\oplus dx_\ominus d\Phi_n(k_\oplus + k_\ominus; k_1, \dots, k_n), \quad (127)$$

$$d\bar{\Phi}_{n+1} = dx_\oplus dx_\ominus d\Phi_{n+1}(k_\oplus + k_\ominus; k_1, \dots, k_{n+1}), \quad (128)$$

where $k_\oplus = x_\oplus K_\oplus$ and $k_\ominus = x_\ominus K_\ominus$ denote the incoming parton momenta, derived from the hadron momenta K_\oplus and K_\ominus . The PDFs, one for each incoming parton, have been summarized in the *luminosity*

$$\mathcal{L} = \mathcal{L}(x_\oplus, x_\ominus) = f_\oplus(x_\oplus) f_\ominus(x_\ominus), \quad (129)$$

where the scale and parton-flavor dependence of the PDFs has been suppressed. In Eq. (126), $\mathcal{G}_{\oplus,b}$ and $\mathcal{G}_{\ominus,b}$ denote the the initial-state collinear counterterms, which contain ϵ poles. They are functions of $\Phi_{n,\oplus}$ and $\Phi_{n,\ominus}$, which correspond to an $(n+1)$ phase space in the scenario of initial-state collinear emission, i.e. with the restriction that one final-state parton is collinear to one initial-state parton, so that only the energy of the radiated particle is a free variable. For a given infrared safe observable O , a function of the final-state momenta, its expectation value can be written as:

$$\begin{aligned} \langle O \rangle = & \int d\Phi_n \mathcal{L} O_n(\Phi_n) \left[\mathcal{B}(\Phi_n) + \mathcal{V}_b(\Phi_n) \right] + \int d\Phi_{n+1} \mathcal{L} O_{n+1}(\Phi_{n+1}) \mathcal{R}(\Phi_{n+1}) \\ & + \int d\Phi_{n,\oplus} \mathcal{L} O_n(\bar{\Phi}_n) \mathcal{G}_{\oplus,b}(\Phi_{n,\oplus}) + \int d\Phi_{n,\ominus} \mathcal{L} O_n(\bar{\Phi}_n) \mathcal{G}_{\ominus,b}(\Phi_{n,\ominus}), \end{aligned} \quad (130)$$

where $\bar{\Phi}_n$ is the *underlying Born configuration* that corresponds to $\Phi_{n,\oplus}$ or $\Phi_{n,\ominus}$, $d\Phi_{n,\oplus} = d\bar{\Phi}_n \frac{dz}{z}$, in which x_\oplus or x_\ominus has been substituted by the momentum fraction that the initial-state particle carries after the collinear emission zx_\oplus . The infrared safety of O requires that $O(\Phi_{n+1}) \rightarrow O(\Phi_n)$ in the soft or collinear limits.

Eq. (130) is finite as a whole. Nevertheless, the fact that the divergences arise in different phase-space integrals means that the integrals can not be carried out separately, since they are each individually divergent. Therefore, a *subtraction method* is typically employed to rewrite Eq. (126) in a way suitable for numerical calculations. In a subtraction scheme, the soft and collinear divergences that the real contribution \mathcal{R} would develop upon integration are subtracted from it under the integral (over the $n+1$ -particle phase space) by suitable *real counterterms*. These are a set of functions $\mathcal{C}^{(\alpha)}(\Phi_{n+1})$ that have the same divergent structure as $\mathcal{R}(\Phi_{n+1})$ in the soft or collinear limits and are analytically integrable over the (one-particle) phase space of the extra emitted particle. The real counterterms are integrated and added back to the rest of the contributions. The divergences present in the integrated real counterterms, the bare virtual contribution and the collinear counterterms cancel, and the integration over the n -particle phase space can be performed. We now describe this process in a schematic way. We refer to Sec. 2.2 of [34] for a detailed discussion of the subtleties involved with the phase-space arguments.

2.1 Infrared Subtraction

The real contribution in Eq. (130) is rewritten as

$$\begin{aligned} \int d\Phi_{n+1} \mathcal{L} O_{n+1}(\Phi_{n+1}) \mathcal{R}(\Phi_{n+1}) &= \sum_{\alpha} \int d\Phi_{n+1} [\tilde{\mathcal{L}} O_n(\bar{\Phi}_n) \mathcal{C}(\Phi_{n+1})]_{\alpha} \\ &+ \int d\Phi_{n+1} \left\{ \mathcal{L} O_{n+1}(\Phi_{n+1}) \mathcal{R}(\Phi_{n+1}) - \sum_{\alpha} [\tilde{\mathcal{L}} O_n(\bar{\Phi}_n) \mathcal{C}(\Phi_{n+1})]_{\alpha} \right\}, \end{aligned} \quad (131)$$

using a real counterterm for each divergent region α , such that the second line of Eq. (131) is finite in 4 dimensions. Here, $\tilde{\mathcal{L}}$ is as \mathcal{L} , but its arguments correspond to the phase-space configuration that defines α .

In the next step, the first sum on the right hand side of Eq. (131) is divided in two, one sum over the soft and final-state collinear divergences $\{\text{S,FSC}\}$, and the other over the initial-state collinear divergences $\{\text{ISC}\}$. Then, each of these sums is integrated over the appropriate radiation phase space, and we arrive at

$$\begin{aligned} \langle O \rangle &= \int d\Phi_n \mathcal{L} O_n(\Phi_n) [\mathcal{B}(\Phi_n) + \mathcal{V}_b(\Phi_n)] \\ &+ \int d\Phi_{n+1} \left\{ \mathcal{L} O_{n+1}(\Phi_{n+1}) \mathcal{R}(\Phi_{n+1}) - \sum_{\alpha} [\tilde{\mathcal{L}} O_n(\bar{\Phi}_n) \mathcal{C}(\Phi_{n+1})]_{\alpha} \right\} \\ &+ \sum_{\alpha \in \{\text{FSC,S}\}} \left[\int d\bar{\Phi}_n \tilde{\mathcal{L}} O_n(\bar{\Phi}_n) \bar{\mathcal{C}}(\bar{\Phi}_n) \right]_{\alpha} + \sum_{\alpha \in \{\text{ISC}\}} \left[\int d\Phi_{n,\oplus} \tilde{\mathcal{L}} O_n(\bar{\Phi}_n) \bar{\mathcal{C}}(\Phi_{n,\oplus}) \right]_{\alpha} \\ &+ \int d\Phi_{n,\oplus} \tilde{\mathcal{L}} O_n(\bar{\Phi}_n) \mathcal{G}_{\oplus,b}(\Phi_{n,\oplus}) + \int d\Phi_{n,\ominus} \tilde{\mathcal{L}} O_n(\bar{\Phi}_n) \mathcal{G}_{\ominus,b}(\Phi_{n,\ominus}). \end{aligned} \quad (132)$$

Here $\bar{\mathcal{C}}^{(\alpha)} = \int d\Phi_1 \mathcal{C}^{(\alpha)}$, schematically, and these integrated counterterms contain the divergences of the real contribution explicitly as poles in ϵ .

The integrated real counterterms for the initial-state collinear configurations can be combined with the collinear counterterms

$$\mathcal{G}_{\oplus,b}(\Phi_{n,\oplus}) + \sum_{\alpha \in \{\text{ISC}\}} \bar{\mathcal{C}}^{(\alpha)}(\Phi_{n,\oplus}) = \mathcal{G}_{\oplus}(\Phi_{n,\oplus}) + \delta(1-z) \mathcal{G}_{\oplus}^{\text{div}}(\bar{\Phi}_n), \quad (133)$$

which results in a finite part \mathcal{G}_{\oplus} and a divergent part $\mathcal{G}_{\oplus}^{\text{div}}$, in which only soft divergences remain⁴.

After plugging Eq. (133) into Eq. (132), all the remaining divergent parts can be combined as

$$\mathcal{V}(\Phi_n) = \mathcal{V}_b(\Phi_n) + \left[\sum_{\alpha \in \{\text{FSC,S}\}} \bar{\mathcal{C}}^{(\alpha)}(\bar{\Phi}_n) + \mathcal{G}_{\oplus}^{\text{div}}(\bar{\Phi}_n) + \mathcal{G}_{\ominus}^{\text{div}}(\bar{\Phi}_n) \right], \quad (134)$$

⁴Although this is a combination of counterterms that are associated to collinear divergences, these can be tangled up with soft divergences. What this combination achieves is their disentanglement, and additionally the cancelation of the collinear part.

where $\bar{\Phi}_n$ is the underlying configuration of Φ_n for each α . In Eq. (134), all poles are of soft or final-state collinear kind, and completely cancel due to the KLN theorem.

With this, Eq. (132) becomes

$$\begin{aligned} \langle O \rangle &= \int d\Phi_n O_n(\Phi_n) \left[B(\Phi_n) + V(\Phi_n) \right] \\ &+ \int d\Phi_{n+1} O_{n+1}(\Phi_{n+1}) \hat{R}(\Phi_{n+1}) \\ &+ \int d\Phi_{n,\oplus} O_n(\bar{\Phi}_n) G_{\oplus}(\Phi_{n,\oplus}) + \int d\Phi_{n,\ominus} O_n(\bar{\Phi}_n) G_{\ominus}(\Phi_{n,\ominus}), \end{aligned} \quad (135)$$

where the upright contributions stand for the corresponding calligraphic contributions times their luminosities, and we have defined

$$\hat{R}(\Phi_{n+1}) = \left\{ O_{n+1}(\Phi_{n+1}) R(\Phi_{n+1}) - \sum_{\alpha} [O_n(\bar{\Phi}_n) C(\Phi_{n+1})]_{\alpha} \right\}, \quad (136)$$

i.e. the remainder of the real contribution minus the real counterterms. This remainder can be found for each divergent region in a general way by parametrizing the phase space of the emitted particle in that region and analyzing the singular part of the second line of Eq. (132), which results from the integral over the emission variables. In this way, the counterterms are automatically found, since they are precisely those singular parts. We refer to Sec. 2.3 of [34] for details of this procedure. All integrals in Eq. (135) are now separately finite and thus suitable for numerical integration.

2.1.1 Frixione-Kunszt-Signer Subtraction Method

In Eq. (135), we have found an expression that is suitable for numerical integration. Nevertheless, it remains abstract, since the counterterms have not been specified. In an *IR subtraction method*, the real counterterms $\mathcal{C}^{(\alpha)}$ are defined. These are fixed, up to finite parts, by the requirement that \hat{R} is finite for each divergent region, and are necessary for the calculation of the *soft-virtual* contribution of Eq. (134). Several subtraction methods exist, like the commonly used Catani-Seymour (CS) dipole subtraction [70] or the Frixione-Kunszt-Singer (FKS) method [71]. In this subsection, we briefly discuss the FKS method as used in [34]. This method has the advantage of being process independent [53], and it is employed in this work.

As mentioned before, the real counterterms can be naturally found by analyzing the divergent parts of \mathcal{R} . From this point of view, constructing the counterterms corresponds to extracting the divergences from the real contribution. To this end, it is necessary to first disentangle the poles of \mathcal{R} . In the FKS method, this is achieved by decomposing the real contribution as a sum of terms that contain each at most one collinear and one soft divergence associated with each parton

$$\mathcal{R} = \sum_i \mathcal{R}_i + \sum_{ij} \mathcal{R}_{ij}, \quad (137)$$

2.1 Infrared Subtraction

where \mathcal{R}_i carries the divergence associated to the final-state particle i being soft and/or collinear to an initial-state particle and \mathcal{R}_{ij} correspondingly for the final-state particle i becoming soft and/or collinear to another final-state particle j . This separation is achieved by so-called \mathcal{S} -functions, which depend upon the external momenta of the process. The \mathcal{S} -functions must have the following properties:

- If particle m is soft in the present configuration, then $\mathcal{S}_i = \mathcal{S}_{ij} = 0$ if $i \neq m$.
- If particle m is collinear to an initial-state particle, then $\mathcal{S}_m = 1$ and all other \mathcal{S}_i vanish, as does \mathcal{S}_{ij} .
- If particle i is collinear to a final-state particle j , only \mathcal{S}_{ij} and \mathcal{S}_{ij} are nonzero.
- $\sum_i \mathcal{S}_i + \sum_{ij} \mathcal{S}_{ij} = 1$.

Thus, the \mathcal{S} -functions act as selectors for the phase-space configuration of each separate divergent region. With these, one defines $\mathcal{R}_i = \mathcal{S}_i \mathcal{R}$ and $\mathcal{R}_{ij} = \mathcal{S}_{ij} \mathcal{R}$. The precise definition of the \mathcal{S} -functions in the framework employed in this work can be found in [72].

Once this decomposition has taken place, the soft, initial- and final-state collinear singularities can be extracted from \mathcal{R} . Thereby, the finite part $\hat{\mathcal{R}} = \sum_i \hat{\mathcal{R}}_i + \sum_{ij} \hat{\mathcal{R}}_{ij}$ remains, itself decomposed in (finite) contributions associated with each singular region. The extraction of different singularities relies on the factorization properties mentioned in Sec. 1.2.3. It is described in detail in [73] for the case of QCD emission corrections to the production of three jets.

In a similar way, the divergences present in the bare virtual contribution can be extracted, so that [74, 34]

$$\mathcal{V}_b = \mathcal{N} \frac{\alpha_s}{2\pi} \left[- \sum_{i \in \mathcal{I}} \left(\frac{1}{\epsilon^2} C_{f_i} + \frac{1}{\epsilon} \gamma_{f_i} \right) \mathcal{B} + \frac{1}{\epsilon} \sum_{\substack{i, j \in \mathcal{I} \\ i \neq j}} \log \left(\frac{2 k_i \cdot k_j}{Q^2} \right) \mathcal{B}_{ij} + \mathcal{V}_{\text{fin}} \right], \quad (138)$$

with the normalization factor

$$\mathcal{N} = \frac{(4\pi)^\epsilon}{\Gamma(1-\epsilon)} \left(\frac{\mu_r^2}{Q^2} \right)^\epsilon. \quad (139)$$

The *Ellis-Sexton* scale Q^2 is chosen as $Q = \mu_r$ in the implementation of the FKS subtraction used in this work. In Eq. (138) the sums run over all external partons \mathcal{I} . In the first term inside the square brackets, the C_i and γ_i are finite coefficients that multiply the Born contribution \mathcal{B} . These are related to the color properties of the parton with flavor f_i . They can be found in Ref. [34].

In the second term, k_i is the momentum of the i -th parton and the \mathcal{B}_{ij} are the *color-correlated* or *color-linked* Born amplitudes. Matrix elements involving color-charged particles depend upon their color indices and can be compatible with different sets of values of color indices. The color-correlated amplitude \mathcal{B}_{ij} is built

by multiplying the amplitude $\mathcal{M}_{\{c_k\}}$, with color indices $\{c_k\}$ by the amplitude

$$\left(\mathcal{M}_{\{c_k\}}^\dagger\right)_{\substack{c_i \rightarrow c'_i \\ c_j \rightarrow c'_j}},$$

which is the complex conjugate of $\mathcal{M}_{\{c_k\}}$ with the color indices c_i, c_j substituted by c'_i, c'_j . Then, the sum over all spins and color configurations is performed, weighted by appropriate color factors. The definition is

$$\mathcal{B}_{ij} = -N_{cc} \sum_{\substack{\text{spins} \\ \text{colours}}} \mathcal{M}_{\{c_k\}} \left(\mathcal{M}_{\{c_k\}}^\dagger\right)_{\substack{c_i \rightarrow c'_i \\ c_j \rightarrow c'_j}} T_{c_i, c'_i}^a T_{c_j, c'_j}^a. \quad (140)$$

For gluons $T_{cb}^a = if_{cab}$, where f_{abc} are the structure constants of $SU(3)$. For incoming quarks $T_{\alpha\beta}^a = \lambda_{\alpha\beta}^a$, and for antiquarks $T_{\alpha\beta}^a = -\lambda_{\beta\alpha}^a$. \mathcal{B}_{ij} is related to the exchange of a soft gluon between particles i and j , and appears in the soft limit of the real matrix elements [75], so that the ϵ pole that it multiplies in Eq. (138) is canceled. The prefactor N_{cc} includes the partonic flux factor $(2\hat{s})^{-1}$, as well as the color and spin normalization. Equation (138) defines the finite part of the virtual contribution, \mathcal{V}_{fin} .

After the divergent terms of \mathcal{V}_b have been cancelled by the real and collinear counterterms, Eq. (134) becomes

$$\mathcal{V} = \frac{\alpha_s}{2\pi} \left(\mathcal{Q}\mathcal{B} + \sum_{\substack{i,j \in \mathcal{I} \\ i \neq j}} \mathcal{I}_{ij} \mathcal{B}_{ij} + \mathcal{V}_{\text{fin}} \right), \quad (141)$$

where \mathcal{Q} corresponds to the collinear remnants and the \mathcal{I}_{ij} to the soft remnants or *eikonal integrals*. The \mathcal{Q} and \mathcal{I}_{ij} are finite functions of the partons momenta and flavors, of the factorization scale μ_f and the Ellis-Sexton scale Q , which is set equal to μ_r . Their expressions are somewhat involved, and can be found in Sec. 2.4.2 of Ref. [34].

2.2 Parton Showers

As mentioned in Sec. 1.5, parton showers are an important step towards a realistic simulation of hadronic collisions. The hard scattering described by the fixed order calculation produces highly energetic particles which radiate other particles, thereby losing energy. After the energy of all final-state particles has decreased below a certain level, (non-perturbative) hadronization processes ensue. A PS program simulates these emissions and thus describes an evolution from the hard energy scale down to the hadronization scale, at which particles are detected in collision experiments.

From the point of view of matrix elements, the radiation off final-state particles of a $2 \rightarrow n$ hard process corresponds to Feynman diagrams with one more external

2.2 Parton Showers

line per radiated particle, attached to the original n final-state lines. Consequently, the probability for these emissions is suppressed by one factor of α_s per emission. On the other hand, according to the discussion in Sec. 1.2.3, such emissions are enhanced in the soft and collinear regimes, and their probability even becomes divergent in these limits if no virtual corrections are taken into account. This enhancement is logarithmic, and can be strong enough to counteract the factor of α_s that accompanies every radiation. Thus, considering these emissions in the modeling of hadronic collisions is necessary. This can not be achieved using matrix elements with ever higher multiplicities, which become increasingly complicated to calculate. Rather, the emissions are described using an approximation that is valid in the region of phase space in which they are enhanced. This is accomplished by the PS, which is added as an improvement on top of the calculation of a hard process. In this way, a PS is similar to analytic *resummation techniques*, which are employed to formally resum the large logarithms from soft and collinear emissions and improve fixed order calculations.

The principle behind a PS is to model the radiation as a sequence of independent emissions. This neglects interference effects that would be taken into account in the matrix element approach. The probability of each emission is obtained from the factorization property that we have previously discussed. In this context, it means that the cross section of a $2 \rightarrow (n+1)$ QCD process, where the $(n+1)$ -th particle is emitted by an external leg, can be written as [76]

$$d\sigma_{n+1} \approx d\sigma_n \sum_{i,j} \frac{\alpha_s}{2\pi} \frac{d\theta^2}{\theta^2} P_{ij}(z) dz, \quad (142)$$

in the collinear regime. Here, σ_n is the cross section of the process without the extra emission and the P_{ij} are the Altarelli-Parisi functions introduced in Sec. 1.4. The variables θ and z parametrize the radiation phase space $d\Phi_1$, and the sum runs over emitters i and emitted partons j . This property is ultimately what leads to Eq. (108), and is the first step towards the factorization theorem.

From Eq. (142), we read off that the probability of an emission in an interval $[\theta, \theta + d\theta]$ is

$$d\mathcal{K}(\theta) = \frac{\alpha_s}{2\pi} \frac{d\theta^2}{\theta^2} \int dz P(z), \quad (143)$$

where we have dropped the sum over partons to simplify the notation. To prevent the collinear divergence as $\theta \rightarrow 0$, a PS considers only *resolvable emissions*, i.e. those above a finite resolution threshold θ_{\min} . This threshold limits the integration over z in Eq. (143), which becomes

$$d\mathcal{K}(\theta) = \frac{\alpha_s}{2\pi} \frac{d\theta^2}{\theta^2} \int_{z_{\min}}^{z_{\max}} dz P(z), \quad (144)$$

with integration limits $z_{\min/\max}$ that depend upon θ_{\min} .

In a PS, the emissions off a given emitter are ordered with respect to an *evolution variable* t that is proportional to the invariant mass of the branching. The $(i + 1)$ -th branching is forced to occur at a value of $t_{i+1} < t_i$. A natural choice for the evolution variable is the angle θ^2 from Eq. (144). In fact, since $d\mathcal{K}(\theta) \sim d\theta^2/\theta^2$, a PS can use any evolution variable t with the same collinear limit for $\theta \rightarrow 0$,

$$\frac{dt}{t} = \frac{d\theta^2}{\theta^2}. \quad (145)$$

Common choices besides θ are the virtuality of the emitter or the transverse momentum of the radiated particle. In the following, we will use a general evolution variable t , bounded from below by a finite t_{\min} and from above by t_{\max} , which corresponds to the scale at which the hard process occurs.

A PS is required to generate emissions using Eq. (144) in a unitary way. This means that, for a given interval in the evolution variable, we require that a branching either happens or that it does not happen. In other words, the sum of the probability $\Delta(t_{\max}, t_1)$ that no emission occurs between t_{\max} and t_1 , plus the probability that the first splitting takes place at some value in between, must be equal to one:

$$1 = \Delta(t_{\max}, t_1) + \int_{t_1}^{t_{\max}} dt \Delta(t_{\max}, t) d\mathcal{K}(t). \quad (146)$$

This equation can be solved iteratively for $\Delta(t_{\max}, t_1)$, which yields

$$\Delta(t_{\max}, t_1) = \exp \left\{ - \int_{t_1}^{t_{\max}} d\mathcal{K}(t) \right\}. \quad (147)$$

To simulate the *first* emission, we determine the probability that it occurs at a given value t_1 . It is proportional to the probability $\Delta(t_{\max}, t_1)$ that *no emission* happens between the values t_{\max} and t_1 times the probability that an emission occurs *exactly* at t_1 , namely $d\mathcal{K}(t_1)$. This means that

$$\Delta(t_{\max}, t_1) d\mathcal{K}(t_1) = d\Delta(t_{\max}, t_1), \quad (148)$$

according to Eq.(147). Equation (148) can be sampled to find a value for t_1 . Subsequent emissions can be treated in the same way: the probability for the second emission to occur at t_2 is

$$d\Delta(t_1, t_2) = \Delta(t_1, t_2) d\mathcal{K}(t_2),$$

and so on. More specifically, the scale of the i -th emission by a given emitter is found by generating a pseudo-random number $r_i \sim U(0, 1)$ and solving $r_i = \Delta(t_{i-1}, t_i)$ for t_i . If $t_i < t_{\min}$, the would-be emitter is considered part of the final state and no emission is produced. If $t_i > t_{\min}$, then a splitting is triggered, and the kinematics and final-state parton species of the $1 \rightarrow 2$ process are generated according to

2.3 Matching of NLO Calculations to PS

the Altarelli-Parisi kernels, under consideration of four-momentum conservation⁵. The azimuthal angle is uniformly generated, since the underlying approximation does not describe any angular correlations. This process is iterated until $t_i < t_{\min}$, which marks the end of the emissions from this emitter. This chain of emissions is constructed for every particle, until eventually all of them have been evolved down to the hadronization scale.

The quantity $\Delta(T, t)$ is called *Sudakov form factor*, and it contains contributions from all orders of α_s . It describes the finite probability that no resolvable emission occurs between the scales T and t , which corresponds to the sum of virtual and soft/collinear emissions below the resolution threshold. Consequently, the description of emission by a PS is called an *all-orders* calculation, as opposed to the fixed-order calculation of the hard process. By describing the emission with the Sudakov form factor, the logarithmic enhancement of soft and collinear branchings is taken into account at *leading-logarithmic order* [53, 77].

2.3 Matching of NLO Calculations to Parton Showers

The PS approach was originally created to supplement hard processes calculated at LO. In that case, the expectation value of an IR-safe observable is given by

$$\langle O \rangle_{\text{PS}} = \int d\Phi_n B(\Phi_n) \left\{ O_n(\Phi_n) \Delta(t_{\max}, t_{\min}) \right. \quad (149)$$

$$\left. + \int_{t_{\min}}^{t_{\text{hard}}} O_{n+1}(\Phi_{n+1}) \Delta(t_{\max}, t(\Phi_1)) d\mathcal{K}(\Phi_1) \right\}, \quad (150)$$

up to one emission. Here, we have used the notation of Eq. (135) for the Born contribution. The first term on the right hand side of Eq. (149) is associated with the probability of no emission, and the second one with that of one emission. Because of the unitarity of the PS, the LO result for $\langle O \rangle$ is recovered upon phase-space integration in Eq. (149).

It is desirable to combine the improved accuracy of an NLO calculation with the resummation effect of a PS, since each provides a good description of radiation in complementary regions of phase space. To this end, it is not possible to simply substitute the Born contribution in Eq. (149) by some higher-order counterpart. Ultimately, the issue boils down to the fact that the NLO cross section already describes an extra emission with respect to the LO process, which is something that the PS is also supposed to do. This can be seen intuitively with the help of the diagrams shown in Fig. 7. There, the soft and/or collinear emissions, represented by

⁵More specifically, the parton shower must give the particle that emits, which a-priori is on-shell, a non-zero virtuality so that it can branch into two on-shell particles. The required energy must come from other particles involved in the event, which recoil against the splitting. The necessary redistribution of momenta can be done in different ways, and some PS programs have different schemes to choose from.

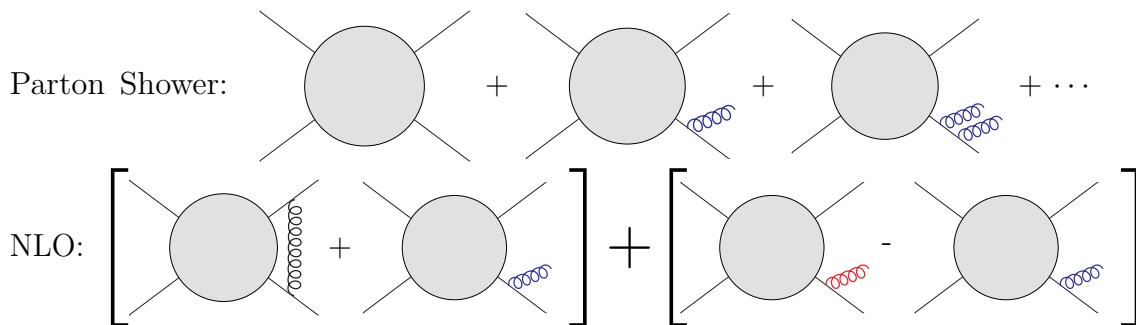


Figure 7: Diagrammatic sketch of the contributions taken into account by a PS and an NLO calculation. The gray blob stands for the LO hard process. The red gluon line stands for an emission of arbitrary hardness, while the blue ones stand for soft/collinear ones.

blue gluon lines, are taken into account in both the PS and the NLO calculation. Thus, care must be taken to prevent the double counting of the first emission. A solution one might think of is to generate the first emission using the NLO contribution only, and start the PS only from the second extra emission onwards. Although this would achieve NLO accuracy, the description of the first emission would not have the desired resummation effect provided by the PS. One solution to this problem is provided by the POWHEG method [34], which stands for *Positive Weight Hardest Emission Generator*. In it, the first emission, with respect to a “core” LO process, is generated using a modified Sudakov form factor. This achieves NLO accuracy of the result while also providing all emissions beyond LO with the resummation effect of the PS.

The main formula of the POWHEG method can be understood by making the following observations. First, consider the expansion up to NLO of the all-orders expression in Eq. (149):

$$\begin{aligned}
 \langle O \rangle_{\text{PS}} &= \int d\Phi_n B(\Phi_n) \left\{ O_n(\Phi_n) \Delta(t_{\text{hard}}, t_{\text{min}}) \right. \\
 &\quad \left. + \int O_{n+1}(\Phi_{n+1}) \Delta(t_{\text{max}}, t(\Phi_1)) d\mathcal{K}(\Phi_1) \right\} \\
 &= \int d\Phi_n B(\Phi_n) O_n(\Phi_n) \\
 &\quad + \int d\Phi_n \int d\mathcal{K}(\Phi_1) B(\Phi_n) [O_{n+1}(\Phi_{n+1}) - O_n(\Phi_n)] + \mathcal{O}(\alpha_s^{k+2}),
 \end{aligned} \tag{151}$$

where we plugged in $\Delta = 1 - \int d\mathcal{K} + \mathcal{O}(\alpha_s^2)$ and k is the order of B .

2.3 Matching of NLO Calculations to PS

Now, we return to Eq. (135):

$$\begin{aligned}
\langle O \rangle_{\text{NLO}} &= \int d\Phi_n O_n(\Phi_n) [B(\Phi_n) + V(\Phi_n)] \\
&\quad + \int d\Phi_{n,\oplus} O_n(\bar{\Phi}_n) G_{\oplus}(\Phi_{n,\oplus}) + \int d\Phi_{n,\ominus} O_n(\bar{\Phi}_n) G_{\ominus}(\Phi_{n,\ominus}) \\
&\quad + \int d\Phi_{n+1} \left\{ O_{n+1}(\Phi_{n+1}) R(\Phi_{n+1}) - O_n(\bar{\Phi}_n) C(\Phi_{n+1}) \right\}, \quad (152)
\end{aligned}$$

where we have written out the \hat{R} contribution and we assume that here is only one singular region for simplicity. We can rewrite Eq. (152) as

$$\begin{aligned}
\langle O \rangle_{\text{NLO}} &= \int d\Phi_n O_n(\Phi_n) \left[B(\Phi_n) + V(\Phi_n) + \int d\Phi_1 [R(\Phi_{n+1}) - C(\Phi_{n+1})] \right] \\
&\quad (153) \\
&\quad + \int d\Phi_{n,\oplus} O_n(\bar{\Phi}_n) G_{\oplus}(\Phi_{n,\oplus}) + \int d\Phi_{n,\ominus} O_n(\bar{\Phi}_n) G_{\ominus}(\Phi_{n,\ominus}) \\
&\quad + \int d\Phi_{n+1} R(\Phi_{n+1}) [O_{n+1}(\Phi_{n+1}) - O_n(\Phi_n)],
\end{aligned}$$

where we have used that O is an IR-safe observable, and signal with blue the terms that cancel out to give Eq. (152). We introduce the quantity

$$\begin{aligned}
\bar{B}(\Phi_n) &= B(\Phi_n) + V(\Phi_n) \\
&\quad + \int d\Phi_1 [R(\Phi_{n+1}) - C(\Phi_{n+1})] + \int \frac{dz}{z} [G_{\oplus}(\Phi_{n,\oplus}) + G_{\ominus}(\Phi_{n,\ominus})] \quad (154)
\end{aligned}$$

where z is the fraction of momentum of the incoming parton after radiation (cf. Sec. 2.1), and insert it in Eq. (153) to obtain

$$\begin{aligned}
\langle O \rangle_{\text{NLO}} &= \int d\Phi_n \bar{B}(\Phi_n) O(\Phi_n) \\
&\quad + \int d\Phi_n d\Phi_1 R(\Phi_n, \Phi_1) [O_{n+1}(\Phi_{n+1}) - O_n(\Phi_n)]. \quad (155)
\end{aligned}$$

This equation has the same form as Eq. (151), and we can transform $\langle O \rangle_{\text{PS}}$ up to NLO into $\langle O \rangle_{\text{NLO}}$ by making the replacements

$$\begin{aligned}
B(\Phi_n) &\quad \rightarrow \bar{B}(\Phi_n), \\
d\mathcal{K}(\Phi_1) B(\Phi_n) &\quad \rightarrow d\Phi_1 R(\Phi_{n+1}),
\end{aligned}$$

or equivalently

$$d\mathcal{K}(\Phi_1) \rightarrow d\Phi_1 \frac{R(\Phi_{n+1})}{\bar{B}(\Phi_n)} \quad (156)$$

where $\Phi_1 = \Phi_1(t, z)$. This is precisely what is done in the POWHEG method, where the expectation-value of O up to the first emission is given by

$$\begin{aligned} \langle O \rangle_{\text{PWG}} = & \int d\Phi_n \bar{B}(\Phi_n) \left\{ O_n(\Phi_n) \Delta_{\text{PWG}}(\Phi_n, p_T^{\text{min}}) \right. \\ & \left. + \int d\Phi_1 O_{n+1}(\Phi_{n+1}) \Delta_{\text{PWG}}(\Phi_n, p_T(\Phi_{n+1})) \frac{R(\Phi_{n+1})}{\bar{B}(\Phi_n)} \Theta(p_T - p_T^{\text{min}}) \right\}, \end{aligned} \quad (157)$$

with the modified Sudakov form factor

$$\Delta_{\text{PWG}}(\Phi_n, p_T) = \exp \left\{ - \int d\Phi_1 \frac{R(\Phi_{n+1})}{\bar{B}(\Phi_n)} \Theta(k_T(\Phi_{n+1}) - p_T) \right\}, \quad (158)$$

where k_T is a function that approaches the transverse momentum of the emitted particle with respect to the emitter in the singular limit. The Heavyside function in Eq. (157) enforces the infrared cut that we called t_{min} before.

By sampling Eq. (158) for a value of p_T , the first radiation is generated in the POWHEG method using transverse momentum as the evolution scale. This scale is communicated to the PS program. If the shower is p_T -ordered, then it simply generates subsequent radiation respecting the POWHEG scale as its upper bound. If the shower simulator uses a different ordering scale, then the hardest emission produced by it might not be the first one, and a check needs to be in place to ensure that the radiation it produces does not surpass the POWHEG radiation in p_T . This can be achieved through a *veto algorithm* in the PS program. To finish this section, we remark that the name of the POWHEG method is due to the *weight* $\langle O \rangle_{\text{PWG}}$ being positive whenever \bar{B} is, as opposed to the weight given by other commonly used matching methods.

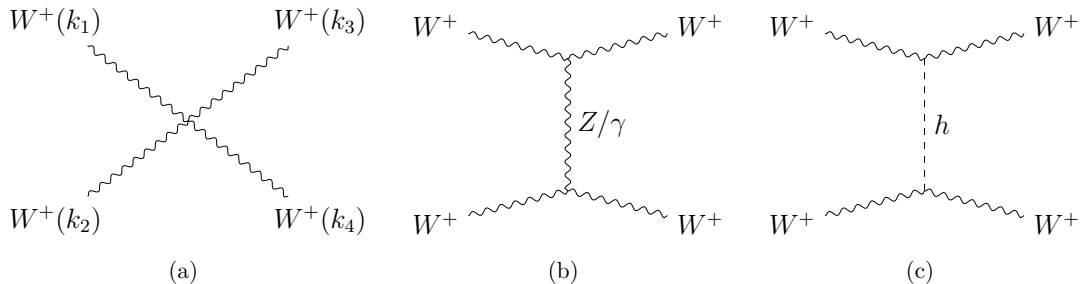


Figure 8: Contributions to the $W^+W^+ \rightarrow W^+W^+$ process at LO. Diagram 8(a) represents the so-called contact interaction and is proportional to the QGC of four W bosons. The contribution 8(b) involves the exchange of a Z boson or a photon, and involves two triple gauge couplings. Diagram 8(c) corresponds to the exchange of a Higgs boson, and is sensitive to the HWW coupling. The diagrams 8(b) and 8(c) must be symmetrized with respect to the identical particles in the final state to obtain all contributions.

3 Vector Boson Scattering and the $pp \rightarrow W^+W^+jjj$ Process

In this section, we turn to the process under investigation, the scattering of two W^+ bosons. We begin by considering pure VBS of on-shell bosons, $W^+W^+ \rightarrow W^+W^+$, and recalling the cancellation mechanism that makes VBS especially sensitive to deviations in EWSM and the EW sector of the SM. Afterwards, we consider VBS at the LHC and motivate its calculation within the $pp \rightarrow W^+W^+jjj$ process.

As mentioned in the introduction of this thesis, delicate cancellations prevent VBS scattering amplitudes from violating unitarity in the high-energy regime. We now illustrate this mechanism for W^+W^+ scattering at LO in a schematic way following Ref. [17]. Assuming a stable pair of W^+ bosons in the initial and final states, the process at hand receives contributions from the three Feynman diagrams in Fig. 8, where the k_i denote the momenta of the external particles. We consider only longitudinally-polarized W^+ bosons, which are responsible for the dangerous growth of the scattering amplitude with energy⁶. Going to the high-energy regime, where the center-of-mass energy $s = (k_1 + k_2)^2 \gg 4M_W^2$, the contributions of each diagram in Fig. 8 to the matrix element read [17]

⁶The longitudinal polarization vector ε_L is proportional to the particle's energy, while transverse polarization vectors ε_T are not. Consider for example a particle with momentum $p = (E, 0, 0, p_z)$. Then, $\varepsilon_T^{(1/2)} = (0, 1, \pm i, 0)$ for example, but $\varepsilon_L = \frac{1}{m}(p_z, 0, 0, E)$. Thus, only $\varepsilon_L \rightarrow p/m$ at high energies.

$$i\mathcal{M}_{(a)} = \frac{e_{\text{EM}}^2}{4 \sin \theta_W} \left[\frac{s^2}{M_W^4} - \frac{2t^2}{M_W^4} - \frac{2st}{M_W^4} - \frac{4s}{M_W^2} - \frac{16t^2}{M_W^2 s} - \frac{8t}{M_W^2} - \frac{32t}{s} - \frac{96t^2}{s^2} \right] \quad (159)$$

$$i\mathcal{M}_{(b)} = \frac{e_{\text{EM}}^2}{4 \sin \theta_W} \left[-\frac{s^2}{M_W^4} + \frac{2t^2}{M_W^4} + \frac{2st}{M_W^4} + \frac{3s}{M_W^2} + \frac{16t^2}{M_W^2 s} + \frac{8t}{M_W^2} + \frac{32t}{s} + \frac{96t^2}{s^2} \right. \\ \left. + 4 \sin \theta_W \left(\frac{s-u}{t} + \frac{s-t}{u} \right) + \frac{(1-2\sin^2 \theta_W)^2}{1-\sin \theta_W} \left(\frac{s-u}{t-M_Z^2} + \frac{s-t}{u-M_Z^2} \right) + 4 \right] \quad (160)$$

$$i\mathcal{M}_{(c)} = \frac{e_{\text{EM}}^2}{4 \sin \theta_W} \left[\frac{s}{M_W^2} - 4 - \left(\frac{m_h^2}{M_W^2} + 4 + \frac{4M_W^2}{m_h^2} + \frac{8m_h^2}{s} \right) \left(\frac{m_h^2}{t-m_h^2} + \frac{m_h^2}{u-m_h^2} \right) \right. \\ \left. - \frac{2m_h^2}{M_W^2} - \frac{16m_h^2}{s} \right] \quad (161)$$

up to terms of $\mathcal{O}(\frac{4M_W^2}{s})$, where $t = (k_1 - k_3)^2$ and $u = (k_1 - k_4)^2$ and the expressions for the gauge and HWW couplings have been inserted. In $\mathcal{M}_{(b)}$, the contributions of a Z -boson and of photon exchange are summarized. Evidently, $\mathcal{M}_{(a)}$ and $\mathcal{M}_{(b)}$ exhibit the strongest dependence on s , which is quadratic. This dependence cancels out upon combining contributions $\mathcal{M}_{(a)}$ and $\mathcal{M}_{(b)}$, as can be seen when adding Eqs.(159) and (160), leaving only the subleading term $-s/M_W^2$ and the second line of Eq. (160), whose terms do not grow with energy. To cancel the term of $\mathcal{O}(s)$ in $\mathcal{M}_{(a)} + \mathcal{M}_{(b)}$, the contribution due to Higgs exchange from Eq. (161) is necessary. The full amplitude, given by $\mathcal{M}_{(a)} + \mathcal{M}_{(b)} + \mathcal{M}_{(c)}$, is well-behaved in the high energy regime. Nevertheless, terms

$$\frac{m_h^2}{M_h^2} \left(\frac{t}{t-m_h^2} + \frac{u}{u-m_h^2} \right), \quad (162)$$

which originate from $\mathcal{M}_{(c)}$, do rise with energy if $s < m_h^2$ and are not necessarily small and can even violate the unitarity of the S -matrix. Following this idea, the upper bound of around 1 TeV was given for the Higgs boson mass by Lee, Quigg and Thacker [4] 25 years before its discovery⁷.

After seeing this sketch of the cancellation mechanism, it becomes clear that deviations in the SM couplings could spoil it. For example, an alteration of the QGC that is not compensated by a corresponding change in the TGC could potentially lead to a scattering amplitude proportional to s^2 . Similarly, a modified WWH coupling could lead to an energy growth $\sim s$. This would not mean that unitarity is in fact violated, but simply that our model is incomplete and physics beyond the SM are responsible for the finiteness of physical VBS cross sections. In modern studies, anomalous couplings are parametrized using *effective field theories* (EFT), in which

⁷In Ref. [4], the upper bound was formulated upon investigation of neutral VBS processes, but the reasoning is the same for W^+W^+ scattering, see Ref. [17].

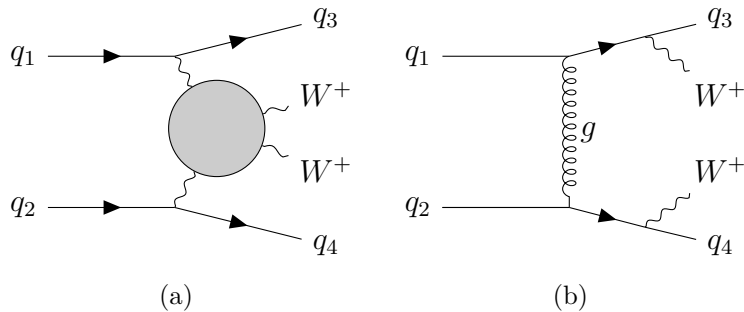


Figure 9: 9(a): Generic diagram of W^+W^+ scattering at the LHC induced by quarks q_1 and q_2 . The grey circle stands for any scattering topology, like the ones in Fig.8. 9(b): representative diagram of QCD-induced W^+W^+jj production at the LHC at $\mathcal{O}(\alpha_{\text{em}}^2\alpha_s^2)$.

new terms are added to the SM Lagrangian in a systematic way. In Ref. [78], this approach⁸ was used to constrain new-physics effects using experimental data from the LHC of all available VBS processes. We now turn to a discussion of how these processes arise and are detected at a hadron collider.

At the LHC, VBS events occur when the EW bosons, each emitted by a parton of each proton, scatter off each other. Figure 9(a) shows the general form of such a process, where the grey circle stands for any pure VBS diagram. Embedding any of the diagrams in Fig.8 in place of the grey circle of Fig. 9(a) results in a LO contribution to VBS at the LHC. As these diagrams make clear, VBS processes occur purely via EW interactions and their cross section is of $\mathcal{O}(\alpha_{\text{em}}^4)$. The vector bosons in the final state are accompanied by two partons, i.e. the quarks that emitted the vector bosons in the first place, which typically give rise to two jets. As we will see in Sec. 3.2.1, these jets are mainly very forward and well-separated and represent the specific signature of VBS processes.

There are also QCD-induced contributions to the production of two W^+ bosons and two jets at the LHC. These are of $\mathcal{O}(\alpha_{\text{em}}^2\alpha_s^2)$ at LO and cannot embed VBS. An example diagram of such a process is shown in Fig. 9(b). Since no VBS is possible at that order, we consider QCD-induced W^+W^+jj production as a different process and do not include it in the calculations of this work. We remark that diagrams like the one in Fig. 9(b) do not only lead to contributions to the cross section of $\mathcal{O}(\alpha_{\text{em}}^2\alpha_s^2)$, but also to interference contributions of $\mathcal{O}(\alpha_{\text{em}}^3\alpha_s)$ which are neglected too. In general, this artificial separation of contributions of different orders to the same final state is not necessarily suitable for comparison with experimental data, even if it is theoretically well defined by the order of the perturbative expansion. Moreover, one generally expects that cross sections of QCD-induced processes are larger, because the strong coupling constant is larger than the electroweak one. In

⁸Specifically, the Standard Model EFT was employed, in which the new operators are built of SM fields and respect the SM symmetries.

the present case, however, the aforementioned signature of VBS events allows for a meaningful separation. The QCD-induced background to VBS tends to produce more central final-state jets [5], which makes it possible to distinguish VBS events from it by considering only some phase-space regions, namely those without central jets.

Until now, our discussion of VBS at the LHC has been on the level of FO calculations. As we have seen, the LO approximation describes two jets in the final state. On the other hand, realistic events at a hadron collider can have many jets, as we have seen in Sec. 1.6. Because of the lack of color exchange between initial-state quarks, the additional or *subleading* jets in VBS processes also display a characteristic forward behavior [5], in contrast to the subleading jets of QCD-induced processes. This fact can be leveraged in event-selection strategies, and it lead to the development of the *central-jet-veto* (CJV) technique [79, 80, 81], which is designed to exclude events in which the rapidities of the subleading jets lie between those of the LO jets. Although precise predictions for the additional jets are generally desirable, understanding their behavior is especially important if the event selection is based upon their kinematics.

To model subleading jets, one can combine a LO calculation with a PS simulation. The emissions produced by the PS, see Secs. 1.5 and 2.2, are the origin of the additional jets, which are thus described in the PS approximation. A better description of subleading jets is achieved by first performing an NLO calculation. Then, a third jet may arise as real radiation. In this case, the third jet is described as tree-level only, namely by the real matrix elements. The NLO calculation can be matched to a PS, see Sec.2, to further improve the description of the third jet by including leading-logarithmic effects and possibly produce even more jets.

It is however possible to go a step further and achieve a full NLO description of the third jet within the framework of NLO calculations matched to PS. For this, one can consider EW W^+W^+jjj production as the LO process. Then, the third jet is described by tree-level contributions of $\mathcal{O}(\alpha_{\text{em}}^4\alpha_s)$ as well as loop- and tree-level ones of $\mathcal{O}(\alpha_{\text{em}}^4\alpha_s^2)$, and a fourth jet arises as part of the real-emission corrections. This is the strategy that we pursue in this work.

In the remaining of this section, we discuss the scattering of two W^+ bosons associated with three jets as part of the underlying process $pp \rightarrow W^+W^+jjj$. In Sec. 3.1 we review all $\mathcal{O}(\alpha_{\text{em}}^4\alpha_s)$ contributions to the underlying process, as well as their corrections at NLO in QCD. We present the partonic subprocesses that contribute to the hadronic process and their characteristic Feynman diagrams. In Sec. 3.2, we discuss how the VBS signature not only allows for the separation from the QCD-induced background, but also for the disentanglement of different contributions within the order $\alpha_{\text{em}}^4\alpha_s$. We then use Feynman diagrams to distinguish the relevant classes of subprocesses and define which contributions to the underlying process we choose to consider as VBS and why.

3.1 Electroweak Production of W^+W^+jjj at the LHC

3.1 Electroweak Production of W^+W^+jjj at the LHC

At order $\alpha_{\text{em}}^4\alpha_s$, two possible types of initial state exist, defining two types of subprocesses, which we generally denote as $q_1q_2 \rightarrow W^+W^+q_3q_4g$ and $gq_1 \rightarrow W^+W^+q_2q_3q_4$. Here, the q_i stand for arbitrary quarks or antiquarks, although actual subprocesses of course need to respect the conservation of charge and fermion number. We now discuss these subprocesses in some detail, with emphasis on the topologies that arise in each case. In the following, we will often omit the W^+ bosons when writing a subprocess, and will refer to each subprocess using only the initial state when no confusion is possible. Furthermore, we will only consider (anti)quarks of the first and second generations in our discussion. The reasons for excluding top and bottom quarks will become clear in the following.

We first consider the qq ($\bar{q}\bar{q}$)-type subprocesses, initiated by two (anti)quarks. They are:

$$\textcircled{1} uc \rightarrow dsq, \quad \textcircled{2} \bar{d}\bar{s} \rightarrow \bar{u}\bar{c}g \quad \textcircled{3} uu \rightarrow ddg \quad (cc \rightarrow ssg), \quad \textcircled{4} \bar{d}\bar{d} \rightarrow \bar{u}\bar{u}g \quad (\bar{s}\bar{s} \rightarrow \bar{c}\bar{c}g).$$

Although there are six different ones, some of them share the same matrix element, which we have denoted using parentheses, and only four are truly distinct. Furthermore, $\textcircled{1}$ and $\textcircled{2}$ are related by crossing symmetry, as well as $\textcircled{3}$ and $\textcircled{4}$.

Figure 10 depicts exemplary Feynman diagrams that contribute to these channels. In all of them, there are two (anti)quark lines connecting the initial and final states, which we will often refer to as upper (q_1 to q_3) or lower (q_2 to q_4). These are connected by the t -channel exchange of electroweak particles. This t -channel might be a single propagator (Fig. 10, upper left) or contain further electroweak vertices (Fig. 10, upper center, right and bottom row). In the former case, the W^+ bosons of the final state are radiated by the quark lines, as is the gluon. In the latter, they may also originate from the vertices between quark lines. We point out that no s -channel topologies contribute to the qq ($\bar{q}\bar{q}$) subprocesses. Specifically, we mean that no bosonic propagator has a vertex from which only final-state particles originate.

The $q\bar{q}$ subprocesses, initiated by a quark and an antiquark, are

$$\textcircled{5} u\bar{s} \rightarrow d\bar{c}g \quad (c\bar{d} \rightarrow s\bar{u}g), \quad \textcircled{6} u\bar{d} \rightarrow s\bar{c}g \quad (c\bar{s} \rightarrow d\bar{u}g), \quad \textcircled{7} u\bar{d} \rightarrow d\bar{u}g \quad (c\bar{s} \rightarrow s\bar{c}g).$$

These are related to $\textcircled{1} - \textcircled{4}$ by crossing symmetry, but we discuss them separately for the following reason. If the incoming quark and antiquark are not of the same generation, as in channel $\textcircled{5}$, the Feynman diagrams that arise are of the kinds shown in Fig. 10 and contain no s -channel. On the other hand, diagrams that contribute to channels $\textcircled{6}$ and $\textcircled{7}$ also include s -channel topologies, with up to three resonant propagators. Some examples are shown in Fig. 11. All in all, there are 12 LO subprocesses without gluons in the initial state.

Finally, the $g\bar{q}$ subprocesses can be obtained from some $q\bar{q}$ subprocesses by crossing the gluon from the final to the initial state and an initial-state (anti)quark

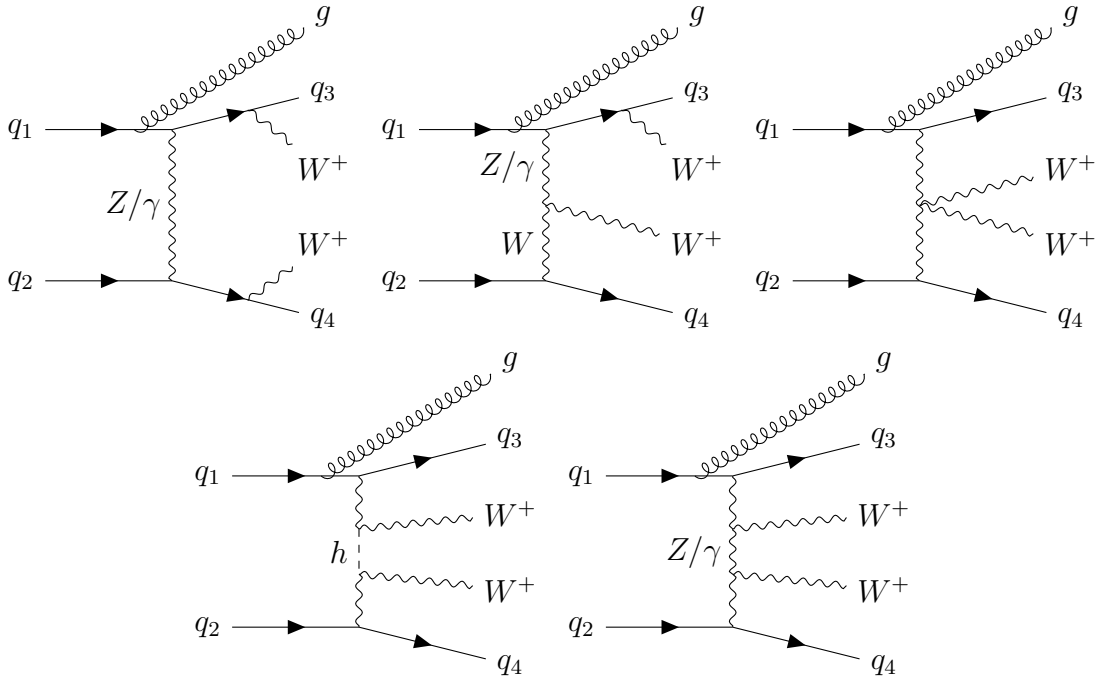


Figure 10: Exemplary Feynman diagrams of qq -initiated subprocesses of the process $pp \rightarrow W^+W^+jjj$ at LO in QCD.

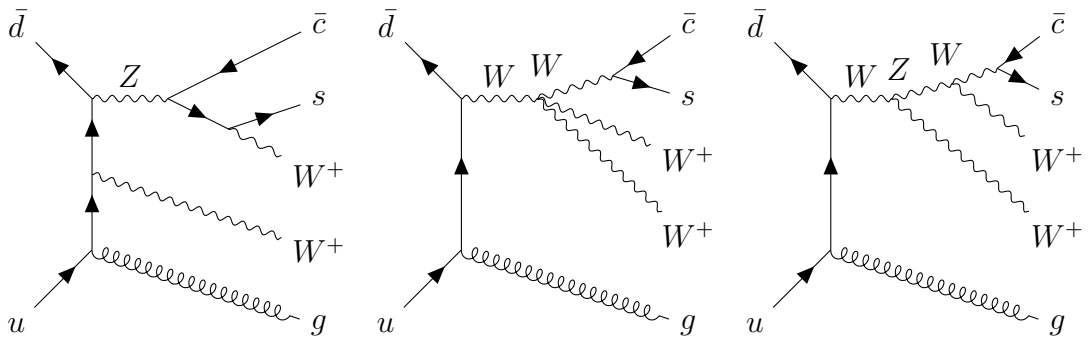


Figure 11: Exemplary leading-order Feynman diagrams of the $q\bar{q}$ subprocesses with one, two and three resonant propagators (left to right).

3.1 Electroweak Production of W^+W^+jjj at the LHC

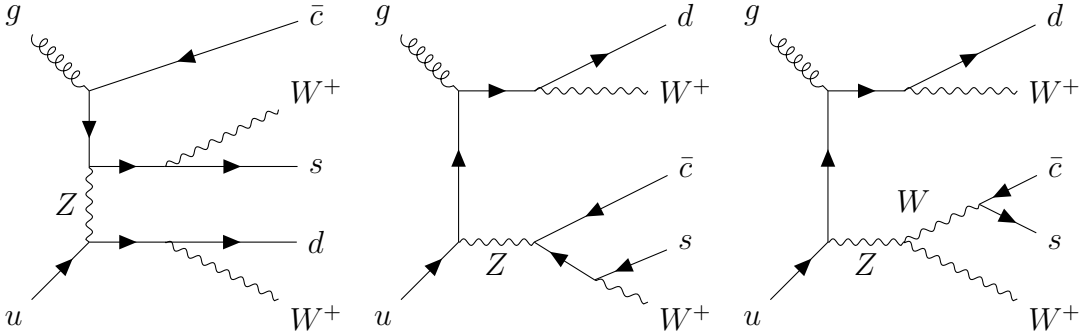


Figure 12: Exemplary leading-order Feynman diagrams of the gq -type subprocess $gu \rightarrow ds\bar{c}$ with zero, one and two s -channel propagators, from left to right.

to the final state. One obtains eight distinct subprocesses, some of which have the same matrix element:

$$\begin{aligned} \textcircled{8} \quad gu \rightarrow ds\bar{c} \quad (gc \rightarrow sd\bar{u}), \quad \textcircled{9} \quad gu \rightarrow dd\bar{u} \quad (gc \rightarrow ss\bar{c}), \\ \textcircled{10} \quad g\bar{d} \rightarrow \bar{u}s\bar{c} \quad (g\bar{s} \rightarrow \bar{c}d\bar{u}), \quad \textcircled{11} \quad g\bar{d} \rightarrow \bar{u}d\bar{u} \quad (g\bar{s} \rightarrow \bar{c}s\bar{c}). \end{aligned}$$

Processes with an initial-state gluon have diagrams with and without s -channel topologies, even if they are related by crossing to qq ($\bar{q}q$) subprocesses, which do not show these topologies. Figure 12 shows some examples for the subprocess $gu \rightarrow ds\bar{c}$.

Before discussing the NLO corrections, we remark that the $\mathcal{O}(\alpha_{\text{em}}^4 \alpha_s)$ matrix elements of the $pp \rightarrow W^+W^+jjj$ process, i.e. our LO, contain infrared divergences in regions of phase space in which one of the massless final-state particles becomes soft or collinear to another external massless particle⁹. An example would be the gluon's (g) momentum becoming soft or collinear to that of q_1 in any of the diagrams of Fig. 10. These divergences are not canceled by the KLN mechanism, which starts to act at NLO as described in Sec. 1.2.3. Therefore, a method is required in our calculation to prevent unphysical predictions as a consequence of these divergences. The details of this method will be discussed in Sec. 4.2.4.

3.1.1 One-Loop Corrections

The virtual QCD corrections, of order $\alpha_{\text{em}}^4 \alpha_s^2$, arise from the interference of LO diagrams with one-loop diagrams of the same subprocess. These diagrams are of order $g^4 g_s^3$, and contain loops with up to seven vertices (heptagon loops).

Figure 13 depicts one-loop diagrams in which the external W^+ bosons stem from a fermion line, similar to the top-left (LO) diagram in Fig. 10, and where there is no gluon exchange between upper and lower quark lines. These diagrams contain

⁹This is in contrast to the lowest order VBS processes possible at the LHC, i.e. $pp \rightarrow W^+W^+jj$ at $\mathcal{O}(\alpha_{\text{em}}^4)$, for which the matrix elements are finite.

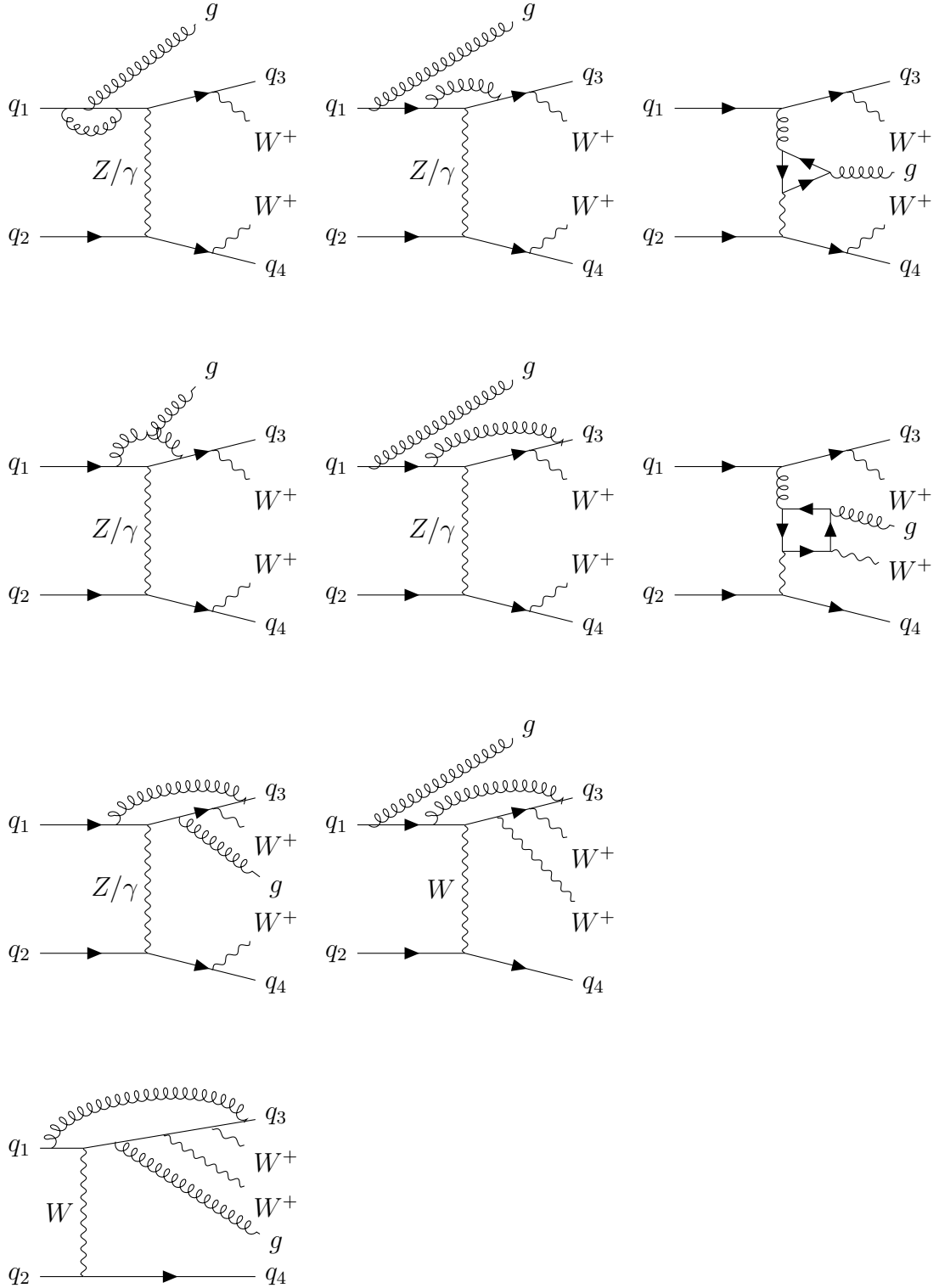


Figure 13: Exemplary one-loop Feynman diagrams of a qq -type subprocess without gluon exchange between the upper and lower quark lines. From top to bottom, the lines show triangle, box, pentagon and hexagon loops.

3.1 Electroweak Production of W^+W^+jjj at the LHC

loops with up to six vertices. Some of these loops contain only fermion lines (see Fig. 13 first and second lines, right), and cannot be constructed by only attaching gluon lines to LO diagrams.

Virtual diagrams with gluon exchange between upper and lower quark lines contain loops with at least four and up to seven vertices. Figure 14 shows some examples for a qq -type subprocess.

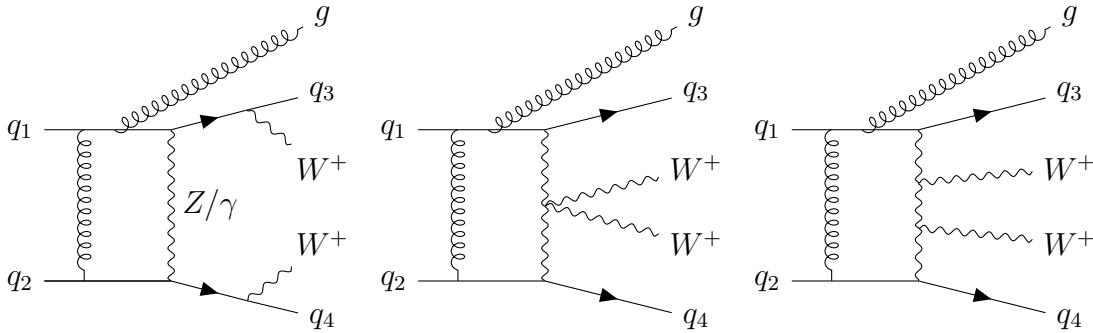


Figure 14: Exemplary one-loop Feynman diagrams of a qq -type subprocess with gluon exchange between fermion lines. From left to right: pentagon, hexagon and heptagon loops.

3.1.2 Real-Emission Corrections

The real-emission corrections, of order $\alpha_{\text{em}}^4 \alpha_s^2$, arise from diagrams of order $g^4 g_s^2$. There are four types of real subprocesses:

$$q_1 q_2 \rightarrow q_3 q_4 g g, \quad g q_1 \rightarrow q_2 q_3 q_4 g, \quad g g \rightarrow q_1 q_2 q_3 q_4 \quad \text{and} \quad q_1 q_2 \rightarrow q_3 q_4 q_5 q_6,$$

in the notation of Sec. 3.1. The first two types contain the same subprocesses as the corresponding LO types, with one more gluon in the final state. Accordingly, they contain 12 and 8 subprocesses, respectively. Their Feynman diagrams also inherit the resonant structure of the corresponding LO diagrams.

The third type, with initial state gg , is related by crossing to the first type and has the 3 subprocesses

$$g g \rightarrow d \bar{u} s \bar{c}, \quad g g \rightarrow d \bar{u} d \bar{u} \quad (g g \rightarrow s \bar{c} s \bar{c}).$$

The corresponding Feynman diagrams can have up to three resonant propagators, and some of them include a three-gluon vertex.

The fourth subprocess type has four quarks in the final state, and we will sometimes call it the four-quark type. It has 86 subprocesses, the largest number of all types. It also exhibits a wider variety of topologies in its Feynman diagrams, which contain three fermion lines. Generally, the real Feynman diagrams can have up to three s -channel electroweak boson propagators. In some diagrams, the two

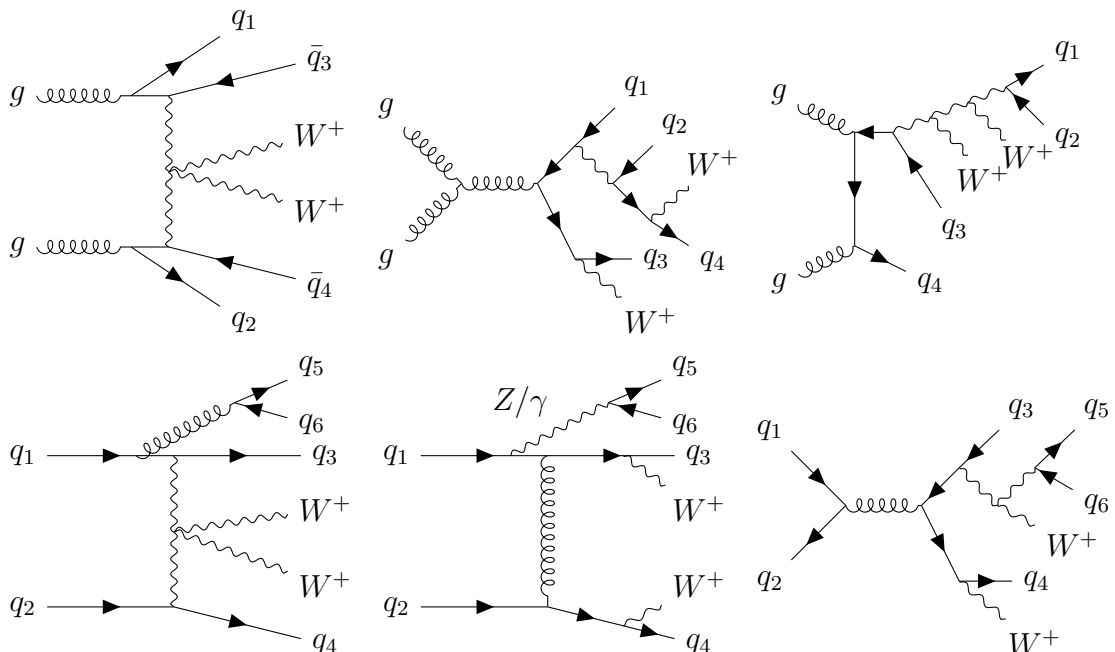


Figure 15: First row: Feynman diagrams of a real subprocess of the gg type with zero, one and three s -channel electroweak boson propagators, from left to right. Second row: four-quark real subprocess without (left, right) and with (center) gluon exchange between initial-state fermion lines.

fermion lines that are part of the initial state are joined by a gluon propagator. In such diagrams, a quark-antiquark pair necessarily originates from an s -channel electroweak boson propagator, since the gluon exchange already requires all available orders of the strong coupling. Some examples of Feynman diagrams of real gg and four-quark subprocesses are shown in Fig. 15.

Some four-quark subprocess contain IR divergences that are not cancelled by the virtual contributions that we take into account, nor by the initial-state collinear counterterms that correspond to the PDF renormalization (see Sec.2.1). This is because they are associated to processes with an external photon, which we do not consider. One example of this is the diagram at the center of the second row of Fig. 15, where the final-state quark-antiquark pair q_5q_6 can originate from a photon propagator. Since the photon is massless, this $\gamma^* \rightarrow q\bar{q}$ splitting is divergent in the limit of a collinear quark-antiquark configuration. We remark that these splittings appear exclusively in diagrams of real, four-quark subprocesses with gluon exchange between initial and final-state quark lines. As we will see in Sec. 3.2, such diagrams are not taken into account in our calculation.

Another example of a remaining singularity is given in Fig. 16. There, the quarks q_1 and q_3 can become collinear, causing the internal photon propagator to diverge. Such contributions are included in our calculation. The initial-state collinear singularity that they contain would typically be cancelled by the initial-

3.2 The Vector-Boson-Scattering Approximation

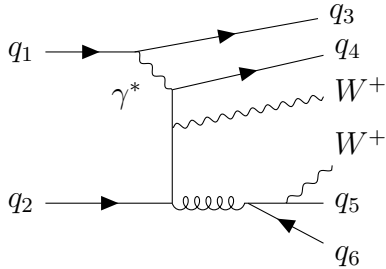


Figure 16: Feynman diagram of an all-quark real subprocess with a divergent $q \rightarrow q\gamma^*$ splitting.

state collinear counterterms (see Sec. 2.1), which are proportional to a Born matrix element of $\mathcal{O}(\alpha_{\text{em}}^3 \alpha_s^2)$ with an initial-state photon. To be consistent with our choice of neglecting photon-induced contributions, we instead regulate this $q \rightarrow q\gamma^*$ splitting by introducing a *technical cut* in our calculation that requires the photon virtuality to be finite. Specifically, we require that $(p_i - p_j)^2 > Q_{\gamma, \text{min}}^2$, where i and j denote initial- and final-state quarks respectively. This technical cut is applied only for the real all-quark subprocesses, since they are the only ones that can present the divergent splittings.

3.2 The Vector-Boson-Scattering Approximation

In general, the calculation of a certain process, defined by an initial and final state, implies that all contributions to at least a certain order of perturbation theory must be considered. In some cases, distinct subsets of contributions dominate the cross section in certain regions of phase space. In those cases, it can be sensible to compare only a subset of the contributions to experimental observations. If only a subset of the contributions for a process is taken into account for a calculation, that subset must be gauge invariant to obtain gauge-independent results.

The so-called Vector-Boson Scattering (VBS) or Vector-Boson Fusion (VBF) approximation has been used to simplify calculations of the hadronic production of $W^\pm W^\pm jj$, $ZZjj$ and $Hjj(j)$ in such a way [82, 83, 84, 85, 86]. In those processes, there are Feynman diagrams of qq -initiated subprocesses in which the quarks scatter off each other by the exchange of a space-like electroweak vector boson, and the exchanged electroweak boson can radiate a pair of electroweak bosons (VBS), see the last three diagrams in Fig. 10, or a Higgs boson (VBF). These diagrams have a distinct kinematic signature, i.e. they correspond to expressions that dominate certain regions of phase space. If this set of diagrams is extended to be gauge-invariant, then it can be used to define a subset of contributions that can be compared to observations. In [5], this approach is taken to *define* the VBS/VBF process as this subset of diagrams, as opposed to an initial and final state.

In this section, we define the VBS approximation as will be used in the present work and argue why it is sensible and gauge invariant. We begin by discussing

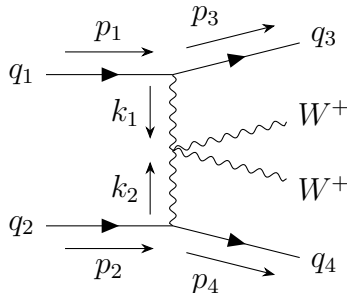


Figure 17: Characteristic Feynman diagram of Vector Boson Scattering with two jets.

the VBS signature following [5]. Afterwards, we discuss why certain contributions to W^+W^+jjj production are suppressed in the region in which the VBS signal is largest, and thus provide the arguments for neglecting these contributions. Then, we show why this approximation leads to a gauge-invariant result. The quality of the VBS approximation has been recently assessed in Ref. [28], where the relative difference with respect to the full calculation was found to be below 1.5% at the level of integrated cross sections¹⁰.

3.2.1 The VBS Signature

We first consider VBS at LO, that is, a subset of events of the hadronic production of W^+W^+jj at $\mathcal{O}(\alpha_{\text{em}}^4)$. Contributions from Feynman diagrams like the ones discussed in Sec. 3.2, where two vector bosons scatter off each other, dominate events in which the two final state jets, also called *tagging jets*, appear in the very forward regions of the detector, as we will see shortly. This is the characteristic signature of VBS.

Figure 17 depicts one VBS diagram with momenta labels. According to the Feynman rules in Eq. (1.3), the spin-averaged square of its amplitude \mathcal{A} is proportional to

$$|\mathcal{A}|^2 \propto \frac{A(p_1 \cdot p_2)(p_3 \cdot p_4) + B(p_1 \cdot p_4)(p_2 \cdot p_3)}{(k_1^2 - M_W^2)^2(k_2^2 - M_W^2)^2}, \quad (163)$$

where A and B are constant coefficients and $k_1 = p_1 - p_3$, $k_2 = p_2 - p_4$.

On the one side, the expression in Eq. (163) becomes large when its denominator is small. The squared momentum of the upper virtual boson is given by

$$k_1^2 = -2p_1 \cdot p_3 = -2E_1E_3(1 - \cos\theta_{1,3}) \leq 0,$$

where $\theta_{1,3} = \angle(\vec{p}_1, \vec{p}_3)$, and similarly for k_2^2 . Thus the smallest possible denominator in Eq. (163) is reached for $k_{1/2}^2 \approx 0$. For a given incoming energy E_1 , this is the case

¹⁰In Ref. [28], the full calculation comprised contributions to W^+W^+jj production at the LHC of all possible orders, as well as leptonic decay products of the W^+ bosons. The employed approximation was a combination of the VBS approximation and the so-called double-pole approximation, which neglects contributions of far off-shell W^+ bosons and is thus closer to our calculation.

3.2 The Vector-Boson-Scattering Approximation

when either the scattering angle or E_3 is small (or both). We shall assume the first case, the reason why will become clear further below.

On the other side, the expression Eq. (163) is large if the numerator is large. For a given squared partonic energy $s = (p_1 + p_2)^2 = 2 p_1 \cdot p_2$, the term proportional to A in (163) is proportional to the squared invariant mass $M^2(q_3, q_4) = 2 p_3 \cdot p_4$ of the outgoing quarks. This quantity is large for large E_3 and E_4 , which motivates the assumption above. Furthermore, large E_3 and E_4 means that the energy carried by the virtual bosons is not much larger than the $2M_W^2$ necessary to create the rest of the final state. In this scenario, it holds

$$p_1 \cdot p_4 \approx p_1 \cdot p_2 \quad \text{and} \quad p_2 \cdot p_3 \approx p_4 \cdot p_3$$

so that the denominator of Eq. (163) as a whole behaves as we just described for the part proportional to A , and we can approximately write the expression in Eq. (163) as [87]

$$\frac{(A + B)(p_1 \cdot p_2)(p_3 \cdot p_4)}{4(E_1 E_3(1 - \cos \theta_{1,3}) + M_W^2)^2(E_2 E_4(1 - \cos \theta_{2,4}) + M_W^2)^2}.$$

All in all, we expect the VBS contributions to be largest in regions of phase space with two hard, forward jets with a large total invariant mass. Other types of diagrams that contribute to W^+W^+jj production lack such an enhancement in this region.

Until now, our discussion of the VBS signature has focused on VBS with two jets. The process we study in this work contains one more jet in the final state at LO, but the above considerations with respect to the VBS signature remain valid. Consider, for example, the contribution of the diagram in Fig. 17 with the additional emission of a gluon of momentum p_5 by the upper quark line. If we picture the gluon emission after the emission of the virtual boson, then the additional quark propagator provides a factor

$$((p_3 + p_5)^2)^2 = E_3^2 E_5^2 (1 - \cos \theta_{3,5})^2$$

to the spin-averaged squared matrix element, which enhances the contribution for small E_5 and $\theta_{3,5}$. Such soft/collinear emissions do not significantly affect the kinematic arguments made before for the two-jet final state, so we expect a similar signature of VBS contributions in the three-jet case.

We now turn to the contributions which are suppressed in the regions of phase space that correspond to the signature we just described.

3.2.2 Electroweak Propagators in the s -Channel

A class of diagrams that is neglected in the VBS approximation is composed of LO and NLO diagrams with electroweak propagators in the s -channel. The contributions of diagrams where the final-state quarks are the decay products of a vector boson,

cf. the right diagram in Fig. 12, are expected to be the largest for values of the two-jet invariant mass close to the mass of the parent vector boson. There are also other s -channel diagrams where a quark-antiquark pair originates from a resonant electroweak propagator and then either the quark or the antiquark emit a final state W^+ boson, cf. the center diagram in Fig. 12. These contributions are largest for even lower values of the two-jet invariant mass, as can be seen from the following argument. Consider the kinematics of the center diagram in Fig. 12. The Z -boson propagator contributes with a factor

$$[p_Z^2 - M_Z^2]^{-2}, \quad (164)$$

where p_Z stands for the momentum of the Z boson and M_Z for its mass. Denoting the momenta of the final-state quarks with a subindex of the corresponding flavor and the momentum of the lower W^+ boson by p_W , momentum conservation yields

$$\begin{aligned} p_Z^2 &= (p_c + p_s + p_W)^2 \\ &= M(p_c, p_s)^2 + M_W^2 + 2p_W \cdot (p_c + p_s) \\ &= 2|\vec{p}_c||\vec{p}_s|(1 - \cos\theta_{cs}) + M_W^2 + 2M_W(|\vec{p}_c| + |\vec{p}_s|), \end{aligned} \quad (165)$$

where we have taken all momenta as flowing from left to right in the diagram. In the last step, we have chosen the center-of-mass system of the lower W^+ boson and we have written the invariant mass of the quark pair in terms of the absolute-value of its three momenta and the angle θ_{cs} between these. We can plug Eq. (165) in the expression from Eq. (164) and obtain

$$\left[-(M_Z^2 - M_W^2) + 2|\vec{p}_c||\vec{p}_s|(1 - \cos\theta_{cs}) + 2M_W(|\vec{p}_c| + |\vec{p}_s|)\right]^{-2}, \quad (166)$$

which is symmetric w.r.t. the quark energies $|\vec{p}_i|$. The expression in Eq. (166) is maximized by setting one quark energy to zero and the other to

$$|\vec{p}| = \frac{M_Z^2 - M_W^2}{2M_W} \approx 12\text{GeV}.$$

For $|\vec{p}_c| = |\vec{p}_s| =: |\vec{p}|$ and $\cos\theta_{cs} < 1$, the expression in Eq. (166) is maximized by

$$|\vec{p}| = \frac{1}{1 - \cos\theta_{cs}} \left[\sqrt{\frac{M_Z^2 + M_W^2}{2} - \frac{M_Z^2 - M_W^2}{2} \cos\theta_{cs}} - M_W \right] \leq \frac{M_Z^2 - M_W^2}{4M_W} \approx 6\text{GeV}.$$

Such small typical values of the quark energies are only compatible with a small invariant mass of the jet pair, as opposed to the large values of the VBS signature. Thus, contributions of s -channel diagrams are kinematically distinct from VBS contributions, and can be disentangled by implementing analysis cuts that require a high invariant mass of the hardest jet pair.

3.2 The Vector-Boson-Scattering Approximation

3.2.3 Diagrams with Gluon Exchange

As we have shown in previous sections, diagrams in which a gluon is exchanged between external fermion lines contribute to the virtual and real corrections of W^+W^+jjj production at order $\alpha_{\text{em}}^4\alpha_s$. As we will see now, these contributions are *color suppressed* with respect to those of diagrams without gluon exchange and are neglected in the VBS approximation. This means that the color parts of the squared contribution, which result from the color factors of the matrix elements after squaring and summing over colors, are proportional to a lower power in the number of colors N_C .

Figures 18 and 19 show some virtual contributions, i.e. the interference of a one-loop and a LO diagram, and the color factors that these are proportional to. Virtual contributions that contain gluon-exchange diagrams are suppressed by a power of $(N_C - N_C^{-1})$ with respect to those that do not (Fig. 18). Other interferences vanish due to the tracelessness of the $N_C^2 - 1$ Gell-Man matrices $\{\lambda^a\}$, namely those where only one gluon is radiated from a quark line (Fig. 19). These arguments carry over to virtual contributions of qg -type channels with no s -channel electroweak boson propagator. To determine the color factors, we have considered the Feynman rule of Eq. (89) for the quark-gluon vertex, summed over colors and used the relations in Eqs. (53) and (52).

The contributions of one-loop diagrams with gluon exchange that we neglect contain IR divergences which, according to the KLN theorem [47, 48], would be canceled by real-emission contributions in a full NLO calculation. Therefore, care needs to be taken in the VBS approximation to not include the would-be remainders of the IR subtraction. This can be accomplished by excluding the interferences of real-emission diagrams of type $qq \rightarrow qqgg$ in which each gluon is emitted by a different quark line in each diagram. This procedure is discussed in [82] for VBF with three jets, where it is argued that not only do such real-emission contributions need to be neglected for consistency reasons, but they are also kinematically suppressed.

At LO, no gluon exchange between external fermion lines can take place. On the other hand, the QCD-induced contributions to W^+W^+jjj production, mentioned at the top of this section, do contain diagrams with gluon exchange. Therefore, the arguments about color suppression presented above also apply to the interferences of VBS (g^4g_s) with QCD-induced ($g^2g_s^3$) diagrams. This adds to the justification of not taking the QCD-induced process into account.

Diagrams that contribute to the real-emission corrections can contain gluon exchange only if they belong to subprocesses of the four-quark type. Furthermore, these diagrams contain s -channel electroweak boson propagators, which, as discussed before, leads to a signature that is different to that of VBS and are safe to be ignored in the regions of phase space where the VBS signature is largest.

3 VBS and the $pp \rightarrow W^+W^+jjj$ Process

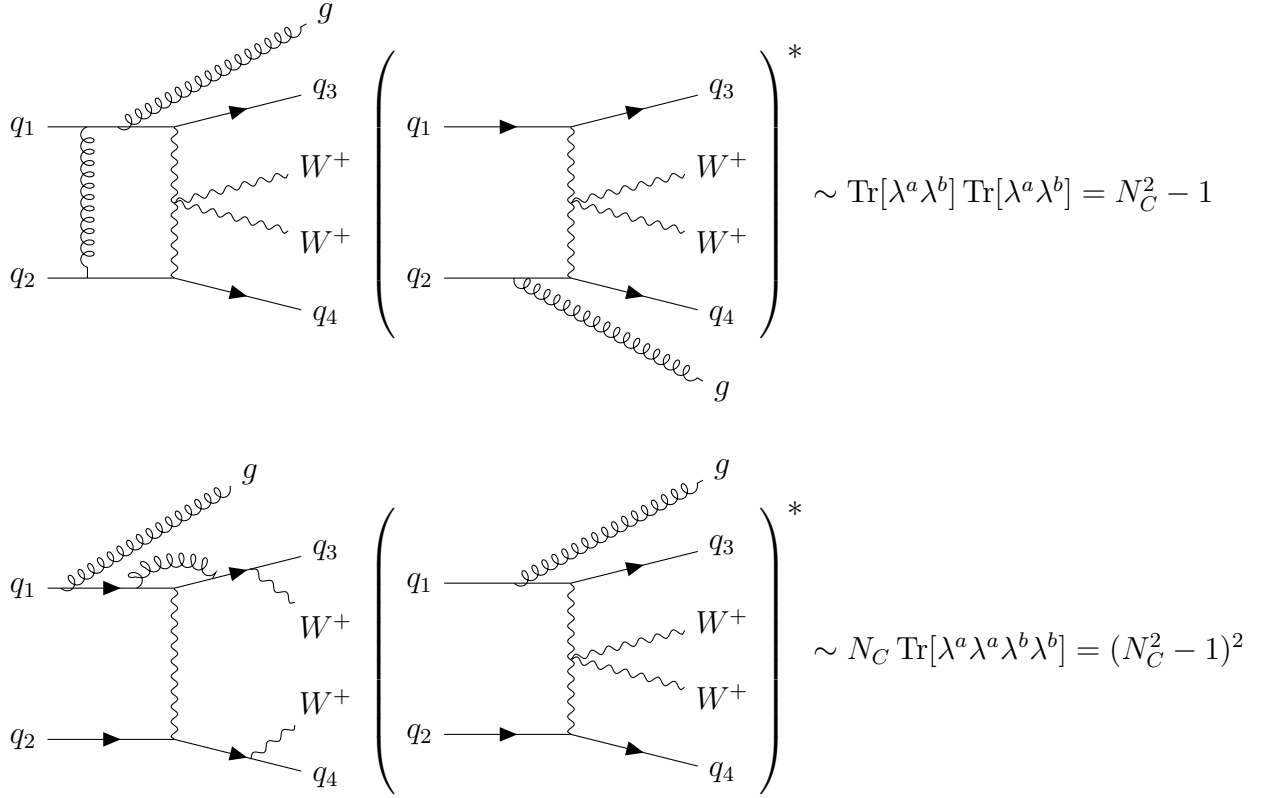


Figure 18: Exemplary interferences of Feynman diagrams alongside the color part of the contributions that they correspond to. In each row, the interference is diagrammatically represented as the product of a Feynman diagram (left) times a complex-conjugated Feynman diagram. The first row contains a one-loop diagrams with gluon exchange, which is neglected in the VBS approximation. The second row contains an interference that is taken into account in the VBS approximation. The contribution of the first row is suppressed by a power of $(N_C - N_C^{-1})$ with respect to that of the second one.

3.2 The Vector-Boson-Scattering Approximation

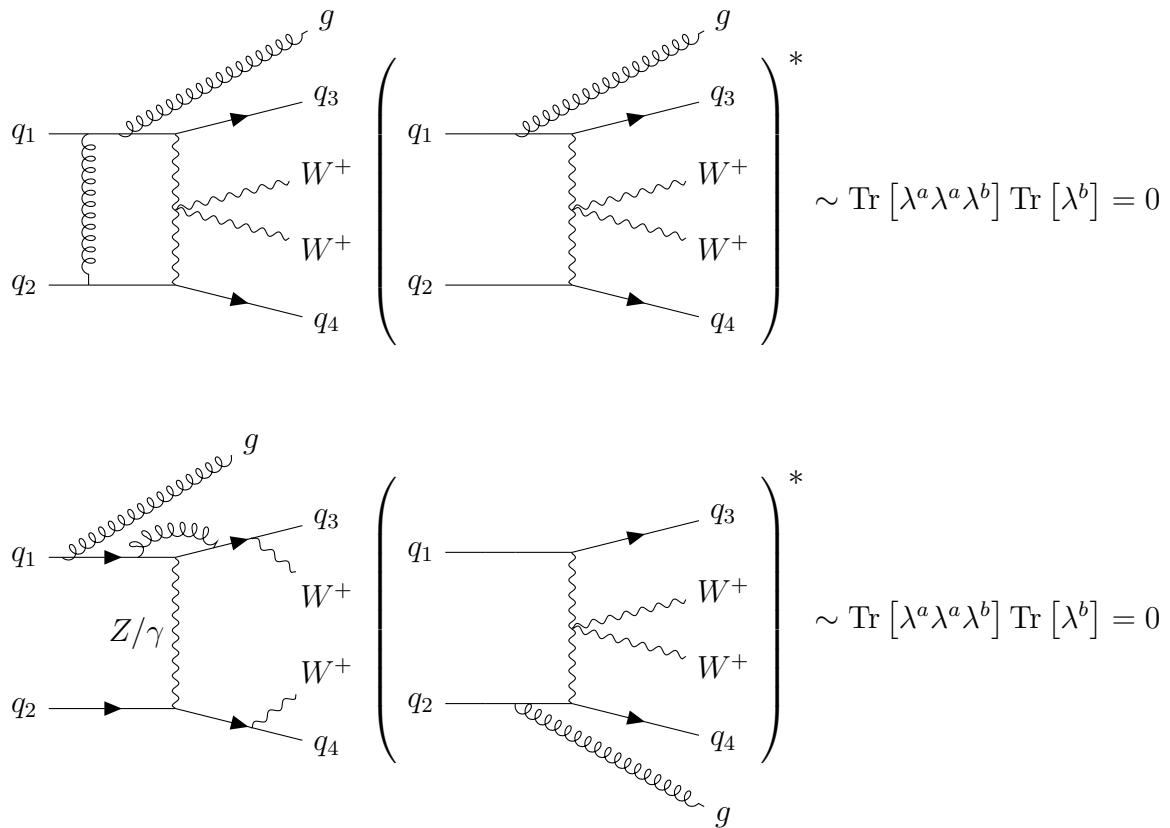


Figure 19: Schematic representation of exemplary vanishing interferences of Feynman diagrams and the color part of the contributions that they correspond to. Loop diagram with (upper row) and without (lower row) gluon exchange. These interferences and all others where only one gluon is attached to a quark line vanish due to the tracelessness of the Gell-Mann matrices.

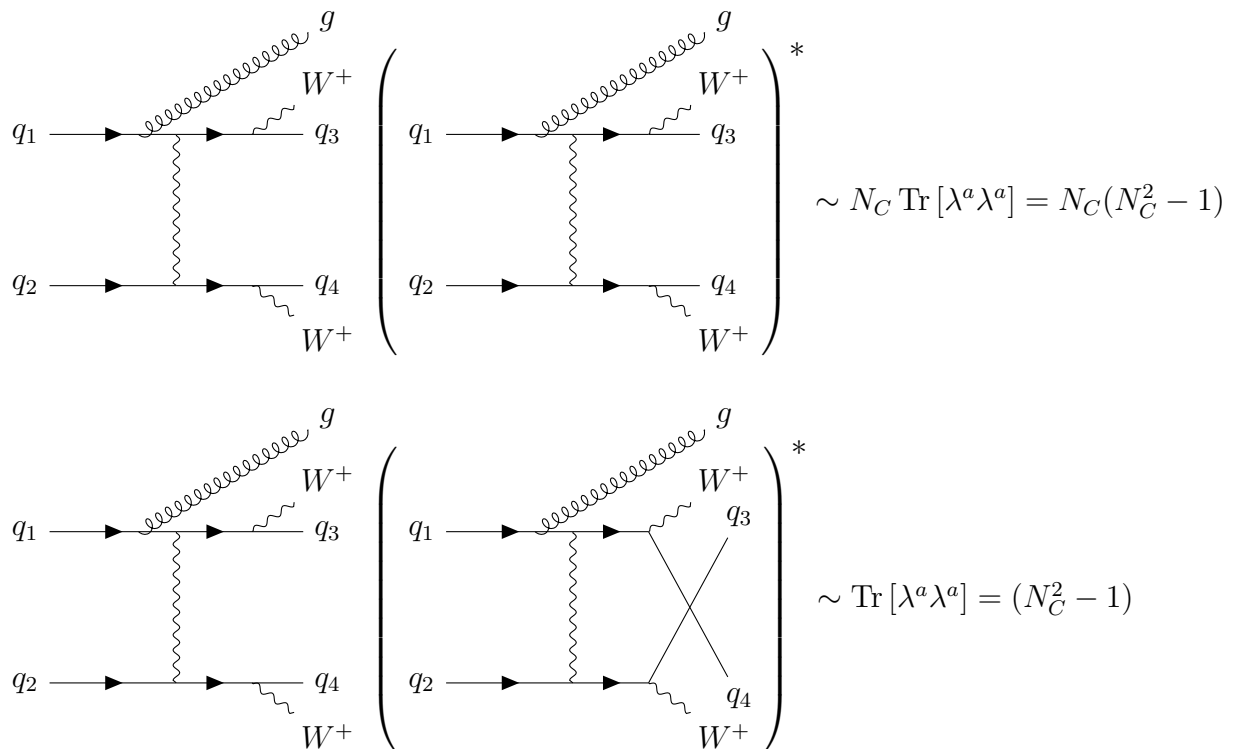


Figure 20: Schematic representation of exemplary interferences of Feynman diagrams and the color part of the contributions that they correspond to. First row: t -channel diagram squared. Second row: interference of t and u -channel diagrams, only possible if $q_3 = q_2$. The t - u interference is suppressed by N_C^{-1} with respect to the squared u -channel diagram.

3.2.4 Identical-Particle Effects

One more kind of contributions that is neglected in the VBS approximation is the interference between t and u -channels, which can occur when the initial or final state include identical quarks. Figure 20 shows the Feynman diagrams of one such contribution alongside its color part, together with a squared t -channel diagram for comparison. The interference contribution is suppressed by a factor N_C^{-1} . The numerical studies of VBF with two jets in Ref. [88] show that t/u -channel interferences can be safely neglected when requiring two jets, each with transverse momentum $p_{T,j}$ and rapidity y_j fulfilling

$$p_{T,j} > 20\text{GeV}, \quad |y_j| < 4.5, \quad (167)$$

as well as being well-separated and in opposite regions of the detector

$$|y_{j_1} - y_{j_2}| > 4, \quad y_{j_1} \cdot y_{j_2} < 0, \quad (168)$$

where j_1 and j_2 denote the two jets, ordered by transverse momentum.

3.2 The Vector-Boson-Scattering Approximation

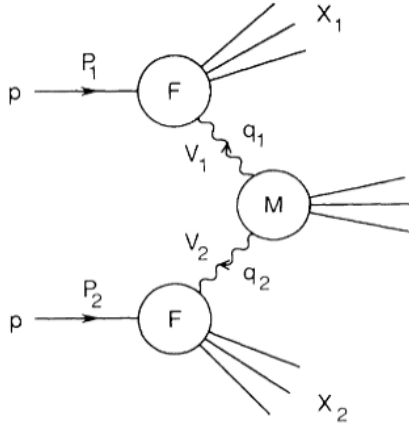


Figure 21: Schematic representation of the structure-function approach to VBS, taken from [90]. The hadronic part of the reaction is parametrized by the structure functions F , while the scattering of the electroweak bosons is described by the matrix element M .

3.2.5 The Structure-Function Approach to Vector Boson Scattering

The *structure-function approach* was formulated for hadronic Higgs boson production via Vector Boson Fusion in [89] and more generally for Vector Boson Scattering in [90]. At the lowest order, that is, with two jets in the final state, these are purely electroweak processes. This calculational approach is based on the observation that the NLO QCD corrections of these processes, of order α_s , correspond to Feynman diagrams in which no color exchange occurs between the quark lines that are involved. The interference of one-loop diagrams in which a gluon is exchanged between quark lines with LO diagrams vanishes after a sum over colors, effectively due to the tracelessness of the Gell-Mann matrices. Therefore, the only diagrams that contribute to these corrections correspond to QCD corrections of the electroweak qqV vertices, where V is the electroweak boson emitted by a quark line. For this reason, the calculation of VBS to NLO in QCD can be done in terms of structure functions that parametrize the hadronic tensor. The corrections factorize into the corrections to the structure functions and the corrections to the vector-boson-scattering subprocess. This is analogous to the situation of two deep-inelastic scattering (DIS) processes in which the photons are replaced by massive vector bosons that then fuse or scatter, see Fig. 21. At order α_s^2 , which is the order of the NLO corrections to VBS with three jets, the exact factorization is not given anymore. As it turns out, the contributions that are neglected by employing the structure-function approach beyond $\mathcal{O}(\alpha_s)$ are precisely those for which we have shown the kinematic and color suppression in the subsections above.

The structure-function approach is equivalent to the following construction: consider two separate, independent copies of QCD, each with their own set of colored particles which do not interact with particles of the other set. Now, compose the

initial state of any partonic subprocess by taking one particle from each copy of QCD and construct all possible Feynman diagrams. Since the resulting diagrams are all possible diagrams of our gauge independent theory, they form a gauge invariant set.

In our case of W^+W^+jjj production, the construction above results in the following. For LO qq -type subprocesses only diagrams occur in which the initial-state particles do not belong to the same fermion line, and in which the upper and lower fermion lines must be connected by electroweak bosons, which needs at least two electroweak couplings. In consequence, no electroweak boson s -channel propagators can appear, since the two remaining electroweak couplings are needed for the two external W^+ bosons.

For LO gq -type subprocesses, this means that the initial-state gluon never couples to the fermion line to which the initial-state quark belongs. It rather creates a quark-antiquark pair, another fermion line, which couples to the first fermion line via electroweak interaction. Again, only diagrams without s -channel electroweak boson propagators arise.

The one-loop diagrams that emerge do not contain s -channels by the same logic, and also lack gluon exchange between fermion lines: a gluon of the first copy of QCD can not couple to the second one.

The same applies for real-emission diagrams of subprocesses of types $qq \rightarrow qqgg$ and $gq \rightarrow qqgq$. The interference contributions of $qq \rightarrow qqgg$ diagrams that need to be left out for consistency, as described in Sec. 3.2.3, do not arise in this construction.

Diagrams of the type $gg \rightarrow qqqq$ contain s -channel electroweak propagators only if there is color exchange between the initial state particles, which is forbidden by construction. The two incoming gluons must end in some quark internal line(s), which uses up the two available strong coupling powers. If the gluons do not each couple to a different quark line, then the other quark line must originate from an electroweak boson, see upper row of Fig. 15.

In diagrams of the $qq \rightarrow qqqq$ type, the forbidden color flow between the lines of the incoming quarks coincides with the presence of s -channel electroweak boson propagators by a similar logic, see the second row of Fig. 15. If one of the final-state quark pairs originates from a gluon propagator, which must itself be attached to one of the other two quark lines, then no powers of the strong coupling remain for a gluon exchange between the initial state quarks. Diagrams in which the initial-state quarks belong to the same fermion line are forbidden by construction. Furthermore, no diagrams with splittings of the kind $\gamma^* \rightarrow q\bar{q}$ are included, as discussed in Sec. 3.1.2

We define the VBS approximation, as we employ it in this work, as the calculation of hadronic W^+W^+jjj production *without* the contributions discussed in Sec. 3.2.2 through 3.2.4, which are kinematically and/or color suppressed. As we have seen, the remaining contributions can be constructed by adopting the structure-function approach, yielding a gauge-invariant set. We remark that no subprocesses induced by a pair of bottom-antibottom quarks arise in our approximation as a

3.2 *The Vector-Boson-Scattering Approximation*

consequence of the exclusion of EW propagators in the s -channel.

4 Implementation

In this Section, we discuss our implementation of the VBS process. We begin by discussing the framework in which the calculation is implemented, the computer program POWHEG-BOX. We then give details about the implementation itself and the checks that were performed on it.

4.1 POWHEG BOX

The FORTRAN computer code POWHEG-BOX is a parton-level *Monte Carlo event generator* that implements the POWHEG method discussed in Sec. 2.2 and generates events with NLO precision that can be matched to a PS program. It was first published in [91], and has since been upgraded to a version 2 [92] and later a RES version [72], which is the latest one and also the one we employ in this work. The code is constructed in a general way, so that developers can implement processes by providing only process-specific ingredients of a calculation. These are:

- The flavor structures of all partonic subprocesses that contribute to the hadronic process at Born and real level.
- For the first and second versions of the code, a parametrization of the Born phase-space that maps uniformly distributed variables X_{born} in the unit interval to a set of momenta of a Born configuration was necessary. In the RES version, the phase space is automatically generated.
- The Born, virtual and real contributions \mathcal{B} , \mathcal{V}_{fin} and \mathcal{R} introduced in Sec. 2.
- The color-correlated Born amplitudes \mathcal{B}_{ij} from Sec. 2, as well as the *spin-correlated Born amplitudes* $\mathcal{B}_{\mu\nu}$, which will be introduced further below.

In the initialization phase, POWHEG-BOX constructs all possible singular regions α_r that can occur due to real emission off each flavor structure f_b . This is done by taking each real flavor structure and checking if it can be realized by the branching of an existing f_b , in which case that f_b is called an *underlying Born structure* of the real flavor structure. This generates a list of regions $\{\alpha_r|f_b\}$ of each underlying Born, which can originate from different branchings (and different real structures). This identification of all possible singular regions is the base for the isolation of divergences that is necessary in the FKS scheme, realized by the \mathcal{S} -functions (cf. Sec. 2.1). Thus, summig over the contributions of all flavor structures, Eq. (154) becomes

$$\bar{B}(\Phi_n) = \sum_{f_b} \bar{B}^{f_b}(\Phi_n) \quad (169)$$

4.1 POWHEG BOX

where

$$\begin{aligned} \bar{B}^{f_b}(\Phi_n) &= [B(\Phi_n) + V(\Phi_n)]_{f_b} + \sum_{\alpha_r \in \{\alpha_r|f_b\}} \int \left[d\Phi_{\text{rad}} \hat{R}(\Phi_{n+1}) \right]_{\alpha_r}^{\bar{\Phi}_n^{\alpha_r} = \Phi_n} \\ &+ \sum_{\alpha_\oplus \in \{\alpha_\oplus|f_b\}} \int \frac{dz}{z} G_\oplus^{\alpha_\oplus}(\Phi_{n,\oplus}) + \sum_{\alpha_\ominus \in \{\alpha_\ominus|f_b\}} \int \frac{dz}{z} G_\ominus^{\alpha_\ominus}(\Phi_{n,\ominus}). \end{aligned} \quad (170)$$

In Eq. (170), we have adopted the *context notation* of references [34, 91], in which the quantities within a square bracket that has a subindex are all relative to that subindex. Furthermore, the square bracket under the first integral means that the integration is carried out over the one-particle radiation phase space that describes the branching of the current α_r , keeping the underlying Born variables $\bar{\Phi}_n^{\alpha_r}$ fixed and equal to Φ_n . The regions α_\oplus and α_\ominus correspond to initial-state radiation. There might also be real flavor structures which can not lead to a divergence, and thus are called *regular*.

The generation of events in POWHEG-BOX is subdivided into 4 stages, which occur after the initialization phase mentioned above. In the first stage, importance-sampling grids are set up to make the integration of the FO cross section more efficient. Specifically, the function

$$\tilde{B}(\Phi_n, X_{\text{rad}}) = \sum_{f_b} \tilde{B}^{f_b}(\Phi_n, X_{\text{rad}}), \quad (171)$$

with

$$\begin{aligned} \tilde{B}^{f_b}(\Phi_n, X_{\text{rad}}) &= [B(\Phi_n) + V(\Phi_n)]_{f_b} + \sum_{\alpha_r \in \{\alpha_r|f_b\}} \left[\left[\frac{\partial \Phi_{\text{rad}}}{\partial X_{\text{rad}}} \right] \hat{R}(\Phi_{n+1}) \right]_{\alpha_r}^{\bar{\Phi}_n^{\alpha_r} = \Phi_n} \\ &+ \sum_{\alpha_\oplus \in \{\alpha_\oplus|f_b\}} \frac{1}{z} \left| \frac{\partial z}{\partial X_{\text{rad}}^{(1)}} \right| G_\oplus^{\alpha_\oplus}(\Phi_{n,\oplus}) + \sum_{\alpha_\ominus \in \{\alpha_\ominus|f_b\}} \frac{1}{z} \left| \frac{\partial z}{\partial X_{\text{rad}}^{(1)}} \right| G_\ominus^{\alpha_\ominus}(\Phi_{n,\ominus}) \end{aligned} \quad (172)$$

is sampled to create grids that are denser where the function is larger. In Eq. (172), the radiation phase space Φ_{rad} as well as z has been parametrized with three further variables

$$X_{\text{rad}} = \left\{ X_{\text{rad}}^{(1)}, X_{\text{rad}}^{(2)}, X_{\text{rad}}^{(3)} \right\}, \quad (173)$$

each in the unit interval, and Φ_n is implicitly given by the integration variables X_{born} and an appropriate Jacobian. If regular structures exist, a separate grid is constructed for them. Once the grids are computed, they can be visualized to check their quality, which will greatly impact the next stages of the program. The first stage can be iterated several times to achieve better grids.

In the second stage, \tilde{B} is integrated according to the grids generated previously, as well as any regular contributions that might exist. The value of the total cross

section that results will be used to give the events, generated at a later stage, their weight. In stage 2, also an upper bounding function of the integrand is generated. Optionally, the user can choose to generate differential distributions during this stage. The corresponding observables must be constructed in a user-defined analysis, but routines to generate the histograms are provided by the program.

In the third stage, the normalization of the upper bounding function for the generation of radiation is calculated. This normalization is necessary for the *hit-and-miss* or *accept-reject* procedure that is performed in the next stage.

Finally, the events are generated in the fourth stage. For each event, a phase-space point and a flavor structure are generated according to the function \bar{B} . Then, for each singular region α_r , a Sudakov form factor is computed and a transverse momentum p_T is generated according to it as a function of the radiation phase space. Then, the transverse momentum with the highest value is selected together with the corresponding α_r . If the selected value fulfills $p_T > p_T^{\min}$, where p_T^{\min} is the resolution threshold from Sec. 2.3, the radiation phase space is accepted and the event is saved. Otherwise, no radiation is generated. The events, which constitute the output of the last stage, are given out in the *Les Houches Event File* (LHEF) format [93, 94], which can be read by a PS program for further treatment.

4.2 Process-Specific Parts

4.2.1 Flavor Structures

The Born and real flavor structures of the VBS process, which have been discussed in Sec. 3, are not hard-coded but generated at the initialization stage. This is done in the routines `init_born` and `init_processes` by iterating over all possible flavor labels¹¹ and accepting those that respect charge and fermion-number conservation. Here, the assumption of a diagonal CKM matrix is taken into account. The list of flavor structures must include permutations of the initial state if it is not composed of identical particles. As for the final state, it must respect the following ordering: first, particles without color charge should be listed, then come the massive quarks and finally massless quarks and gluons. In our case, this means that the third and fourth entries of f_b are W^+ bosons. The rest of the labels are as given in Sec. 3, with the first two entries for the initial state and the entries after the fourth for the rest of the final state. POWHEG-BOX automatically checks that no flavor structure is defined twice according to these definitions. For calculations performed with this implementation, we assume a *perfect bottom-jet tagging and veto*, i.e. that jets stemming from bottom quarks can always be experimentally identified and excluded. Since our VBS approximation implicitly excludes a bottom-antibottom pair in the initial state, our calculation does not include flavor structures with any bottom quarks.

¹¹For the fermion labels, POWHEG-BOX employs the *Monte Carlo numbering scheme*, which can be found in [52], with the exception of the use of 0 instead of 21 to denote gluons.

4.2 Process-Specific Parts

After the flavor structures are generated, a second set of labels, called *tags*, is created. The tags are non-physical, internal labels that prevent the mechanism that finds singular regions from arriving at undesired regions. In practice, the tags correspond to the fermion lines of a Feynman diagram. Particles that belong to the same fermion line carry the same tag. Then, for example, if two fermions of a real flavor structure, say a quark-antiquark pair, carry different tags, the region that corresponds to the splitting $g \rightarrow q\bar{q}$ is not found, even if a compatible Born flavor structure exists.

In the RES version of POWHEG-BOX, eventual resonances present in matrix elements, i.e. massive propagators in the s -channel, are taken into account as additional information to improve the subtraction method. This functionality requires that each flavor structure is further supplemented by its *resonant histories*. For each *bare* flavor structure, i.e. a list of the flavor labels of the initial and final state, a new *resonant* flavor structure is constructed for each possible set of intermediate resonances. Thereby, the flavor labels of the resonances are listed in the resonant flavor structure between the initial and final state. Furthermore, all possible *associations* must be provided. These are a further set of labels that indicates which final-state particles are the decay products of which resonances. Altogether, a full flavor structure consists of four one-dimensional arrays (including the tags), with a length that depends on the particular number of intermediate resonances.

POWHEG-BOX includes the general routines `find_born_resonances` and `find_real_resonances` to construct all these arrays. In our implementation of the VBS process, the machinery that is necessary to include resonances is not employed, since we have explicitly excluded all resonances in our approximation. Nevertheless, it is our intention to extend our implementation to an exact calculation of the $pp \rightarrow W^+W^+jjj$ process in further work. For this case, the general routines `find_born_resonances` and `find_real_resonances` were not able to generate the intended result, so we have developed our own version of them, tailored to the $pp \rightarrow W^+W^+jjj$ process.

4.2.2 Matrix Elements

The matrix elements we employ to build the tree-level contributions were generated using the computer code `MadGraph5_aMC@NLO` [95] in standalone mode, in its version 2.9.15¹². In this program, the matrix elements are generated in a diagrammatic way, and the user can specify which diagrams are taken into account to a certain extent¹³. This is particularly useful for the purposes of the VBS implementation, since this

¹²POWHEG-BOX includes a part of the external code `MadGraph4` [96, 97] that is used to generate tree level matrix elements. Because of limitations in the multiplicity of the processes it can handle and in order to have a consistent framework for tree- and loop-level contributions, we generated instead these matrix elements using `MadGraph5_aMC@NLO`.

¹³We remark that the generation of matrix elements is only one of the many functions of this program. In full, it can carry out NLO computations and match them to a PS program with a method different from POWHEG, called MC@NLO.

allows us to exclude all diagrams with electroweak bosons in the s -channel by using the `$$` notation of `MadGraph5_aMC@NLO`.

The matrix-element routines that are generated by `MadGraph5_aMC@NLO` are mainly built to return the spin- and color-averaged square matrix elements, as they are needed for the computation of a LO cross section. This is done in a series of intermediate steps. The expression for each Feynman diagram is first constructed using so-called *helicity amplitudes*, which are provided as FORTRAN routines by the library `HELAS` [98] and encode the polarization- and kinematic-dependence of the amplitude. These are decomposed using the color-flow formalism [99, 100] and organized as color factors and color subamplitudes (see the end of Sec. 1.3.4) that each correspond to a distinct *color flow*.

For each partonic subprocess of $pp \rightarrow W^+W^+jjj$ at LO, there are at most two non-vanishing color flows, and each one corresponds to the external gluon (see Sec. 3.1) being attached to either of the two quark lines. Thanks to this setup, we can extract the color subamplitudes necessary to build \mathcal{B}_{ij} according to Eq. (140) under consideration of our VBS approximation, which neglects color flows in which a gluon is exchanged between different quark lines.

Similarly, we can build the spin-correlated Born amplitudes

$$\mathcal{B}_j^{\mu\nu} = N_{sc} \sum_{\{i\}, s_j, s'_j} \mathcal{M}(\{i\}, s_j) \mathcal{M}^\dagger(\{i\}, s'_j) (\epsilon_{s_j}^\mu)^* \epsilon_{s'_j}^\nu, \quad (174)$$

which are one 4×4 matrix per external particle j , and are only non-zero if j is a massless vector boson. In Eq. (174), $\mathcal{M}(\{i\}, s_j)$ is the Born amplitude, $\{i\}$ are all remaining spins and colors of the external particles, and s_j represents the spin of the j -th particle. As in Eq. (140), N_{sc} is the appropriate normalization factor that accounts for color and spin degrees of freedom as well as for identical particles. The $\epsilon_{s_j}^\mu$ are polarization vectors, normalized as

$$\sum_{\mu, \nu} g_{\mu\nu} (\epsilon_{s_j}^\mu)^* \epsilon_{s'_j}^\nu = -\delta_{s_j s'_j}. \quad (175)$$

`POWHEG-BOX` has built-in checks for the correctness of \mathcal{B}_{ij} and $\mathcal{B}_{\mu\nu}$, which must fulfill

$$\sum_{i, i \neq j} \mathcal{B}_{ij} = C_{f_j} \mathcal{B}, \quad (176)$$

where i runs over all colored particles entering or exiting the process, $C_{f_j} = 4/3$ for quarks and $C_{f_j} = 3$ for gluons, and

$$\sum_{\mu, \nu} g_{\mu\nu} \mathcal{B}_j^{\mu\nu} = -\mathcal{B}. \quad (177)$$

Both \mathcal{B}_{ij} and $\mathcal{B}_{\mu\nu}$ are used to construct analytic approximations to the real contributions in the singular regions, which ultimately enter the calculation of \hat{R} in

4.2 Process-Specific Parts

the FKS subtraction method. A further test of the correlated amplitudes consists in numerically checking that the approximations built with them actually coincide with the matrix elements in the appropriate soft and/or collinear limits. Also this check is implemented in POWHEG-BOX, and we have used it to test our routines.

The virtual corrections were generated using the code `MadLoop5` [101, 102], which is delivered as part of `MadGraph5_aMC@NLO`. As for the tree-level contributions, this program allows the exclusion of electroweak propagators in the s -channel using the `$$` command. `MadLoop5` includes interfaces to several other programs that handle the tensor integral reduction and the computation of scalar integrals, cf. Sec. 1.2.2, from which the user can choose. We have opted for the codes `COLLIER` [103] and `CutTools` [104] for this task. The latter is used as a backup in case `MadLoop5` detects an unstable result from the first one.

4.2.3 Channel Mapping

To implement the exclusion of identical particles, which is part of our VBS approximation, only matrix elements of subchannels that involve quark lines of different generations are called, which we call *primary*. This strategy requires a mapping from the complete set of flavor structures onto the set of flavor structures of the primary subchannels. The principle behind this mapping is to identify the fermion lines of the matrix elements that contribute to a general flavor structure and then assign each of those lines quark labels of the same kind but a different family. Thus, for example, we map

$$(u_1 \bar{d}_2 \rightarrow d_1 \bar{u}_2 g) \mapsto (u_1 \bar{s}_2 \rightarrow d_1 \bar{c}_2 g),$$

where we have used subscripts as labels for each fermion line. The mapping is well defined because we exclude electroweak bosons in the s -channel, so that an initial state like $u\bar{d}$ can not annihilate, i.e. the tags $(u_1 \bar{d}_1 \rightarrow d_2 \bar{u}_2 g)$ cannot be realized. Rather, the u and the \bar{d} each belong to a fermion line with one end in the initial state and the other in the final state. In the notation of Sec. 3, the primary subchannels at Born and virtual level are:

$$\textcircled{1} uc \rightarrow dsg, \quad \textcircled{2} \bar{d}\bar{s} \rightarrow \bar{u}\bar{c}g, \quad \textcircled{5} u\bar{s} \rightarrow d\bar{c}g, \quad \textcircled{8} gu \rightarrow ds\bar{c}, \quad \textcircled{10} g\bar{d} \rightarrow \bar{u}s\bar{c}.$$

The real primary subchannels with only two fermion pairs are:

$$uc \rightarrow dsgg, \quad \bar{d}\bar{s} \rightarrow \bar{u}\bar{c}gg, \quad u\bar{s} \rightarrow d\bar{c}gg, \quad gu \rightarrow ds\bar{c}g, \quad g\bar{d} \rightarrow \bar{u}s\bar{c}g, \quad gg \rightarrow d\bar{u}s\bar{c}.$$

To realize real primary subchannels with three fermion pairs, we employ matrix elements that include quarks of the third generation (b and t), where we artificially set their masses to zero. The primary structures in this case are

$$\begin{aligned} uc &\rightarrow dcb\bar{t}, & uc &\rightarrow usb\bar{t}, & uc &\rightarrow dsq\bar{q}, & us &\rightarrow dsb\bar{t}, \\ \bar{d}\bar{s} &\rightarrow \bar{u}\bar{s}b\bar{t}, & \bar{d}\bar{s} &\rightarrow \bar{d}\bar{c}b\bar{t}, & \bar{d}\bar{s} &\rightarrow \bar{u}\bar{c}q\bar{q}, & \bar{d}\bar{c} &\rightarrow \bar{u}\bar{c}b\bar{t}, \\ \bar{d}\bar{s} &\rightarrow d\bar{c}b\bar{t}, & u\bar{c} &\rightarrow d\bar{c}b\bar{t}, \\ u\bar{s} &\rightarrow d\bar{s}b\bar{t}, & u\bar{s} &\rightarrow u\bar{c}b\bar{t}, & u\bar{s} &\rightarrow d\bar{c}q\bar{q}, \end{aligned}$$

where $q\bar{q} = b\bar{b}, t\bar{t}$.

Certain (non-primary) flavor structures can be mapped to more than one primary flavor structure. This is the case for subchannels that have a $q\bar{q}$ pair in the final state and contain another fermion pair of the same family. One example is

$$u\bar{s} \rightarrow d\bar{c}u\bar{u},$$

which can be mapped to a primary subchannel as

$$(u_1\bar{s}_2 \rightarrow d_1\bar{c}_2u_3\bar{u}_3) \rightarrow (u_1\bar{s}_2 \rightarrow d_1\bar{c}_2t_3\bar{t}_3), \quad (178)$$

as well as

$$(u_1\bar{s}_2 \rightarrow d_3\bar{c}_2u_1\bar{u}_3) \rightarrow (u_1\bar{s}_2 \rightarrow u_1\bar{c}_2b_3\bar{t}_3). \quad (179)$$

In such cases, we choose the mapping where the $q\bar{q}$ pair in the final state belongs to the same fermion line, which in our example is mapping (178). This corresponds to fixing the Born structure that one obtains by replacing the $q\bar{q}$ pair by a gluon as the underlying Born structure. The output of mapping (178) is uniquely reached by mapping the structure $(u_1\bar{s}_2 \rightarrow u_1\bar{c}_2d_3\bar{u}_3)$, for example. This choice is part of our definition of the VBS approximation.

4.2.4 The Born Suppression Factor

As mentioned in Sec. 3, the LO matrix elements of the process under consideration contain divergences that must be handled in the numerical computation to prevent unphysical results. In fact, POWHEG-BOX includes a mechanism for this very purpose. It employs a *Born Suppression Factor* (BSF) $F(\Phi_n)$, which is a function of the underlying Born kinematics Φ_n , to weight the \tilde{B} function at each phase-space point. The resulting suppressed cross section is used in the intermediate steps of the computation to prevent the importance sampling of stage 1 from focusing on the divergent regions we want to avoid, as well as to prevent numerical instabilities in the results of stage 2. In the end, the results of stages 2 and 4 are reweighted using $1/F(\Phi_n)$ to recover the true cross section.

The form of the BSF is determined by the developers. Following Refs. [105, 84], we implemented and investigated two different BSF. The first one is a multiplicative BSF and has the form:

$$F_1(\Phi_n) = \prod_{j=1}^3 \left(\frac{(p_{T,j})^2}{(p_{T,j})^2 + \Lambda_1^2} \right)^k \prod_{i \neq j}^3 \left(\frac{M_{ij}^2}{M_{ij}^2 + \Lambda_2^2} \right)^k, \quad (180)$$

where i, j index the jets and M_{ij} is the invariant mass of the ij jet pair.

Option two is an exponential BSF, of the form

$$F_2(\Phi_n) = \exp \left\{ -\Lambda_1^4 \left(\sum_{j=1}^3 \frac{1}{(p_{T,j}^2)^p} + \sum_{i \neq j}^3 \frac{1}{((p_{\text{rel}}^2(i, j))^p)} \right) \right\} \cdot \left(\frac{h^2}{h^2 + \Lambda_2^2} \right)^2, \quad (181)$$

4.3 Validation

where $p_{\text{rel}}(i, j)$ is the relative transverse momentum of jets i and j in the partonic center-of-mass system and $h = \left(\sum_{j=1}^3 p_{T,j}^2\right)$. The values of Λ_i and k, p can be varied by the user. The default choices are $k = 2 = p$ and $\Lambda_1 = \Lambda_2 = 20$ GeV for F_1 and $\Lambda_1 = 10$ GeV, $\Lambda_2 = 30$ GeV for F_2 .

4.3 Validation

In this short section, we describe which steps were taken for the validation of our implementation.

To test that the diagram selection of `MadGraph5_aMC@NLO` that we employed to exclude s -channel EW propagators produces gauge-invariant matrix elements, we checked that these fulfill the *Ward identity* for external gluons [106]. This identity states that a gauge-invariant matrix element that involves an external gauge vector boson with momentum k^μ and polarization vector $\varepsilon^\mu(k)$ vanishes upon the replacement $\varepsilon^\mu(k) \rightarrow k^\mu$. We checked that this is the case for the Born, virtual and real matrix element of one partonic subprocess of each kind. We remark that fulfilling the Ward identity is a necessary, but not a sufficient condition for gauge invariance. Nevertheless, the VBS approximation produces gauge-invariant matrix elements per construction, as discussed in Sec. 3.2.5.

Our implementation was furthermore compared to the calculation of Ref. [25], where QCD corrections to electroweak production of $e^+\nu_e\mu^+\nu_\mu jj$ at the LHC was calculated using `POWHEG BOX V2` with matrix-element routines generated using the `VBFNLO` code [107, 108, 109] in the VBS approximation. Specifically, the leading order of our implementation was compared to the real QCD correction of $e^+\nu_e\mu^+\nu_\mu jj$ production, which has one more jet. This process contains the scattering of two W^+ bosons which then each decay into a charged lepton and a neutrino, but also includes contributions in which the final-state leptons do not originate from W^+ bosons. This validation check proceeded in two steps:

1. New real matrix elements for $pp \rightarrow e^+\nu_e\mu^+\nu_\mu jj$ were generated using `MadGraph5_aMC@NLO` and integrated in the implementation of [25], which is publicly available as a `POWHEG BOX V2` process. It was confirmed that the two sets of matrix elements coincide for a handful of phase-space points.
2. The new real matrix-element routines were modified to include only contributions from Feynman diagrams with two s -channel W^+ -boson propagators. With this selection, we were able to check that the leading order of our implementation does indeed correspond to the real QCD correction of $e^+\nu_e\mu^+\nu_\mu jj$ production, restricted to diagrams that are compatible with the production of two on-shell W^+ boson and three jets and for subprocesses without gluons in the initial state.

Furthermore, some Born, real and virtual matrix elements of our implementation were compared pointwise to corresponding matrix elements generated using the `RECOLA2` program [110, 111]. This comparison is only feasible for certain subprocesses, because

RECOLA2 does not allow the exclusion of diagrams with certain s -channel propagators, as it is done in our implementation according to the VBS approximation. Specifically, the comparison of virtual matrix elements of gluon-quark initiated subprocesses, which exhibit s -channel EW propagators, can not be performed.

Finally, we corroborated that the results generated with our implementation are insensitive to technical parameters. We varied technical cut $Q_{\gamma,\min}^2$, introduced in Sec. 3.1.2, in the range 1-10 GeV² and found no significative differences. Furthermore, we checked that the results produced using the forms F_1 and F_2 of the BSF are compatible. For the form F_2 , which we employ to generate the results of Sec. 5, we additionally checked that varying the values of $\Lambda_{1/2}$ yields equivalent results.

5 Numerical Studies

In this section, we present the results of numerical calculations performed using the implementation described in Sec. 4. The contents of this section are closely based on Ref. [35], where these results were first published. We begin by giving the input parameters and settings that we employed in Sec. 5.1. In Sec. 5.2, we discuss fixed-order results and the effect of NLO QCD corrections. We then investigate PS effects in Sec. 5.3, where we first assess them with respect to our fixed-order NLO calculation and then compare different settings of the PS.

5.1 Input Parameters and Analysis Setup

The results presented in this work have been obtained using the NNPDF40_nnlo_as_01180 set [112] of parton distribution functions as implemented in the LHAPDF6 library [113]. It corresponds to $\alpha_s(M_Z) = 0.118$ and assumes the five-flavor scheme, i.e. that all quarks apart from the top-quark are massless.

For the EW input parameters we use the G_μ scheme where, besides the Fermi constant G_μ , the masses of the Z and W bosons are fixed. For our study we choose the following input values [52]:

$$M_Z = 91.1876 \text{ GeV}, \quad M_W = 80.377 \text{ GeV}, \quad G_\mu = 1.1663788 \times 10^{-5} \text{ GeV}^{-2}. \quad (182)$$

Other EW parameters like the electromagnetic coupling constant α_{em} and the weak mixing angle θ_W are derived via tree-level relations. The widths of the Z and W bosons are set to [52]:

$$\Gamma_Z = 2.4955 \text{ GeV}, \quad \Gamma_W = 2.085 \text{ GeV}. \quad (183)$$

We set the top-quark mass and width to [52]:

$$m_t = 172.5 \text{ GeV}, \quad \Gamma_t = 1.42 \text{ GeV}, \quad (184)$$

and for the mass and width of the Higgs boson we employ:

$$m_H = 125.25 \text{ GeV}, \quad \Gamma_H = 3.2 \times 10^{-3} \text{ GeV}. \quad (185)$$

The minimal photon virtuality for the technical cut discussed in Sec. 3.1.2 is set to

$$Q_{\gamma,\text{min}}^2 = 4 \text{ GeV}^2. \quad (186)$$

We employ the Born suppression factor F_2 from Eq. (181) with the default values

$$\Lambda_1 = 10 \text{ GeV} \text{ and } \Lambda_2 = 30 \text{ GeV}. \quad (187)$$

This choice is motivated by the improved grid convergence that it provides.

For the renormalization and factorization scales, we set $\mu_r = \mu_f = \mu_0$ with

$$\mu_0 = \frac{1}{2} \left(E_{T,W_1} + E_{T,W_2} + \sum_f^{n_{\text{part}}} p_{T,f} \right), \quad (188)$$

following [114], where

$$E_{T,W_i} = \sqrt{m_W^2 + p_{T,W_i}^2} \quad (189)$$

are the transverse energies of the W bosons and the sum in Eq. (188) includes the transverse momenta $p_{T,f}$ of all n_{part} final-state partons of a considered Born-type or real-emission configuration.

For the results that were obtained from events, i.e. those matched to a parton shower, we additionally perform a seven-point scale variation to estimate the renormalization and factorization scale uncertainty. Specifically, this is done by setting $\mu_r = \xi_R \mu_0$ and $\mu_f = \xi_F \mu_0$ with variation factors ξ_R and ξ_F and independently setting the scale factors ξ_F and ξ_R to the values $\frac{1}{2}$, 1 and 2 while excluding the combinations $(\xi_F, \xi_R) = (\frac{1}{2}, 2)$ and $(\xi_F, \xi_R) = (2, \frac{1}{2})$. This scale variation was done using the reweighting function of POWHEG-BOX.

To define IR-safe observables, we construct jets using the anti- k_T recombination algorithm [69] as implemented in the **FastJet** package [115] and using the distance parameter $R = 0.4$. Our phenomenological analysis imposes cuts on these jets to define the phase-space region in which the VBS approximation is trustworthy and where the QCD-induced background is small [116]. Three jets j_k , $k = 1, 2, 3$ are required with transverse momenta and rapidities such that

$$p_{T,j_k} \geq 30 \text{ GeV}, \quad |y_{j_k}| \leq 4.5. \quad (190)$$

We denote the hardest two of these jets, i.e. those with the largest transverse momentum, as the *tagging jets* j_1 and j_2 with $p_{T,j_1} > p_{T,j_2}$, and require that they are well separated and have a large invariant mass by fulfilling

$$|\Delta y_{j_1,j_2}| \geq 2.5, \quad M_{j_1,j_2} \geq 500 \text{ GeV}. \quad (191)$$

The cuts in Eqs. (190) and (191) are enforced in all the results shown in this section.

5.2 Results at Fixed Order

For the W^+W^+jjj cross sections at LO and NLO QCD integrated over the phase space within the cuts of Eqs. (190)–(191) we obtain $\sigma_{\text{LO}} = 3.214(2) \times 10^{-2}$ fb and $\sigma_{\text{NLO}} = 3.65(2) \times 10^{-2}$ fb, respectively. The Monte Carlo integration uncertainty on the last digit is given in parentheses. This corresponds to a relative QCD correction on the LO result of +13.7(9)%.

5.2 Results at Fixed Order

We now discuss differential cross sections with respect to several jet observables and discuss their main features, as well as the effects of the NLO QCD corrections on them. We distinguish the four jets that can occur in $pp \rightarrow W^+W^+jjj$ at NLO in QCD by ordering them with respect to transverse momentum, and call them j_1, j_2, j_3, j_4 , where $p_{T,j_1} > p_{T,j_2} > p_{T,j_3} > p_{T,j_4}$. Figures 22 to 24 show distributions at LO (blue) and NLO in QCD (red), together with their respective ratios. The fourth jet can only arise at NLO in QCD as real emission, and is thus effectively only described with LO accuracy. Hence, no LO curve or ratio panel is shown in observables that concern the fourth jet. Since detectable jets cannot have an arbitrarily small transverse momentum, we compute some distributions of the fourth using an additional cut

$$p_{T,j_4} \geq 20 \text{ GeV}, \quad (192)$$

which we indicate in the respective plots. The error bars in the histograms correspond to the Monte-Carlo uncertainty.

The transverse-momentum distributions of the four jets are shown in Fig. 22. For the tagging jets j_1 and j_2 , the histograms display maxima at 110–190 GeV and 70–90 GeV, respectively. This behavior is typical for VBS processes. For WZ scattering, for example, it was found that the two final-state quarks at LO that correspond to the tagging jets typically have $p_{T,1/2} \approx \mathcal{O}(M_W)$ [18]. On the other hand, very low values of the transverse momenta of the tagging jets are kinematically suppressed. This is evident in the upper-row plots of Fig. 22, where the distributions increase from the lowest allowed value 30 GeV towards larger p_T values until the corresponding maximum. The reason for this behavior can be seen in the following way. In collider coordinates, the momentum of a particle can be written as [55]

$$p = (m_T \cosh y, p_T \sin \phi, p_T \cos \phi, m_T \sinh y) \quad (193)$$

in terms of its transverse momentum p_T , transverse mass $m_T = \sqrt{p_T^2 + m^2}$, mass m , azimuthal angle ϕ and rapidity y (see definition in Eq.(122)). Using these coordinates, the invariant mass $M_{ik}^2 = (p_i + p_k)^2$ of particles i and k becomes

$$M_{ik}^2 = m_i^2 + m_k^2 + 2 [m_{T,i}m_{T,k} \cosh \Delta y_{ik} - p_{T,i}p_{T,k} \cos \Delta \phi_{ik}], \quad (194)$$

which follows immediately after using the addition theorems for the trigonometric and hyperbolic functions and where $\Delta y_{ik} = y_i - y_k$ and $\Delta \phi_{ik} = \phi_i - \phi_k$ are the rapidity and azimuthal-angle differences of the particles. For small particle masses, Eq. (194) reduces to

$$\begin{aligned} M_{ik}^2 &= m_i^2 + m_k^2 + 2 p_{T,i} p_{T,k} \left[\sqrt{1 + \frac{m_i^2}{p_{T,i}^2}} \sqrt{1 + \frac{m_k^2}{p_{T,k}^2}} \cosh \Delta y_{ik} - \cos \Delta \phi_{ik} \right] \\ &= m_i^2 + m_k^2 + 2 p_{T,i} p_{T,k} \left[\left(1 + \mathcal{O} \left(\frac{m_{i/k}^2}{p_{T,i/k}^2} \right) \right) \cosh \Delta y_{ik} - \cos \Delta \phi_{ik} \right] \\ &\approx 2 p_{T,i} p_{T,k} [\cosh \Delta y_{ik} - \cos \Delta \phi_{ik}], \end{aligned} \quad (195)$$

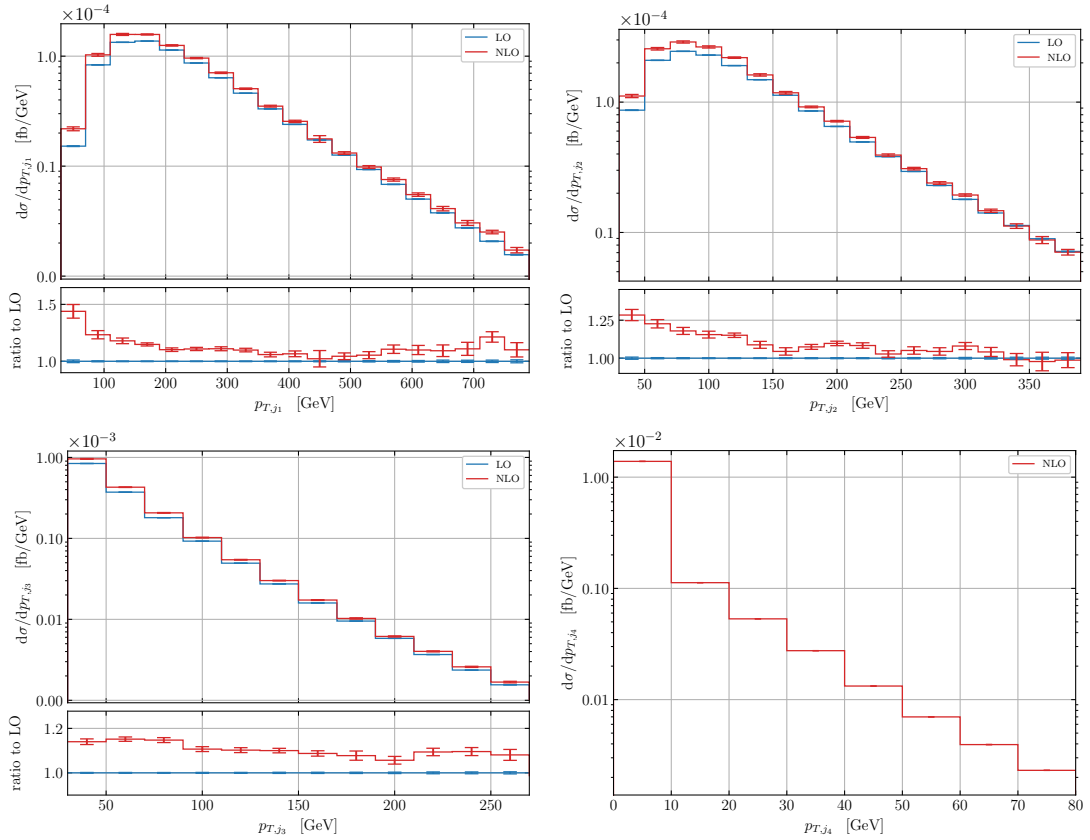


Figure 22: Distributions in transverse momentum p_{T,j_i} of the four jets that can occur in NLO W^+W^+jjj production at the LHC. Taken from Ref. [35].

where the last line becomes an equality for $m_i = m_k = 0$. Since their momentum can correspond the sum of momenta of massless particles, jets generally have non-zero masses. Nevertheless, the approximate relation in Eq. (195) can be employed if these are not too large¹⁴, see e.g. Ref. [116]. Coming back to the tagging jets, we can see that our rapidity-separation requirement from Eq. (191) translates Eq. (195) into the constraint

$$\begin{aligned}
 |\Delta y_{j_1,j_k}| &> \cosh^{-1} \left(\frac{500^2 \text{ GeV}^2}{2 p_{T,j_1} p_{T,j_2}} + \cos \Delta \phi_{j_1,j_2} \right) \\
 &> \cosh^{-1} \left(\frac{500^2 \text{ GeV}^2}{2 p_{T,j_1} p_{T,j_2}} - 1 \right), \quad (196)
 \end{aligned}$$

which means that if p_{T,j_1}, p_{T,j_2} become too small, $|\Delta y_{j_1,j_k}|$ is forced to take larger, less likely values, cf. the upper-left plot in Fig. 24.

¹⁴This is the case if the angles between clustered particles are small, since for the cluster of two massless particles with momenta p, q it is $m^2 = (p+q)^2 = 2|\vec{p}||\vec{q}|\cos\theta_{pq}$, with the angle θ_{pq} between \vec{p} and \vec{q} .

5.2 Results at Fixed Order

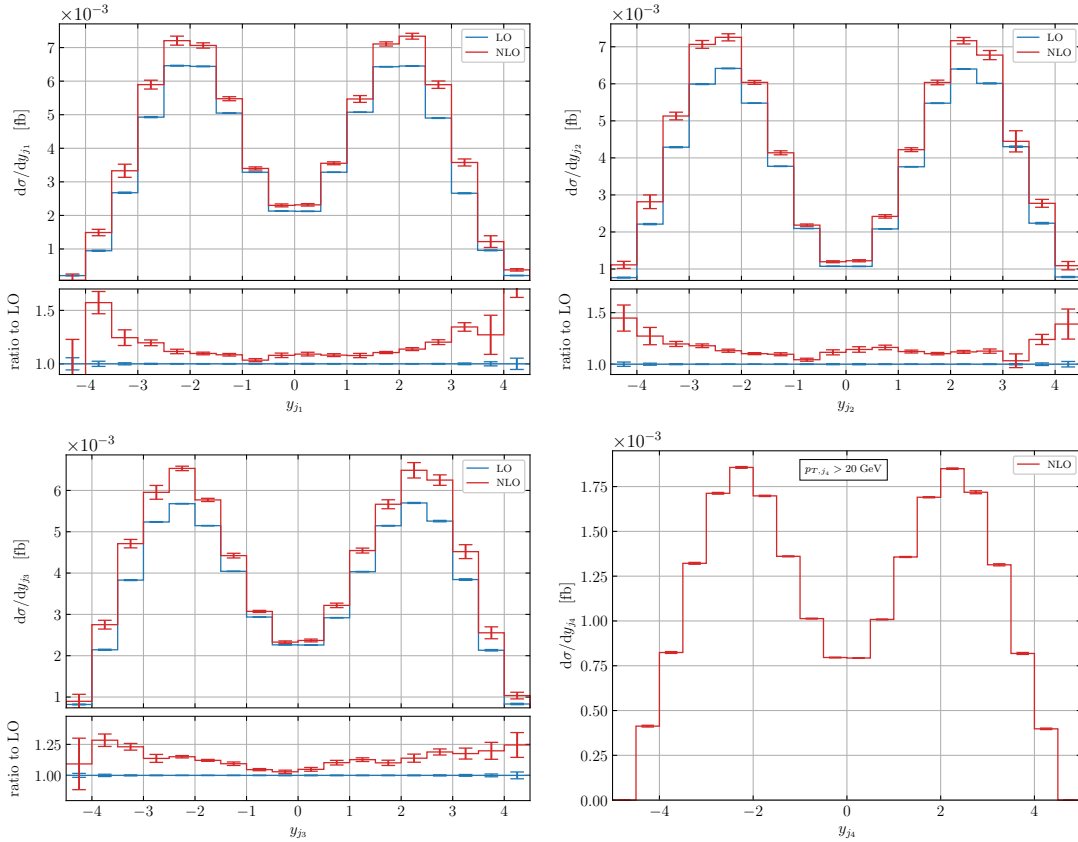


Figure 23: Distributions in the rapidities y_{j_1} of the four jets. For the rapidity distribution of the fourth jet the additional cut of Eq. (192) is imposed. Taken from Ref. [35].

The transverse-momentum distributions of the subleading jets j_3 and j_4 , which are not constrained by an invariant-mass cut, strongly increase towards small values. For the tagging jets, the largest QCD corrections are concentrated at low values of p_T , and they are largest for the hardest jet. This is likely due to soft and/or collinear real emission off one of the hardest partons that is recombined with either of them instead of giving rise to a fourth jet. In the case of the third jet, the correction is not strongly localized but similar in size throughout the shown p_T -range.

Figure 23 displays the rapidity distribution of each jet. For the three hardest jets, the NLO corrections increase towards larger absolute values of their rapidity. Both LO and NLO rapidity distributions of all jets assume their maximal values between ± 2 and ± 2.5 . As was discussed in Sec. 3, this is expected for the tagging jets in VBS processes, which are mostly forward and back-to-back and also for the subleading jets, which are often radiated by the tagging jets and are close to them in position [5]. This behavior has been observed before for the third jet in VBS processes in Refs. [84, 117]), for example, and is compatible with the distributions of jet rapidity-differences shown in Fig. 24. The upper-left plot shows the $\Delta y_{j_1, j_2}$

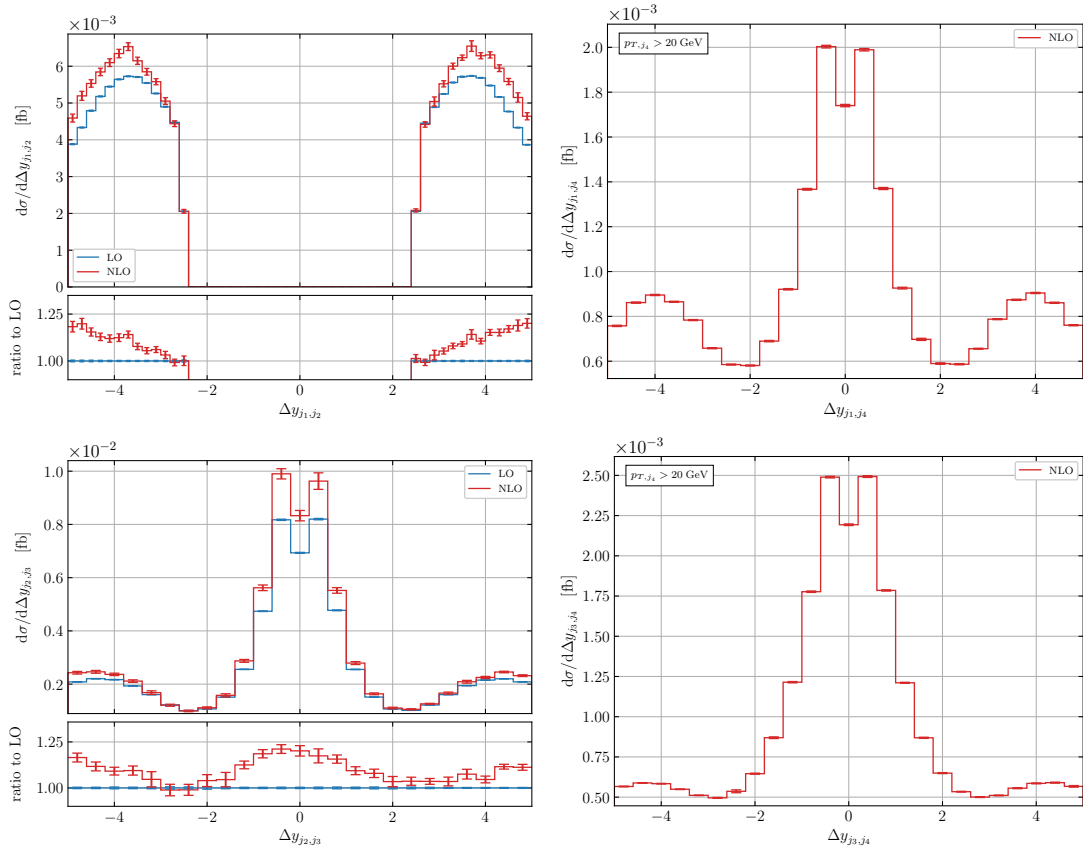


Figure 24: Distributions of the rapidity differences $\Delta y_{j_i, j_k}$ of the tagging jets (top left), one tagging and one non-tagging jet (top-right, bottom-left) and non-tagging jets (bottom right). For distributions involving the fourth jet the additional cut of 192 is imposed. Taken from Ref. [35].

distribution. The total absence of events in the range from -2.5 to 2.5 corresponds to the separation cut of Eq. (190). The LO and NLO distributions assume their maxima at ± 3.8 , and the NLO corrections slightly increase towards larger rapidity separations. Considering that the typical rapidities of the tagging jets are around ± 2.25 as shown in Fig. 23, the behavior of $\Delta y_{j_1, j_2}$ indicates that the tagging jets are often, as expected, in opposite sides of the detector.

In contrast, the rapidity separations of a non-tagging jet to one of the tagging jets and of the two non-tagging jets tend to be small. This corresponds to configurations where these jets have rapidities of the same sign and similar magnitude. Instead of peaking at 0, these distributions have two maxima at $\Delta y_{j_i, j_k} \approx \pm 0.4$ and display a dip between those values. This is due to the requirement of a minimal separation that the anti- k_T clustering algorithm implies, see Sec. 1.6. The distance parameter $R = 0.4$ of the recombination algorithm represents the lower bound on the separation ΔR_{ik} of the jets j_i and j_k , defined in Eq. (121). To satisfy $\Delta R_{ik} > R$ for values of Δy_{ik} smaller than 0.4, the azimuthal-angle difference $\phi_{i,k}$ is forced to take higher

5.3 Parton-Shower Results

values, which results in a phase-space suppression for such configurations. The local maxima at rapidity-difference values of around ± 4 displayed by the plots on the top-right and bottom row of Fig. 24 correspond to configurations in which the corresponding jets have opposite-sign rapidities of the typical magnitude 2.25. In the bottom-left plot of Fig. 24, the QCD correction is localized around values where the LO distribution is itself large.

5.3 Parton-Shower Results

To assess PS effects, we match our calculation to PYTHIA 8.240 using the **Monash 2013** tune, see Sec. 1.5, and turn off QED showering, so that only branchings of color-charged particles are simulated.

We begin by comparing results at fixed NLO against NLO matched to PS, which we denote NLO+PS in the following. For this comparison, we deactivate multi-parton interactions (MPI), which are used to describe effects of the underlying event [67], as well as hadronization effects. Furthermore, we employ the dipole recoil scheme of the PYTHIA initial-state shower instead of the default¹⁵ global recoil, and denote this choice of settings the **PY+DS** setup. In the dipole scheme, the recoiling system consists only of the subset of particles that are color-connected to the emitter¹⁶, leading to a better description of color-coherence effects in the radiation pattern [118]. These are crucial for the correct description of DIS-like processes, in which the fact that the color flows between initial- and final-state partons causes a suppression of gluon radiation in the central region [119]. As was discussed in Sec. 3, VBS is DIS-like in this respect, and it has been shown that a dipole recoil scheme is more appropriate for describing VBF in NLO+PS calculations [120]. Thus, we adopt the dipole recoil scheme to compare against NLO results.

For the NLO+PS cross section integrated within the selection cuts of Eqs. (190)-(191) we obtain $\sigma_{\text{PY+DS}} = 3.45(1) \times 10^{-2}$ fb, which represents an 8.2% reduction with respect to the fixed-order result stated in Sec. 5.2. This is an expected effect, since fewer events pass the selection cuts at NLO+PS level due to the energy loss of the jets from the additional radiation generated by the PS.

We now turn to a discussion of PS effects on NLO differential distributions, shown in Figs. 25 and 26. There, the error bars indicate the Monte-Carlo uncertainty, while the bands indicate scale uncertainties obtained by a 7-point variation of μ_f and μ_r . Figure 25 shows the transverse-momentum and rapidity distributions of the tagging jets, which display only slight PS effects. The top plots of Fig. 26 show the p_T distributions of the non-tagging jets. As is the case for the leading jets, the p_{T,j_3} NLO distribution is only slightly affected by the PS. On the other hand,

¹⁵For the final-state shower, we use the default, which is a dipole recoil scheme.

¹⁶The color structure of each hard event is contained in the LHEF event file produced by **POWHEG BOX**. Thus, the PS knows which particles are color-connected at the beginning of the shower and it can keep track of the color flow in subsequent splittings.

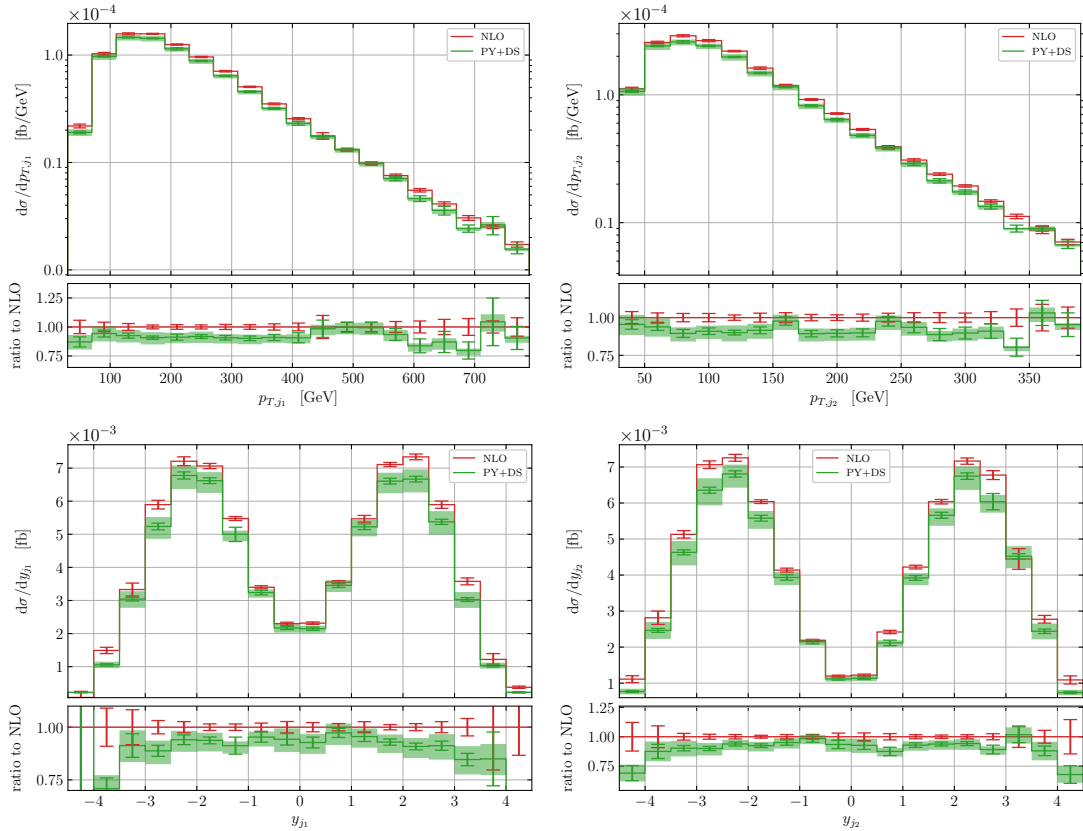


Figure 25: Transverse momentum and rapidity distributions of the two tagging at NLO (red) and NLO+PS (green) using the dipole shower in PYTHIA 8. Taken from Ref. [35].

the spectrum of the fourth jet is strongly influenced in the low- p_T regime. This typical PS effect dampens the divergent behavior of very soft real emissions, and is due to the resummation-like correction that the PS implements in the phase-space region where perturbation theory becomes unreliable, e.g. where large logarithms arise [121]. The description of the fourth jet, which at fixed-order is effectively only LO accurate, is thus improved in this respect.

In order to assess the separation of a non-tagging jet $i = 3, 4$ from the tagging jets, we consider its rapidity relative to the center of the tagging-jet system,

$$y_{ji}^* = y_{ji} - \frac{y_{j1} + y_{j2}}{2}. \quad (197)$$

The corresponding distributions are shown in the lower plots of Fig. 26. Similarly to the p_T distributions, the relative rapidity of the third jet in the PY+DS setup is comparable to the NLO result within the estimated scale uncertainties, which. For the fourth jet, however, we see that the PS shifts the relative rapidity away from the central region towards higher values of $|y_{j4}^*|$. This effect is strongly dependent upon the chosen recoil scheme, as we will see below.

5.3 Parton-Shower Results

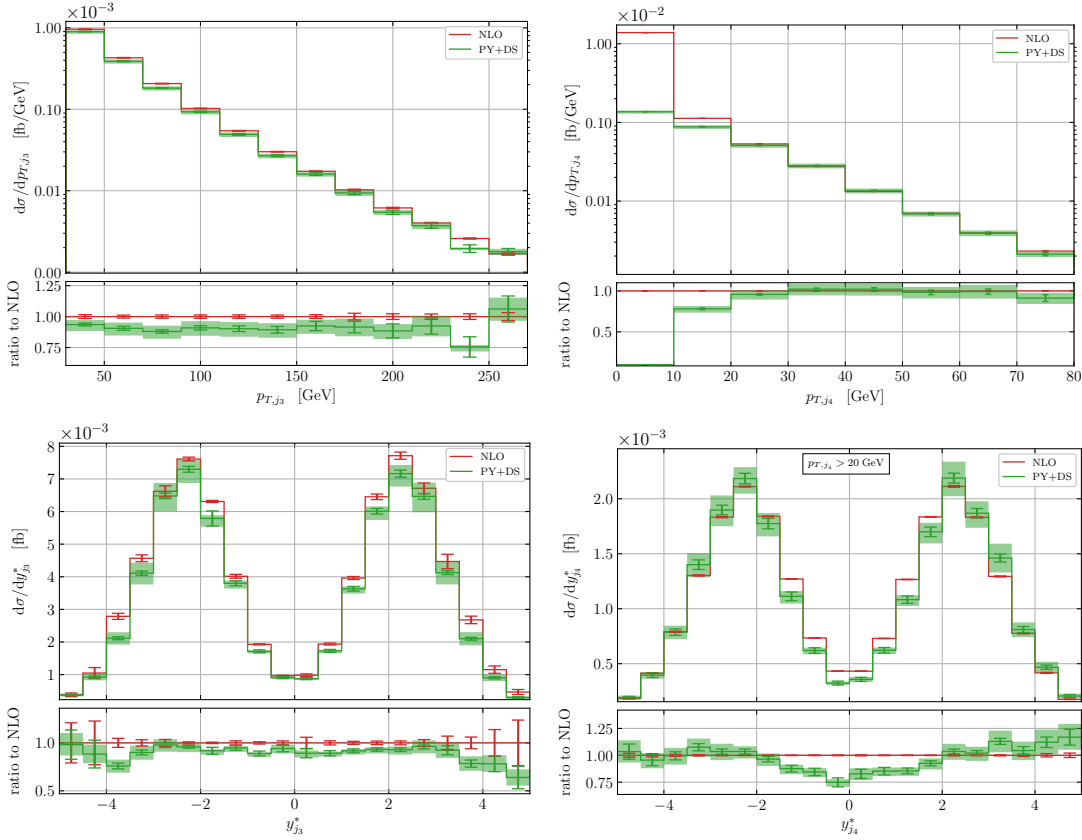


Figure 26: Transverse-momentum and relative-rapidity distributions of the non-tagging jets at NLO and NLO+PS. For the $y_{j_4}^*$ distributions the additional cut of 192 is imposed. Taken from Ref. [35].

To test our expectations on the chosen PS settings, we now consider three additional setups. We define the PY+GS setup, in which we use the global recoil scheme of PYTHIA 8 instead of the dipole recoil scheme. As for the PY+DS setup, MPI and hadronization are turned off in the PY+GS setup to allow for a direct comparison of recoil schemes. To investigate the non-perturbative effects of the PS, we also define the PY+DS+MPI+HAD and PY+GS+MPI+HAD setups in which the dipole or global recoil scheme is used, respectively, and additionally MPI and hadronization effects are activated. Figure 27 displays predictions for the rapidity distributions of the tagging jets and the rapidity-difference distributions of the subleading jets using these four different setups.

For the distributions of the tagging jets, all predictions agree within their scale uncertainties. On the other hand, there are deviations visible beyond the scale uncertainty in the y^* distributions of the subleading jets. The differences are concentrated in the central region, where the setups that employ global recoil scheme (orange and pink curved) evidently predict more events than those using the dipole recoil scheme (green and purple curves). For $y_{j_3}^*$, the relative difference

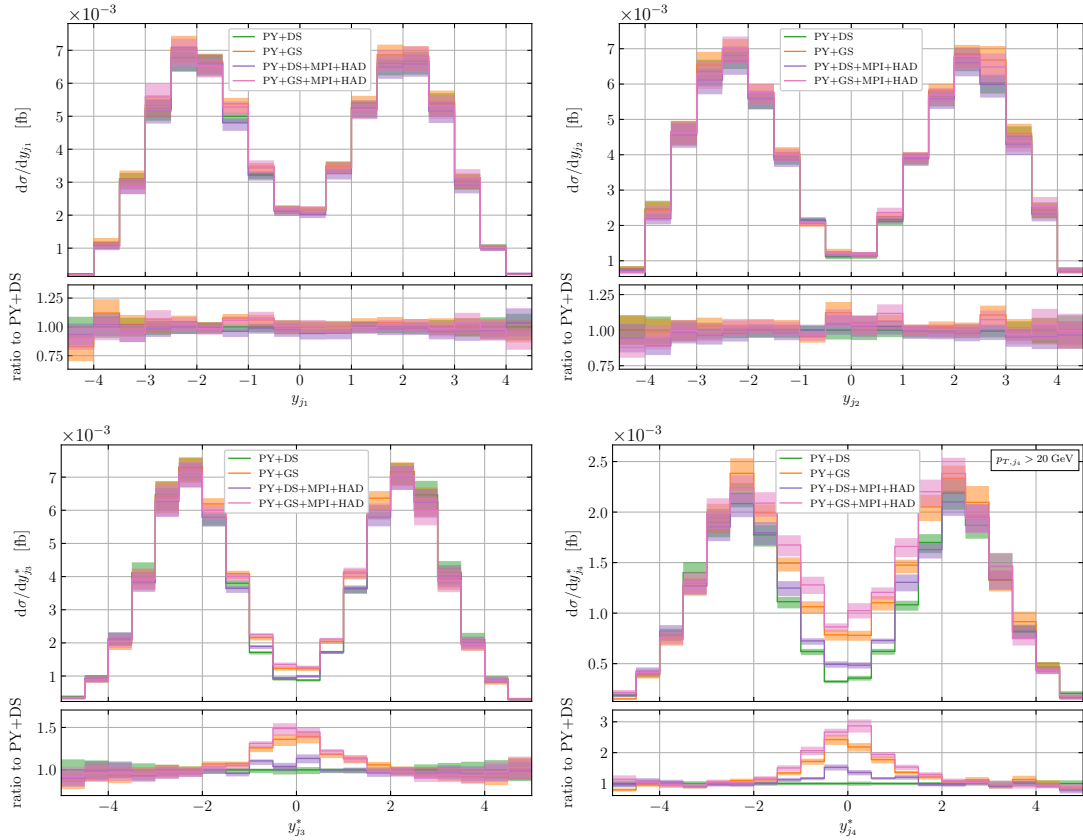


Figure 27: Rapidity distributions of the tagging jets (upper plots) and rapidity distributions of the non-tagging jets relative to the tagging jets (lower plots) at NLO+PS accuracy for the PY+DS (green), PY+GS (orange), and PY+DS+MPI+HAD (purple) setups, and their ratios to the PY+DS results. For the $y_{j_4}^*$ distributions the additional cut of Eq. (192) is imposed. Based on Fig. 11 of Ref. [35].

between the PY+GS and PY+DS predictions in the bins between -0.5 and 0.5 reaches $\sim 40\%$, and it even exceeds 100% for $y_{j_4}^*$. For both recoil schemes, considering MPI and hadronization effects results in a slight increase of events with low values of y_j^* . Nevertheless, the predictions of different recoil schemes display the largest differences. The distributions of the subleading jets as predicted by the dipole recoil scheme lie closer to the the pure fixed-order results than the prediction using the global recoil scheme, cf. Fig. 26. This observation is in agreement with expectations from the literature [120] and supports the existing recommendation [119] of using a PS algorithm that takes color-coherence into account.

Summary and Outlook

In this thesis, we presented a calculation of the scattering of two W^+ bosons at the LHC with three jets in the final state, as well as its NLO corrections in QCD. This was performed in the `POWHEG BOX RES` framework, which allows the matching to a PS and thereby a more accurate description of collision events. Furthermore, we present a phenomenological study in which we assess the effects on jet observables of the different simulation layers that our calculation is capable of performing.

The first part of this thesis was devoted to a review of the theoretical framework of perturbative calculations for collider events. There, some principles of quantum field theory for particle physics and the SM were reviewed. We then discussed in some detail how NLO calculations are performed in the FKS subtraction scheme and matched to PS programs using the POWHEG method in the second part.

In the third part, we introduced the process of W^+W^+ scattering and highlight its relevance as a probe for new-physics effects in the EW sector of the SM. Furthermore, we discussed W^+W^+ scattering at the LHC and the importance of an accurate jet description for the event selection. We then turned to the underlying process of electroweak W^+W^+jjj production and the LHC, which contains VBS scattering, and reviewed its contributions at LO and NLO. Afterwards we discussed the VBS signature, which consists in two far-forward tagging jets with large invariant mass and opposite-signed rapidities, and used it to motivate the VBS approximation that we employed for our calculation. In this approximation, kinematically- and color-suppressed contributions are excluded from the calculation. The retained terms can be constructed by means of the structure-function approach, yielding a theoretically well-defined set of contributions.

The fourth part of this work is concerned with the numerical implementation of the calculation. We began by introducing the `POWHEG BOX` program, which is a parton-level event generator that implements the POWHEG matching strategy. We then detail how we construct the necessary building blocks to perform our calculation within this framework in a way that is consistent with the VBS approximation, and present the checks we employed to validate our implementation.

In the fifth and final section, we showed numerical studies produced with our implementation with a focus on jet kinematics. These were performed using selection cuts to define a phase-space region in which VBS contributions are enhanced and the VBS approximation is expected to be valid. We first showed results at fixed LO and NLO in QCD. We found a 13.8% relative QCD correction for the cross section integrated over the considered phase-space region. Furthermore, we discussed the general features of several differential distributions, as well as the effect of the NLO QCD corrections on these. We found typical VBS behaviors of the transverse-momentum and rapidity distributions of jets, and NLO effects that only moderately affect the distribution shapes. This is in particular the case for the third jet, which is described with NLO accuracy in our FO calculation.

Then, we compared fixed NLO results with those matched to the PS of `PYTHIA 8` using the dipole recoil scheme, which is recommended for processes like VBS. Beyond an expected reduction of the integrated cross section, we found only slight deviations between the NLO and NLO+PS descriptions of the three hardest jets at the differential level. For the fourth jet, whose low-energy kinematics are described by the Sudakov form factor at the NLO+PS level, we found the expected damping of the stark growth towards the soft region present in p_T distributions of real radiation at fixed order. Furthermore, we observed that the NLO and NLO+PS predictions for the relative rapidity of the fourth jet differ in the central region. There, the PS effect is a reduction of the expected events.

Finally, we compared the predictions for the rapidity distributions of the jets produced by different PS settings. Specifically, we varied the recoil scheme and also assessed the effects of non-perturbative parts of the PS simulation. We found that the three studied settings produced compatible predictions for the two hardest jets. Large differences arose between the NLO+PS predictions for the subleading jets using the dipole or global recoil scheme. Particularly for the fourth jet, the latter caused a significant increase in events with low $|y_j^*|$ values, and there was a larger difference between the corresponding distribution with respect to its fixed NLO counterpart. This discrepancy between recoil schemes has been observed before for VBS processes, and is due to the fact that the dipole recoil scheme considers the color structure of the process, whereas the global scheme does not. The effect of non-perturbative aspects of the PS was slighter than the effect of the recoil scheme, and we concluded that our findings support the existing recommendation [119] of using a PS algorithm that takes color-coherence into account.

Our fixed-order calculation represents an improvement upon existing VBS studies in the sense that the description of the third jet includes NLO effects in QCD. Furthermore, our calculation can be matched to a PS, which has significant effects on jet observables. The improved description that our calculation offers becomes especially relevant if central-jets are vetoed as part of selection cuts in measurements of VBS at the LHC.

In its current state, the code we developed can be employed to perform more detailed studies of PS effects, for example under closer consideration of the mismatch in ordering variables between `POWHEG BOX` and `PYTHIA 8`, as suggested in Ref. [119]. Furthermore, it may be used for phenomenological studies in which the decay products of the W^+ bosons, generated by the `PYTHIA 8`, are taken into account. Although our software package is fully functional, further development is necessary to optimize it and bring it into a more user-friendly shape. Therefore, we leave its publication for follow-up work.

In the future, it would be desirable to assess the validity of the VBS approximation we employ at this jet-multiplicity level. Non-VBS contributions could become relevant in the VBS phase space by circumventing the selection cuts in the presence of the extra jet. Furthermore, considering the decay products of the W^+ bosons at the level of the hard process would be interesting, also in the semi-leptonic channel

where more jets arise already at LO. Finally, it would be very valuable to study the impact of EW corrections to the $pp \rightarrow W^+W^+jjj$ process, which have been found to be very large for VBS with two jets [26, 27, 28].

References

- [1] ATLAS collaboration, G. Aad et al., *Observation of a new particle in the search for the Standard Model Higgs boson with the ATLAS detector at the LHC*, *Phys. Lett. B* **716** (2012) 1 [1207.7214].
- [2] CMS collaboration, S. Chatrchyan et al., *Observation of a New Boson at a Mass of 125 GeV with the CMS Experiment at the LHC*, *Phys. Lett. B* **716** (2012) 30 [1207.7235].
- [3] D. R. Green, P. Meade and M.-A. Pleier, *Multiboson interactions at the LHC*, *Rev. Mod. Phys.* **89** (2017) 035008 [1610.07572].
- [4] B. W. Lee, C. Quigg and H. B. Thacker, *Weak interactions at very high energies: The role of the higgs-boson mass*, *Phys. Rev. D* **16** (1977) 1519.
- [5] M. Rauch, *Vector-boson fusion and vector-boson scattering*, 1610.08420.
- [6] A. Ballestrero et al., *Precise predictions for same-sign W-boson scattering at the LHC*, *Eur. Phys. J. C* **78** (2018) 671 [1803.07943].
- [7] ATLAS collaboration, G. Aad et al., *Evidence for Electroweak Production of $W^\pm W^\pm jj$ in pp Collisions at $\sqrt{s} = 8$ TeV with the ATLAS Detector*, *Phys. Rev. Lett.* **113** (2014) 141803 [1405.6241].
- [8] CMS collaboration, A. M. Sirunyan et al., *Observation of electroweak production of same-sign W boson pairs in the two jet and two same-sign lepton final state in proton-proton collisions at $\sqrt{s} = 13$ TeV*, *Phys. Rev. Lett.* **120** (2018) 081801 [1709.05822].
- [9] ATLAS collaboration, M. Aaboud et al., *Observation of electroweak production of a same-sign W boson pair in association with two jets in pp collisions at $\sqrt{s} = 13$ TeV with the ATLAS detector*, *Phys. Rev. Lett.* **123** (2019) 161801 [1906.03203].
- [10] ATLAS collaboration, M. Aaboud et al., *Observation of electroweak $W^\pm Z$ boson pair production in association with two jets in pp collisions at $\sqrt{s} = 13$ TeV with the ATLAS detector*, *Phys. Lett. B* **793** (2019) 469 [1812.09740].
- [11] ATLAS collaboration, G. Aad et al., *Evidence for electroweak production of two jets in association with a $Z\gamma$ pair in pp collisions at $\sqrt{s} = 13$ TeV with the ATLAS detector*, *Phys. Lett. B* **803** (2020) 135341 [1910.09503].
- [12] ATLAS collaboration, G. Aad et al., *Observation of electroweak production of two jets and a Z-boson pair*, *Nature Phys.* **19** (2023) 237 [2004.10612].
- [13] CMS collaboration, S. Chatrchyan et al., *Study of Exclusive Two-Photon Production of W^+W^- in pp Collisions at $\sqrt{s} = 7$ TeV and Constraints on Anomalous Quartic Gauge Couplings*, *JHEP* **07** (2013) 116 [1305.5596].
- [14] CMS collaboration, V. Khachatryan et al., *Evidence for exclusive $\gamma\gamma \rightarrow W^+W^-$ production and constraints on anomalous quartic gauge couplings in pp collisions at $\sqrt{s} = 7$ and 8 TeV*, *JHEP* **08** (2016) 119 [1604.04464].

References

- [15] A. Collaboration, “ATLAS Feature: Unraveling Nature’s secrets – vector boson scattering at the LHC.” 2020.
- [16] V. Barger, K. Cheung, T. Han and D. Zeppenfeld, *Single-forward-jet tagging and central-jet vetoing to identify the leptonic WW decay mode of a heavy higgs boson*, *Phys. Rev. D* **44** (1991) 2701.
- [17] V. Barger, K. Cheung, T. Han and R. J. N. Phillips, *Strong W^+W^+ scattering signals at pp supercolliders*, *Phys. Rev. D* **42** (1990) 3052.
- [18] V. D. Barger, K.-m. Cheung, T. Han, A. Stange and D. Zeppenfeld, *Full tree level calculation of the $qq \rightarrow qqWZ$ electroweak process at hadron supercolliders*, *Phys. Rev. D* **46** (1992) 2028.
- [19] G. Bozzi, B. Jager, C. Oleari and D. Zeppenfeld, *Next-to-Leading Order QCD Corrections to W^+Z and W^-Z Production via Vector-Boson Fusion*, *Physical Review D* **75** (2007) 073004 [[hep-ph/0701105](#)].
- [20] A. Denner, R. Franken, T. Schmidt and C. Schwan, *NLO QCD and EW Corrections to Vector-Boson Scattering into W^+W^- at the LHC*, *Journal of High Energy Physics* **2022** (2022) 98 [[2202.10844](#)].
- [21] B. Jager, C. Oleari and D. Zeppenfeld, *Next-to-leading order QCD corrections to Z boson pair production via vector-boson fusion*, *Phys. Rev. D* **73** (2006) 113006 [[hep-ph/0604200](#)].
- [22] B. Jager, C. Oleari and D. Zeppenfeld, *Next-to-Leading Order QCD Corrections to W^+W^+jj and W^-W^-jj Production via Weak-Boson Fusion*, *Physical Review D* **80** (2009) 034022 [[0907.0580](#)].
- [23] B. Jager and G. Zanderighi, *Electroweak W^+W^-jj Production at NLO in QCD Matched with Parton Shower in the POWHEG-BOX*, *Journal of High Energy Physics* **2013** (2013) 24 [[1301.1695](#)].
- [24] B. Jager, A. Karlberg and G. Zanderighi, *Electroweak $ZZjj$ Production in the Standard Model and beyond in the POWHEG-BOX V2*, *Journal of High Energy Physics* **2014** (2014) 141 [[1312.3252](#)].
- [25] B. Jager and G. Zanderighi, *NLO Corrections to Electroweak and QCD Production of W^+W^+ plus Two Jets in the POWHEGBOX*, *Journal of High Energy Physics* **2011** (2011) 55 [[1108.0864](#)].
- [26] B. Biedermann, A. Denner and M. Pellen, *Large electroweak corrections to vector-boson scattering at the Large Hadron Collider*, *Phys. Rev. Lett.* **118** (2017) 261801 [[1611.02951](#)].
- [27] B. Biedermann, A. Denner and M. Pellen, *Complete NLO corrections to W^+W^+ scattering and its irreducible background at the LHC*, *JHEP* **10** (2017) 124 [[1708.00268](#)].
- [28] S. Dittmaier, P. Maierhöfer, C. Schwan and R. Winterhalder, *Like-sign W-boson scattering at the LHC — approximations and full next-to-leading-order predictions*, *JHEP* **11** (2023) 022 [[2308.16716](#)].

- [29] M. Chiesa, A. Denner, J.-N. Lang and M. Pellen, *An event generator for same-sign W-boson scattering at the LHC including electroweak corrections*, *The European Physical Journal C* **79** (2019) 788 [1906.01863].
- [30] A. Denner, S. Dittmaier, P. Maierhöfer, M. Pellen and C. Schwan, *QCD and electroweak corrections to WZ scattering at the LHC*, *JHEP* **26** (2019) 067 [1904.00882].
- [31] A. Denner, R. Franken, M. Pellen and T. Schmidt, *NLO QCD and EW Corrections to Vector-Boson Scattering into ZZ at the LHC*, *Journal of High Energy Physics* **2020** (2020) 110 [2009.00411].
- [32] J. M. Campbell and R. K. Ellis, *Higgs Constraints from Vector Boson Fusion and Scattering*, *JHEP* **04** (2015) 030 [1502.02990].
- [33] P. Nason, *A New method for combining NLO QCD with shower Monte Carlo algorithms*, *JHEP* **11** (2004) 040 [hep-ph/0409146].
- [34] S. Frixione, P. Nason and C. Oleari, *Matching nlo qcd computations with parton shower simulations: the powheg method*, *JHEP* **11** (2007) .
- [35] B. Jäger and S. L. P. Chavez, *Electroweak $W^+ W^+$ production in association with three jets at NLO QCD matched with parton shower*, *JHEP* **01** (2025) 075 [2408.12314].
- [36] G. C. Wick, *The evaluation of the collision matrix*, *Phys. Rev.* **80** (1950) 268.
- [37] M. Gell-Mann and F. Low, *Bound states in quantum field theory*, *Phys. Rev.* **84** (1951) 350.
- [38] M. E. Peskin and D. V. Schroeder, *An Introduction to quantum field theory*. Addison-Wesley, Reading, USA, 1995.
- [39] T. Muta, *Foundations of Quantum Chromodynamics: An Introduction to Perturbative Methods in Gauge Theories*, vol. 5 of *World Scientific Lecture Notes in Physics*. World Scientific, Sept., 1987, 10.1142/0022.
- [40] C. Becchi, A. Rouet and R. Stora, *Renormalization of Gauge Theories*, *Les rencontres physiciens-mathématiciens de Strasbourg -RCP25* **22** (1975) .
- [41] I. V. Tyutin, *Gauge Invariance in Field Theory and Statistical Physics in Operator Formalism*, 0812.0580.
- [42] M. Böhm, A. Denner and H. Joos, *Gauge Theories of the Strong and Electroweak Interaction*. Vieweg+Teubner Verlag, Wiesbaden, 2001, 10.1007/978-3-322-80160-9.
- [43] G. Sterman, *An Introduction to Quantum Field Theory*. Cambridge University Press, Cambridge, 1993, 10.1017/CBO9780511622618.
- [44] H. Lehmann, K. Symanzik and W. Zimmermann, *Zur Formulierung quantisierter Feldtheorien*, *Il Nuovo Cimento (1955-1965)* **1** (1955) 205.
- [45] G. Passarino and M. J. G. Veltman, *One Loop Corrections for $e^+ e^-$ Annihilation Into $\mu^+ \mu^-$ in the Weinberg Model*, *Nucl. Phys. B* **160** (1979) 151.

References

- [46] N. Agarwal, L. Magnea, C. Signorile-Signorile and A. Tripathi, *The Infrared Structure of Perturbative Gauge Theories*, Dec., 2021.
- [47] T. Kinoshita, *Mass singularities of feynman amplitudes*, *Journal of Mathematical Physics* **3** (1962) 650.
- [48] T. D. Lee and M. Nauenberg, *Degenerate systems and mass singularities*, *Phys. Rev.* **133** (1964) B1549.
- [49] G. 't Hooft, *Renormalization of Massless Yang-Mills Fields*, *Nucl. Phys. B* **33** (1971) 173.
- [50] G. 't Hooft, *Renormalizable Lagrangians for Massive Yang-Mills Fields*, *Nucl. Phys. B* **35** (1971) 167.
- [51] C. Burgess and G. Moore, *The Standard Model: A Primer*. Cambridge University Press, 2012.
- [52] PARTICLE DATA GROUP collaboration, R. L. Workman et al., *Review of Particle Physics*, *PTEP* **2022** (2022) 083C01.
- [53] J. Campbell, J. Huston and F. Krauss, *The black book of quantum chromodynamics: a primer for the LHC era*. Oxford University Press, 2018.
- [54] W. Vogelsang, *Skript zur Vorlesung Quantenfeldthorie 2*, April, 2018.
- [55] R. K. Ellis, W. J. Stirling and B. R. Webber, *QCD and Collider Physics*, Cambridge Monographs on Particle Physics, Nuclear Physics and Cosmology. Cambridge University Press, 1996, 10.1017/CBO9780511628788.
- [56] M. D. Schwartz, *Quantum Field Theory and the Standard Model*. Cambridge University Press, 2013, 10.1017/9781139540940.
- [57] J. Alwall, M. Herquet, F. Maltoni, O. Mattelaer and T. Stelzer, *MadGraph 5 : Going Beyond*, *JHEP* **06** (2011) 128 [1106.0522].
- [58] G. Zweig, *An SU_3 model for strong interaction symmetry and itsbreaking; Version 2*, .
- [59] M. Gell-Mann, *A schematic model of baryons and mesons*, *Physics Letters* **8** (1964) 214.
- [60] J. D. Bjorken, *Asymptotic sum rules at infinite momentum*, *Phys. Rev.* **179** (1969) 1547.
- [61] J. D. Bjorken and E. A. Paschos, *Inelastic electron-proton and γ -proton scattering and the structure of the nucleon*, *Phys. Rev.* **185** (1969) 1975.
- [62] W. Panofsky and H. Kurt, *Low q electrodynamics, elastic and inelastic electron (and muon) scattering*, .
- [63] R. Feynman, *Photon-hadron interactions*, *Frontiers in Physics* (1973) .
- [64] J. Aubert et al., *Measurements of the nucleon structure functions F_2N in deep inelastic muon scattering from deuterium and comparison with those from hydrogen and iron*, *Nuclear Physics B* **293** (1987) 740.
- [65] B. Andersson, G. Gustafson, G. Ingelman and T. Sjöstrand, *Parton fragmentation and string dynamics*, *Physics Reports* **97** (1983) .

- [66] T. Gleisberg, S. Hoeche, F. Krauss, M. Schonherr, S. Schumann, F. Siegert et al., *Event generation with SHERPA 1.1*, *JHEP* **02** (2009) 007 [0811.4622].
- [67] T. Sjöstrand, S. Ask, J. R. Christiansen, R. Corke, N. Desai, P. Ilten et al., *An Introduction to PYTHIA 8.2*, *Computer Physics Communications* **191** (2015) 159 [1410.3012].
- [68] P. Skands, S. Carrazza and J. Rojo, *Tuning PYTHIA 8.1: the Monash 2013 Tune*, *Eur. Phys. J. C* **74** (2014) 3024 [1404.5630].
- [69] M. Cacciari, G. P. Salam and G. Soyez, *The Anti-Kt Jet Clustering Algorithm*, *Journal of High Energy Physics* **2008** (2008) 063.
- [70] S. Catani and M. Seymour, *A General algorithm for calculating jet cross-sections in NLO QCD*, *Nucl. Phys. B* **485** (1997) 291 [hep-ph/9605323].
- [71] S. Frixione, Z. Kunszt and A. Signer, *Three jet cross-sections to next-to-leading order*, *Nucl. Phys. B* **467** (1996) 399 [hep-ph/9512328].
- [72] T. Ježo and P. Nason, *On the Treatment of Resonances in Next-to-Leading Order Calculations Matched to a Parton Shower*, *Journal of High Energy Physics* **2015** (2015) 1 [1509.09071].
- [73] S. Frixione, Z. Kunszt and A. Signer, *Three-jet cross sections to next-to-leading order*, *Nuclear Physics B* **467** (1996) 399 [hep-ph/9512328].
- [74] Z. Kunszt and D. E. Soper, *Calculation of jet cross sections in hadron collisions at order α_s^3* , *Physical Review D* **46** (1992) 192.
- [75] R. Frederix, S. Frixione, F. Maltoni and T. Stelzer, *Automation of next-to-leading order computations in QCD: The FKS subtraction*, *Journal of High Energy Physics* **2009** (2009) 003 [0908.4272].
- [76] S. Gieseke, *Simulation of jets at colliders*, *Progress in Particle and Nuclear Physics* **72** (2013) 155.
- [77] F. Siegert, *Monte-Carlo Event Generation for the LHC*, doctoral thesis, Durham University, 2010.
- [78] J. J. Ethier, R. Gomez-Ambrosio, G. Magni and J. Rojo, *Smeft analysis of vector boson scattering and diboson data from the lhc run ii*, *The European Physical Journal C* **81** (2021) .
- [79] V. Barger, R. Phillips and D. Zeppenfeld, *Minijet veto: a tool for the heavy higgs search at the lhc*, *Physics Letters B* **346** (1995) 106–114.
- [80] D. Rainwater, R. Szalapski and D. Zeppenfeld, *Probing color-singlet exchange in $z + 2$ -jet events at the cern lhc*, *Physical Review D* **54** (1996) 6680–6689.
- [81] N. Kauer, T. Plehn, D. Rainwater and D. Zeppenfeld, *$H \rightarrow ww$ as the discovery mode for a light higgs boson*, *Physics Letters B* **503** (2001) 113–120.
- [82] T. Figy, V. Hankele and D. Zeppenfeld, *Dominant next-to-leading order QCD corrections to Higgs plus three jet production in vector-boson fusion*, *Journal of High Energy Physics* **2008** (2008) [0710.5621].

References

- [83] B. Jager, A. Karlberg and G. Zanderighi, *Electroweak $ZZjj$ production in the Standard Model and beyond in the POWHEG-BOX V2*, *Journal of High Energy Physics* **2014** (2014) [1312.3252].
- [84] B. Jager, F. Schissler and D. Zeppenfeld, *Parton-shower effects on higgs boson production via vector-boson fusion in association with three jets*, *Journal of High Energy Physics* **2014** (2014) 125 [1405.6950].
- [85] J. M. Cruz-Martinez, *Next-to-Next-to-Leading Order QCD Corrections to Higgs Boson Production in Association with two Jets in Vector Boson Fusion*, .
- [86] J. Cruz-Martinez, T. Gehrmann, E. W. N. Glover and A. Huss, *Second-order QCD effects in Higgs boson production through vector boson fusion*, *Physics Letters B* **781** (2018) 672 [1802.02445].
- [87] R. Cahn and S. Dawson, *Production of very massive Higgs bosons*, *Physics Letters B* **136** (1984) 196.
- [88] M. Ciccolini, A. Denner and S. Dittmaier, *Electroweak and QCD corrections to Higgs production via vector-boson fusion at the LHC*, *Physical Review D* **77** (2008) [0710.4749].
- [89] J. Lindfors, *Higgs boson production by W and Z collisions*, *Physics Letters B* **167** (1986) .
- [90] T. Han, G. Valencia and S. Willenbrock, *Structure Function Approach to Vector-Boson Scattering in pp Collisions*, *Physical Review Letters* **69** (1992) 3274 [hep-ph/9206246].
- [91] S. Alioli, P. Nason, C. Oleari and E. Re, *A general framework for implementing NLO calculations in shower Monte Carlo programs: the POWHEG BOX*, *JHEP* **06** (2010) 043 [1002.2581].
- [92] P. Nason, *The POWHEG BOX V2 framework*, .
- [93] E. Boos, M. Dobbs, W. Giele, I. Hinchliffe, J. Huston, V. Ilyin et al., *Generic User Process Interface for Event Generators*, Sept., 2001. 10.48550/arXiv.hep-ph/0109068.
- [94] J. Alwall et al., *A Standard format for Les Houches event files*, *Comput. Phys. Commun.* **176** (2007) 300 [hep-ph/0609017].
- [95] J. Alwall, R. Frederix, S. Frixione, V. Hirschi, F. Maltoni, O. Mattelaer et al., *The automated computation of tree-level and next-to-leading order differential cross sections, and their matching to parton shower simulations*, *JHEP* **07** (2014) 079 [1405.0301].
- [96] F. Maltoni and T. Stelzer, *MadEvent: Automatic event generation with MadGraph*, *JHEP* **02** (2003) 027 [hep-ph/0208156].
- [97] J. Alwall, P. Demin, S. de Visscher, R. Frederix, M. Herquet, F. Maltoni et al., *MadGraph/MadEvent v4: The New Web Generation*, *JHEP* **09** (2007) 028 [0706.2334].

- [98] H. Murayama, I. Watanabe and K. Hagiwara, *HELAS: HELicity amplitude subroutines for Feynman diagram evaluations*, .
- [99] F. Maltoni, K. Paul, T. Stelzer and S. Willenbrock, *Color Flow Decomposition of QCD Amplitudes*, *Phys. Rev. D* **67** (2003) 014026 [[hep-ph/0209271](#)].
- [100] W. Kilian, T. Ohl, J. Reuter and C. Speckner, *QCD in the Color-Flow Representation*, *JHEP* **10** (2012) 022 [[1206.3700](#)].
- [101] V. Hirschi, R. Frederix, S. Frixione, M. V. Garzelli, F. Maltoni and R. Pittau, *Automation of one-loop QCD corrections*, *JHEP* **05** (2011) 044 [[1103.0621](#)].
- [102] V. Hirschi, *New developments in MadLoop*, *PoS RADCOR2011* (2011) 018 [[1111.2708](#)].
- [103] A. Denner, S. Dittmaier and L. Hofer, *Collier: a fortran-based Complex One-Loop Library in Extended Regularizations*, *Comput. Phys. Commun.* **212** (2017) 220 [[1604.06792](#)].
- [104] G. Ossola, C. G. Papadopoulos and R. Pittau, *CutTools: A Program implementing the OPP reduction method to compute one-loop amplitudes*, *JHEP* **03** (2008) 042 [[0711.3596](#)].
- [105] A. Kardos, P. Nason and C. Oleari, *Three-jet production in POWHEG*, *JHEP* **04** (2014) 043 [[1402.4001](#)].
- [106] J. Taylor, *Ward identities and charge renormalization of the yang-mills field*, *Nuclear Physics B* **33** (1971) 436.
- [107] K. Arnold et al., *VBFNLO: A Parton level Monte Carlo for processes with electroweak bosons*, *Comput. Phys. Commun.* **180** (2009) 1661 [[0811.4559](#)].
- [108] J. Baglio et al., *VBFNLO: A Parton Level Monte Carlo for Processes with Electroweak Bosons – Manual for Version 2.7.0*, [1107.4038](#).
- [109] J. Baglio et al., *Release Note - VBFNLO 2.7.0*, [1404.3940](#).
- [110] S. Actis, A. Denner, L. Hofer, J.-N. Lang, A. Scharf and S. Uccirati, *RECOLA: REcursive Computation of One-Loop Amplitudes*, *Comput. Phys. Commun.* **214** (2017) 140 [[1605.01090](#)].
- [111] A. Denner, J.-N. Lang and S. Uccirati, *Recola2: a one-loop matrix-element generator for BSM theories and SM effective field theory*, *PoS RADCOR2017* (2017) 019 [[1712.04754](#)].
- [112] R. D. Ball, S. Carrazza, J. Cruz-Martinez, L. Del Debbio, S. Forte, T. Giani et al., *The Path to Proton Structure at One-Percent Accuracy*, *The European Physical Journal C* **82** (2022) 428 [[2109.02653](#)].
- [113] A. Buckley, J. Ferrando, S. Lloyd, K. Nordstrom, B. Page, M. Ruefenacht et al., *LHAPDF6: Parton density access in the LHC precision era*, *The European Physical Journal C* **75** (2015) 132 [[1412.7420](#)].
- [114] B. Jäger, A. Karlberg and S. Reinhardt, *QCD effects in electroweak $WZjj$ production at current and future hadron colliders*, [2403.12192](#).
- [115] M. Cacciari, G. P. Salam and G. Soyez, *FastJet user manual*, *The European Physical Journal C* **72** (2012) 1896 [[1111.6097](#)].

References

- [116] F. Campanario, M. Kerner, L. D. Ninh and D. Zeppenfeld, *Next-to-leading order QCD corrections to W^+W^+ and W^-W^- production in association with two jets*, *Phys. Rev. D* **89** (2014) 054009 [1311.6738].
- [117] B. Jager, A. Karlberg and J. Scheller, *Parton-shower effects in electroweak $WZjj$ production at the next-to-leading order of QCD*, *Eur. Phys. J. C* **79** (2019) 226 [1812.05118].
- [118] B. Cabouat and T. Sjöstrand, *Some dipole shower studies*, *The European Physical Journal C* **78** (2018) .
- [119] S. Höche, S. Mrenna, S. Payne, C. T. Preuss and P. Skands, *A Study of QCD Radiation in VBF Higgs Production with Vincia and Pythia*, *SciPost Phys.* **12** (2022) 010 [2106.10987].
- [120] B. Jäger, A. Karlberg, S. Plätzer, J. Scheller and M. Zaro, *Parton-shower effects in Higgs production via Vector-Boson Fusion*, *Eur. Phys. J. C* **80** (2020) 756 [2003.12435].
- [121] P. Nason and B. Webber, *Next-to-Leading-Order Event Generators*, *Ann. Rev. Nucl. Part. Sci.* **62** (2012) 187 [1202.1251].